

COMPONENTS' AND MATERIALS' PERFORMANCE FOR ADVANCED SOLAR SUPERCRITICAL CO2 POWERPLANTS

Wear and mechanical properties evaluation

Deliverable Number 4.2

WP4 Evaluation and modelling of metal/medium interaction

Date: 30 June 2025

Deliverable type: Report

Dissemination level: Public

Lead participant: CIEMAT





AUTHORS

Name	Organization
Marta Navas, Rebeca Hernandez, Elvira Oñorbe, Marta Serrano	CIEMAT
Florian Lebendig, Dmitry Naumenko	Forschungszentrum Jülich
Ceyhun Oskay, Christoph Grimme, Emma White	DECHEMA
Filip Radomir	CVR

DOCUMENT HISTORY

Version	Date	Change
01	07/05/2024	Initial version uploaded
02	30/06/2025	Revised version
		Erosion tests of novel materials (FZJ). Section 4.2.3
		Hot-long term abrasion tests (CVR). Section 4.3
		Small Punch tests for the novel materials (CIEMAT) Section 5.3.2
		Conclusions section 6

ABOUT THE PROJECT

COMPASsCO₂ is a 4-year HORIZON2020 project started on 1.11.2020. It is led by the German Aerospace Center (DLR), with eleven additional partners from seven European countries.

COMPASsCO₂ aims to integrate CSP particle systems into highly efficient s-CO₂ Brayton power cycles for electricity production. In COMPASsCO₂, the key component for such an integration, i.e. the particle/s-CO₂ heat exchanger, will be validated in a relevant environment. To reach this goal, the consortium will produce tailored particle and alloy combinations that meet the extreme operating conditions in terms of temperature, pressure, abrasion and hot oxidation/carburization of the heat exchanger tubes and the particles moving around/across them. The proposed innovative CSP s-CO₂ Brayton cycle plants will be flexible, highly efficient, economic and 100% carbon neutral large-scale electricity producers.

The research focus of COMPASsCO2 is on three main technological improvements: development of new particles, development of novel metal alloys and development of the heat exchanger section.

DISCLAIMER

This project has received funding from the European Union's Horizon 2020 Research and Innovation Action (RIA) under grant agreement No. **958418.**

The content of this publication reflects only the author's view and not necessary those of the European Commission. The Commission is not responsible for any use that may be made of the information this publication contains.

TABLE OF CONTENTS

Lis	t of	Figure	S	4
Lis	st of	Tables	S	8
Lis	st of	Abbre	viations	9
1	Ab	ostract		10
2	IN	TROD	UCTION	10
3	S	TRUC	TURAL MATERIALS and PARTICLES	11
4	W	EAR		12
	4.1	Wea	ar test at Ciemat	12
	4.	1.1	Experimental procedure	12
	4.	1.2	Test conditions	12
	4.	1.3	Results and discussion	13
	4.2	Wea	ar test at FZJ	21
	4.	2.1	Experimental procedure	21
	4.	2.2	Test conditions	22
	4.	2.3	Results and discussion.	23
	4.3	Hot	long term abrasion tets for CVR	34
	4.3	3.1	Experimental procedure	34
	4.3	3.2	Results and discussion	36
	4.4	Eva	luation of wear tests	49
5	M	ECHA	NICAL PROPERTIES	51
	5.1	Cre	ep properties at ciemat	51
	5.	1.1	Experimental procedure	51
	5.	1.2	Test conditions	52
	5.	1.3	Results and discussion.	54
,	5.2	Cre	ep properties at DFI	62
	5.	2.1	Experimental procedure	62
	5.	2.2	Test conditions	63
	5.	2.3	Results and discussion.	64
	5.3	Sma	all Punch Creep	66
	5.	3.1	Experimental procedure	66
	5.	3.2	Results	68
	5.	3.3	Discussion	74
	5.4	Eva	luation of creep properties	76
	5.4	4.1	Study of the effect of the environment: Air vs CO2	76

COMPASsCO2 - Components' and Materials' Performance for Advanced Solar Supercritical CO2 Power Plants

	5.4.2	Study of the effect of the specimen size	.77
	5.4.3	Use of the small specimen tests techniques: SSTT	.79
6	CONCL	USIONS	.81
7	FUTURI	E WORK	.82
8	REFERI	ENCES	.83

LIST OF FIGURES

Figure 1. Experimental system and specimens used in the erosion tests at Ciemat
Figure 2. Velocity profiles of particles for erosion test
Figure 3. Weight gain measurements obtained with different particles at 700°C and 5 mm/s velocity14
Figure 4. Weight gain measurements of uncoated and coated (R) materials obtained with
FerOx particles at 700°C and 5 mm/s velocity14
Figure 5. Weight gain measurements of uncoated and coated (R) materials obtained with
FerOx particles at 700°C and 20 mm/s14
Figure 6. Surface appearance of the different sides of P92 tested with B16/30 particles15
Figure 7. Surface appearance of the different faces of uncoated P92 tested with FerOx
particles16
Figure 8. Surface appearance of the different faces of coated P92 tested with FerOx particles
16
Figure 9. Surface appearance of the different faces of uncoated H282 tested with FerOx
particles17
Figure 10. Surface appearance of the different faces of coated H282 tested with FerOx
particles
Figure 11. Cross section of uncoated P92 tested with FerOx particles at 20mm/s during 1000h.
Figure 12. Cross section of coated P92 tested with FerOx particles at 20mm/s during 1000h.
Figure 13. SEM EDX analyses of uncoated P92 tested with FerOx particles at 20mm/s during 1000h19
Figure 14. SEM EDX analyses of uncoated P92 tested with FerOx particles at 20mm/s during
1000h19
Figure 15. Cross section of uncoated H282 tested with FerOx particles at 20mm/s during
1000h20 Figure 16. Cross section of coated H282 tested with FerOx particles at 20mm/s during 1000h.
20
Figure 17. SEM EDX analyses of uncoated H282 tested with FerOx particles at 20mm/s during
1000h20
Figure 18. SEM EDX analyses of uncoated H282 tested with FerOx particles at 20mm/s during
1000h21
Figure 19. Schematic setup of the testing facility at Forschungszentrum Jülich (on the left),
sample aperture (in the center), and a side view showing the sample holder immersed in the
granulate bed22
Figure 20. Effective erosion mass change data at 900°C for Alloy 617, Haynes 282, INCONEL
740, and Sanicro 25 tested with SGB granulates (BL 30/50, BL 16/30, SB 30/50, IP 30/50, and
FerOx 16/30) at a particle flow rate of 5 mm s ⁻¹ 24
Figure 21. Selected backscattered electron images of cross-sectioned materials after
oxidation-erosion testing for 250 hours in air at 900 °C. The images correspond to the weight
change data in Figure 2025
Figure 22. Backscattered electron images of a cross-sectioned sample of Sanicro 25 after
undergoing oxidation-erosion testing for 250 hours in air at a temperature of 900°C using
BL16/30 and SB 30/50. These close-up images correspond to those shown in Figure 2026

Figure 23. Topographical backscattered electron images of candidate materials after oxidation
erosion testing for 250 hours in air at 900 °C. Black coloration of the sample surface implies
deposition of the bauxite-based granulate material27
Figure 24. Effective erosion after 1000 h at 900 °C in air, using SB 30/50 (Gen 3) granulate
with a flow rate of 5 mm s ⁻¹ 28
Figure 25. Backscattered electron images of cross-sectioned materials after cyclic oxidation
and oxidation-erosion testing for 1000 hours in air at 900 °C. The images correspond to the
weight change data in Figure 2428
Figure 26. Topographical backscattered electron images of candidate materials after cyclic
oxidation and oxidation-erosion testing for 250 hours in air at 700 °C. Black coloration within
·
the sample matrix implies granulate deposition of the bauxite-based material SB 30/5029
Figure 27. Comparison of selected granulates before (as-received) and after erosion-oxidation
testing with particle flow rates of either 5 mm s ⁻¹ or 20 mm s ⁻¹
Figure 28 Sanicro 25 after erosion testing at 700°C for 250 h in a bed of FerOx16/30 particles
with relative particle flow rate of 20 mm/s under ambient air3
Figure 29: SEM/BSE-image (a) and corresponding elemental EDX-maps (b-f) of Sanicro 29
ground to 80 grit finish after erosion testing at 700°C for 250 h in a bed of FerOx16/30 particles
with relative particle flow rate of 20 mm/s under ambient air3
Figure 30: Specimens of studied state of the art alloys after testing: (a-d) Preoxidised at 900°C
for 72 h with subsequent erosion testing at 900°C for 250 h in FerOx 16/30 granulate at relative
particle speed of 20 mm/s; (e-h) Specimens after oxidation at 900°C for 250 h in lab air32
Figure 31. Mass change data measured during erosion testing at 600°C in SB30/50 granulate
at 5 mm/s particle relative velocity of Cr-based alloys produced at UoB in comparison to Alloy
617
Figure 32. SEM cross-sections after erosion testing at 600°C in SB30/50 granulate at 5 mm/sec
particle relative velocity of Cr-based alloys produced at UoB a), c), d) in comparison to Alloy
617 (b)
Figure 33. Mass change data measured during erosion testing at 900°C in Ferox 16/30
granulate at 5 mm/sec particle relative velocity of alloys with CrSi-coatings (by Dechema) in
comparison to uncoated Alloy 617
Figure 34. SEM cross-sections after erosion testing at 900°C in Ferox 16/30 granulate at \$
mm/sec particle relative velocity of CrSi-coated alloys (b,c) in comparison to uncoated Alloy
617 (a)
Figure 35. SEM cross-section of CrSi-coated Sanicro 25 after erosion testing at 900°C in Feros
16/30 granulate at 5 mm/sec particle showing coating interdiffusion behaviour: a) BSE-image
b,c) EDX-maps for Si and Cr respectively34
Figure 36: PID - Particle loop - hot long term test configuration35
Figure 37: Test section with the tested material samples39
Figure 38: Three specific regions for analysis36
Figure 39: Top section. a) Inconel 740 with compact oxide layer. b) Sanicro 25 with non
compact oxide layer (spallation)36
Figure 40: Side section. a) Inconel 617 with groove-like features. b) Inconel 740 sample with
Cr-Si coating exhibited surface pits in which fractured oxide fragments and erosive particles
had accumulated3
Figure 41: Bottom section. a) An intact coating layer TiAlSiN on Haynes 282. b) Cross-section
SEM image of intact coating layer TiAlSiN on Haynes 282
Figure 42: Cr-Fe-Al-Ni alloy with non-compact protective oxide layer with visible cracking and
progressing internal oxidation along grain boundaries
PLANTON IN THE LINE AND

Figure 43: Haynes 282 with Cr-Si coating. Spallation of the oxide layer was observed, a	along
with internal oxidation beneath the applied coating	39
Figure 44. CIEMAT creep lab	
Figure 45. M8 specimen to perform creep tests at CIEMAT	51
Figure 46. New M5 specimen for CIEMAT creep tests	
Figure 47. M8 vs. M5 specimen. M5 specimen machined from M8 specimen	52
Figure 48. Tensile curves obtained for each SOTA material	53
Figure 49. Creep curves of (a) Sanicro 25, (b) IN-617B, (c) IN-740 and (d) Haynes-282	in air
at 700°C. Please note the varying x- and y-axes in the respective diagrams	56
Figure 50. (a) Minimum creep rate of the investigated alloys as a function of applied stress	s, (b)
Larson-Miller plot of the investigated alloys. Tests performed in air at 700 °C	57
Figure 51. Creep curves obtained for P92 at 700°C and different loads: 150, 100, 80	and
70MPa	57
Figure 52: SEM images and EDS maps of P92 tested at 700 °C/70MPa	58
Figure 53: SEM images and EDS maps of Haynes 282 tested at 700 °C/400MPa	59
Figure 54: SEM images and EDS maps of Sanicro 25 tested at 700 °C/230MPa	60
Figure 55: SEM images and EDS maps of Inconel 740 tested at 700 °C/400MPa	
Figure 56: SEM images and EDS maps of Inconel 617 tested at 700 °C/250MPa	
Figure 57. (a) Test rig constructed by DFI for creep testing in flowing CO ₂ , (b) dimensio	
creep test samples tested at DFI.	
Figure 58. Creep curves of (a) Sanicro 25, (b) IN-617B, (c) IN-740 and (d) Haynes-28	
flowing IG-CO ₂ at 700°C. Please note the varying x- and y-axes in the respective diagr	ams.
Figure 50. (a) Minimum group rate of the investigated allows as a function of applied stress	
Figure 59. (a) Minimum creep rate of the investigated alloys as a function of applied stress	
Larson-Miller plot of the investigated alloys.	
Figure 60. Cross sectional LOM images of the investigated alloys after creep tests. Places for each alloy, the images on the left hand side belong to green test complete who	
note for each alloy, the images on the left-hand side belong to creep test samples, whe	
the images on the right-hand side belong to the samples without external load. The depl	
zones are indicated by an arrow in the respective images.	
Figure 61. Schematic diagram of small punch creep system.	
Figure 62. CIEMAT small punch creep machine.	
Figure 63. Orientation of SP specimens. SP/SPC specimen.	
Figure 64. Finished procedure to obtain discs for SPC tests	
Figure 65. Small punch curves for SOTA materials at room temperature (RT)	
Figure 66. Small punch curves for SOTA materials at 300 °C.	
Figure 67. Small punch curves for SOTA materials at 500 °C	
Figure 68. Microstructural study and fractography of the samples before and after testing	•
the Cr5Ni5Al 10Fe by UoB.	
Figure 69. Small punch curves obtained for UoB materials	
Figure 70. Small punch curves: SOTA and novel alloys.	
Figure 71. Deflection vs. Time curves obtained for Cr. Test conditions: 700°C and 40kg.	
Figure 72. Small punch creep curves obtained at 700°C and 60 kg for IN740, IN617	
Sanicro25.	
Figure 73. Small punch creep curves obtained at 700°C and 50 kg for IN740, IN617	
Sanicro25.	
Figure 74. Small punch creep curves obtained at 700°C and 40 kg for IN740 and IN617.	
Figure 75. Comparison of the creep data in air and in CO2. Values obtained in air teste	•
CIEMAT are indicated as hollow symbols. Please note the two different geometries fo	r the

Sanicro 25 samples tested in air by CIEMAT. The hollow symbols in this case belong to M5 (miniature samples), whereas the semi-filled triangles denote the M8 samples. The borderline criterion, indicating the highest acceptable creep rate at 10⁻⁶s⁻¹, is illustrated by the dashed red Figure 76. Larson-Miller plot of the investigated alloys in both test atmospheres. Please note that Sanicro 25 creep tests in air were conducted with two different sample geometries, namely M5 (miniature) and M8 (standard).77 Figure 77. Stress (MPa) vs.Time (h) at 700 °C for P92 in air at 700 °C77 Figure 78. T91 steel tested on creep conditions (550°C, 225MPa) at CIEMAT......78 Figure 79. Stress (MPa) vs. Time (h) curve at 700°C for reference H282 alloys (Ref. Plate: Solution Annealed + Age Hardened 282® Plate and Ref. Sheet: Solution Annealed + Age Hardened 282® Sheet) and H282 studied in air and H282 studied in CO₂79 Figure 80. Load (kg) vs. creep time (h) for IN740 and IN617 alloys......79 Figure 81. Deflection rate (mm/h) vs. load (N)80 Figure 82. Fracture surface of conventional creep specimens for IN617 and IN740 alloys. ..80 Figure 83.Bottom fracture of SPC rupture specimens for IN617 and IN740 alloys......80

LIST OF TABLES

Table 1. Chemical composition of SOTA materials tested	11
Table 2: Experimental matrix of erosion tests at Ciemat	13
Table 3: Weight gain measurements at different times	13
Table 4. Phase composition of studied granulates (Rietveld refinement)	26
Table 5: Evaluation of the tested abrasion material samples	39
Table 6: Overview of the SEM results for selected materials	40
Table 7. Initial creep test matrix	53
Table 8. Tensile properties	53
Table 9. Applied stresses for the creep tests in air at CIEMAT	54
Table 10. Creep results obtained for H282 at 700 °C	54
Table 11. Creep results obtained for IN740 at 700 °C	55
Table 12. Creep results obtained for IN617 at 700 °C	55
Table 13. Creep results obtained for Sanicro25 at 700 °C	55
Table 14. Creep properties obtained for P92 alloy	57
Table 15: Thickness of oxide scales for P92 under different test conditions	58
Table 16: Thickness of oxide scales for Sanicro25 two different test conditions	59
Table 17: Thickness of oxide scales for Sanicro25 under different test conditions	60
Table 18: Thickness of oxide scales for Inconel 740 under different test conditions	61
Table 19. Applied stresses for the creep tests in CO ₂ at DFI.	63
Table 20. SP results obtained for IN740 alloy.	70
Table 21. SP results obtained for Sanicro25 steel.	70
Table 22. SP results obtained for IN617 alloy.	71
Table 23. Applied loads for the small punch creep tests in air and at 700°C at CIEMAT	71

LIST OF ABBREVIATIONS

COMPASsCO2	Components' and Materials' Performance for Advanced Solar Supercritical CO2 Power Plants								
CIEMAT	Centro de Investigaciones Energéticas Medioambientales y Tecnológicas (Spain)								
DECHEMA	DECHEMA-Forschungsinstitut (Germany)								
FZJ	Forschungszentrum Jülich (Germany)								
CSP	Concentrated Solar Power (Plants)								
EC	European Commission								
EU	European Union								
H282	Haynes 282								
IN740	INCONEL 740								
IN617	INCONEL 617 (Alloy 617)								
ОМ	Optical Microscopy								
P92	Ferritic steel grade P92								
SEM/EDS	Scanning Electron Microscope/ Energy Dispersive X ray Spectrocopy								
SOTA	Sate Of The Art (Materials)								
SP	Small Punch								
SPC	Small Punch Creep								

1 ABSTRACT

Work Package 4 of the H2020 COMPASsCO2 project is focussed on the evaluation and modelling of the metal/medium interaction and the assessment of candidate materials for particle/s-CO2 heat exchangers. As the primary usage of these materials is in the heat exchanger of the innovative CSP-supercritical CO₂ power plants, separate investigations for each of the two atmospheres of the heat exchanger (ambient air and CO₂) were conducted.

This report includes the experimental work and results obtained in the Task 4.1 regarding to the external wall investigation of the structural material and its interaction with the particles. The laboratory investigations, wear and creep tests and aim to understand the degradation mechanisms of these materials, in order to assess their performance. The main degradation expected is related to oxidation and corrosion protection, mechanical properties and wear. These properties have been studied with the State Of The Art (SOTA) materials and particles, used as reference, and the new particles developed in WP2 and the new bulk materials and coating developed in WP3. The laboratory tests are carried out under conditions simulating actual plant conditions. The degradation mechanisms of the materials are analysed in order to predict the lifetimes of the materials (heat carrier particles and heat exchanger components).

The deliverable D 4.2 provides a comprehensive overview of the wear and mechanical properties testing results.

2 INTRODUCTION

Work Package 4 of the H2020 COMPASsCO2 project is focussed on the evaluation and modelling of metal/medium interactions and the assessment of candidate materials for particle/s-CO₂ heat exchangers. As the primary usage of these materials is in the heat exchanger of the innovative CSP-supercritical CO₂ power plants, separate investigations for each of the two atmospheres of the heat exchanger (ambient air and CO₂) were conducted.

The laboratory tests are carried out under conditions that simulate actual plant conditions. The degradation mechanisms of the materials are analysed and funnelled into a model to predict operating lifetimes of the materials (heat carrier particles and heat exchanger components). Service lifetime estimation models of the interactions between particles degradation, alloys erosion and corrosion are being developed. The objectives are:

- To investigate the **oxidation**, **corrosion** and **wear** behaviour of the candidate materials
- To understand the degradation mechanisms
- To characterise the candidate materials and to assess their performance

Task 4.1 focused on investigating the material degradation on the outer side of the heat exchanger tubes. The main degradation expected is related to oxidation and corrosion protection, mechanical properties and wear. These properties have been studied with the State Of The Art (SOTA) materials and particles, used as reference, and the new particles developed in WP2 and the new bulk materials and coating developed in WP3.

This report includes the experimental work and results obtained in the Task 4.1 regarding to the external wall investigation of the structural material and its interaction with the particles. The same materials and particles were used in the following different tests performed by the different laboratories. Wear tests have been performed at Ciemat and FZJ laboratories with different experimental conditions. Mechanical properties have been studied by creep tests at Ciemat and Dechema facilities, and by small punch creep tests at Ciemat.

3 STRUCTURAL MATERIALS AND PARTICLES

The same structural materials and particles were used in the wear and mechanical tests and they were distributed among the different laboratories. Table 1 shows the chemical composition of State Of The Art (SOTA) or commercial materials tested.

Matariala		Chemical composition Wt.%													
Materials	Fe	Ni	Со	Cr	Al	Mn	Si	Nb	Ti	Мо	W	Cu	С	Other	
Ferritic	P92	Bal.	0.2	1.5	11.4		0.17	0.44			0.27	1.5		0.11	0.22 V
Austenite	Sanicro 25	42.6	25.4	1.5	22.3	0.03	0.5	0.2	0.5			3.4	3		0.2 N
	617B	1.2	54.6	11.9	22.3	1	0.04	0.05		0.4	8.2				0.05 B
Ni-base	282	0.2	57.1	10.6	19.6	1.6	0.02	0.04		2.2	8.6				
	740	0.1	49.7	20.6	24.5	1.4	0.3	0.2	1.5	1.4					

Table 1. Chemical composition of SOTA materials tested.

Novel coatings were developed by Dechema (WP3) as Cr-Si diffusion coatings on Fe- or Nibased state of the art materials, P92 and Hayness 282. These coatings were tested in the wear/erosion tests performed at Ciemat with new particles.

Particles have also been developed by project partner (Saint-Gobain Research Provence) in WP2 of this project to be used as direct heat transfer and storage media. Two different particle types have been tested, state of the art proppants based on bauxite composition, and the newly developed FerOx particles (or Granulated GEN4, see [1]), with different size:

- BL 16/30 ("bauxite light")
- BL 30/50 ("bauxite light")
- SB 16/30 ("sintered bauxite")
- IP 30/50 ("inter-proppant")
- FerOx 16/30 ("containing iron oxide"),

where the particle size of 16/30 corresponds to 590 / 1190 μ m, and 30/50 to 297 / 590 μ m respectively.

4 WEAR

4.1 WEAR TEST AT CIEMAT

4.1.1 Experimental procedure

Erosion tests at Ciemat laboratories have been performed based on the movement/rotation of specimens immersed in the particles using autoclaves equipped with a rotating multisampling holder, at 700°C. Figure 1 shows the experimental device, including the autoclave with the motor stirring, specimen holder and cylindrical specimens used for erosion tests.

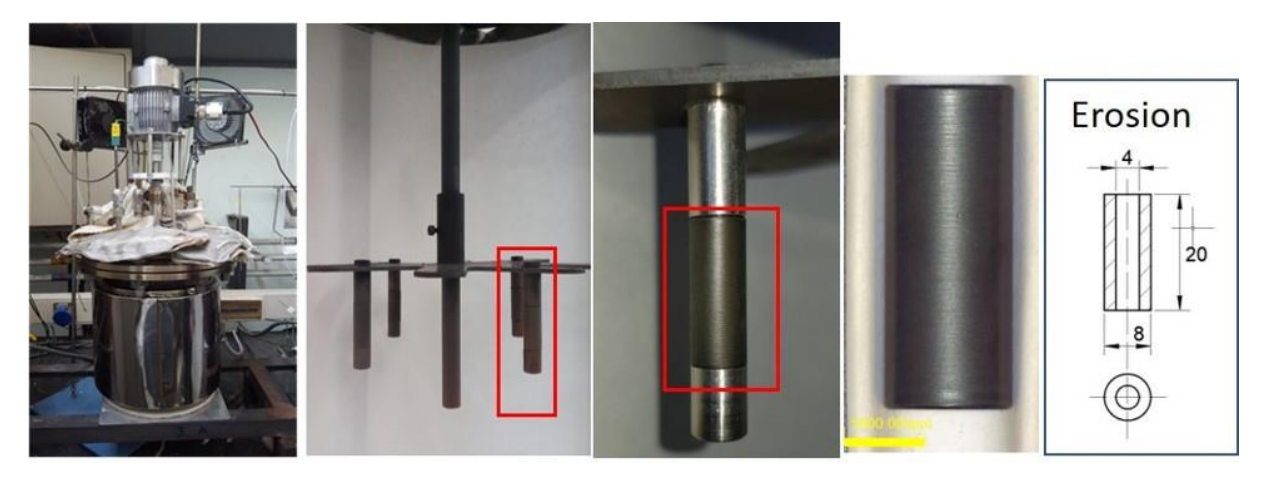


Figure 1. Experimental system and specimens used in the erosion tests at Ciemat.

The geometry of the specimens was chosen in order to simulate the effect of particles erosion, taking into account the tube geometry in the heat exchanger, and to study the possible differences along the external diameter of specimen with four position: front (particles impact head-on), back side or two lateral sides. This final geometry was selected based on the velocity profiles simulated for the different erosion specimen's types and positions (Figure 2).

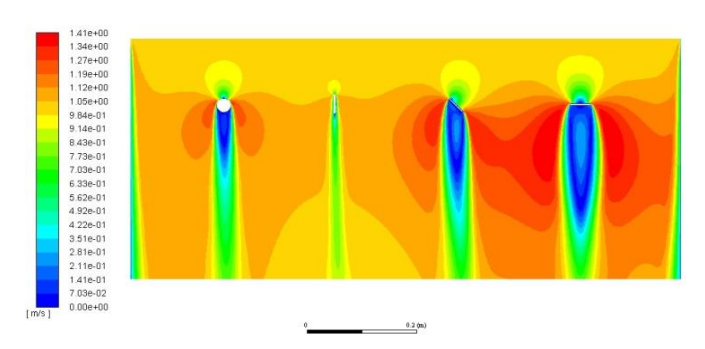


Figure 2. Velocity profiles of particles for erosion test

4.1.2 Test conditions

The objective of the erosion tests at Ciemat is to determine the erosion properties of the new particles (Saint-Gobain) and new coatings for metals (Dechema) developed in the other WP of the project (WP2 and WP3 respectively). The experimental matrix of the erosion tests performed at Ciemat are shown in Table 2. As a reference, one experiment was performed with bauxite B16/30 particles, to compare with the new FerOx particles with the same size (590 / 1190 μ m). The coatings were tested simultaneously on specimens of P92 and Haynes 282,

to study the effect of the coating on metals with FerOx particles. Tests were carried out in air at 700 °C up to 1000 hours with two different rotating speeds corresponding to 5mm/s and 20mm/s lineal velocities.

Test Speed Time **Particle Materials** 700°C (mm/s)(h) 250 P92 Bauxite 5 1 (Reference) 16/30 H282 1000 P92, H282 2 250 Coating on P92, H282 5 P92, H282 3 1000 FerOx Coating on P92 / H282 16/30 P92, H282 4 250

20

Coating on P92 / H282

Coating on P92 / H282

P92, H282

Table 2: Experimental matrix of erosion tests at Ciemat

4.1.3 Results and discussion

5

Erosion test results include the weight measurements and the detailed optical and SEM examination of the entire surface of the specimens, before and after the tests in both cases.

1000

Results of the weight measurements have demonstrated a weight gain in all of the materials tested (Table 3) that increased with the testing time and the velocity of the particles. The weight gain indicated that oxide formation and/or particles deposition have been obtained.

Weight gain (mg/cm²) Time **Materials** B16/30 **FerOx** (h) 5 mm/s 5mm/s 20 mm/s 0.48 250 0.26 0.61 P92 1.02 1.02 1000 1.04 250 1.64 0.72 P92 coated 1000 3.96 3.51 250 0.22 0.40 1.17 H282 1000 0.97 0.96 1.98 0.22 250 0.38 H282 coated 1000 0.29 0.72

Table 3: Weight gain measurements at different times

Figure 3 shows the weight gain results of the two SOTA materials (P92 and Haynes 282) with the two particles (Bauxite and FerOx with the same size 16/30) tested at 700°C and 5 mm/s. Similar results are obtained after 1000 hours testing with the different SOTA materials and particles. Results with new coatings and particles are shown in Figure 4 and Figure 5 with a clear increase in the weight gains in the case of the P92 coated (R) but a low increase in the Haynes 282 coated (R) compared with uncoated one.

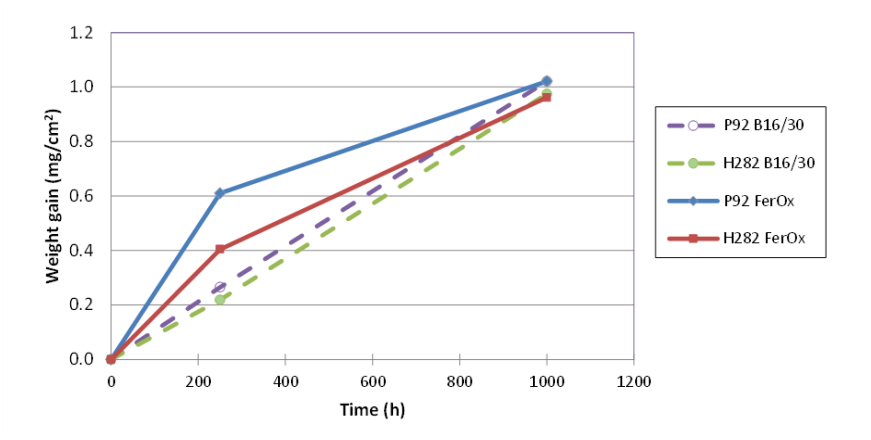


Figure 3. Weight gain measurements obtained with different particles at 700°C and 5 mm/s velocity

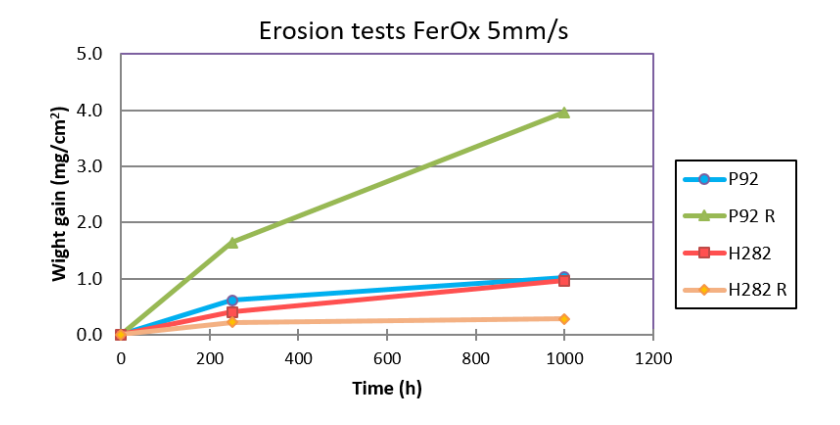


Figure 4. Weight gain measurements of uncoated and coated (R) materials obtained with FerOx particles at 700°C and 5 mm/s velocity

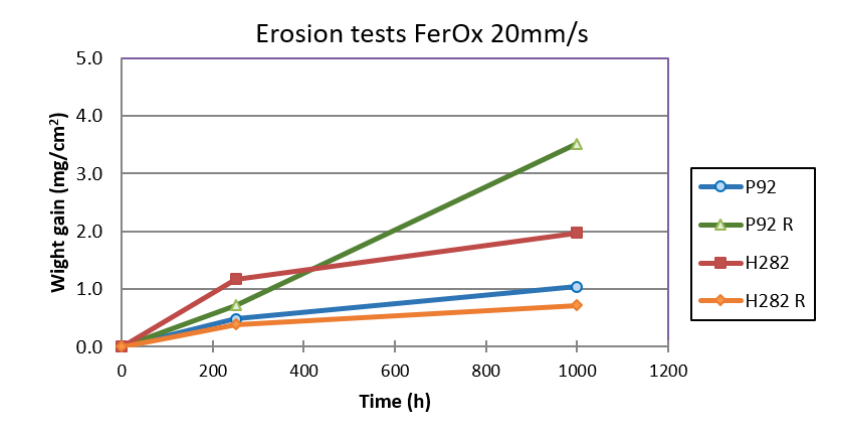


Figure 5. Weight gain measurements of uncoated and coated (R) materials obtained with FerOx particles at 700°C and 20 mm/s

The obtained gain values could be due to the oxidation of the material and/or the deposition of the particles over specimen surface. The deposition of the particles has been observed in the results of Optical and Scanning microscopies shown below. Metallographic examination and SEM/EDX analyses were carried out in the cross section of the specimens.

Figure 6 shows the OM images obtained in the middle length of the specimen surface at the four different sides: front (particles impact head-on), backside or two sides of P92 and Haynes 282. A higher number of circumferential lines is observed on the front faces at longer times. Taking into account the iron content in the alloys, further oxidation should be expected in the case of P92 than in H282. However, the similar behaviour obtained, both in the images and in the gain measurements, seems to indicate that the effect of particle deposition has more influence on the weight gain than oxidation.

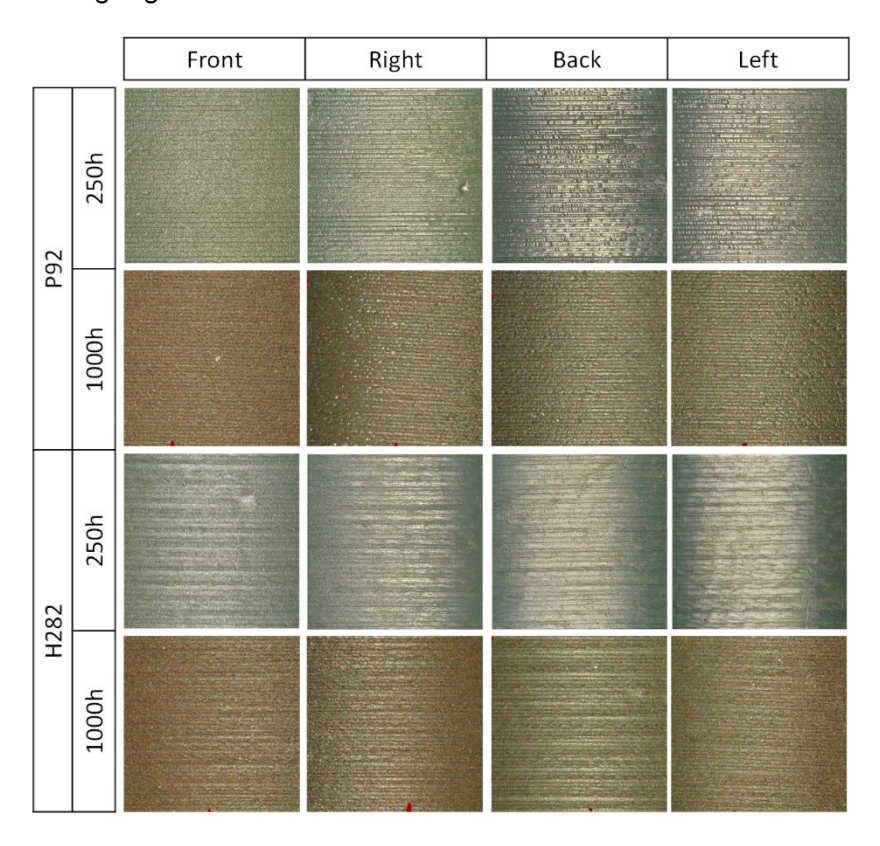


Figure 6. Surface appearance of the different sides of P92 tested with B16/30 particles.

Appearance of specimen surfaces are shown for P92 in Figure 7 and for P92 coated in Figure 8 tested with FerOx particles at two velocities and two testing duration. FerOx particles are deposited or embedded, resulting in the red colour of the circumferential lines on front face, while big deposits have grown on the less exposed faces, especially in the backside at higher times and velocity. In the case of the coated specimens (Figure 8), particles deposition shown to be uniform on the different faces but it is not possible to distinguish from the coatings with this technique. In addition, the coatings have demonstrated a good behaviour with only one small detached zone in all the specimen surfaces.

Figure 9 shows the surface appearances of uncoated Haynes 282 with similar circumferential red lines. FerOx particles are deposited or embedded in small machining marks and produced the red colour on front face. Besides these mechanical lines are still visible on the back faces without FerOx deposition. No detached zones were observed in the coated H282 specimens although the particles deposition seems to change the specimen appearance (Figure 10).

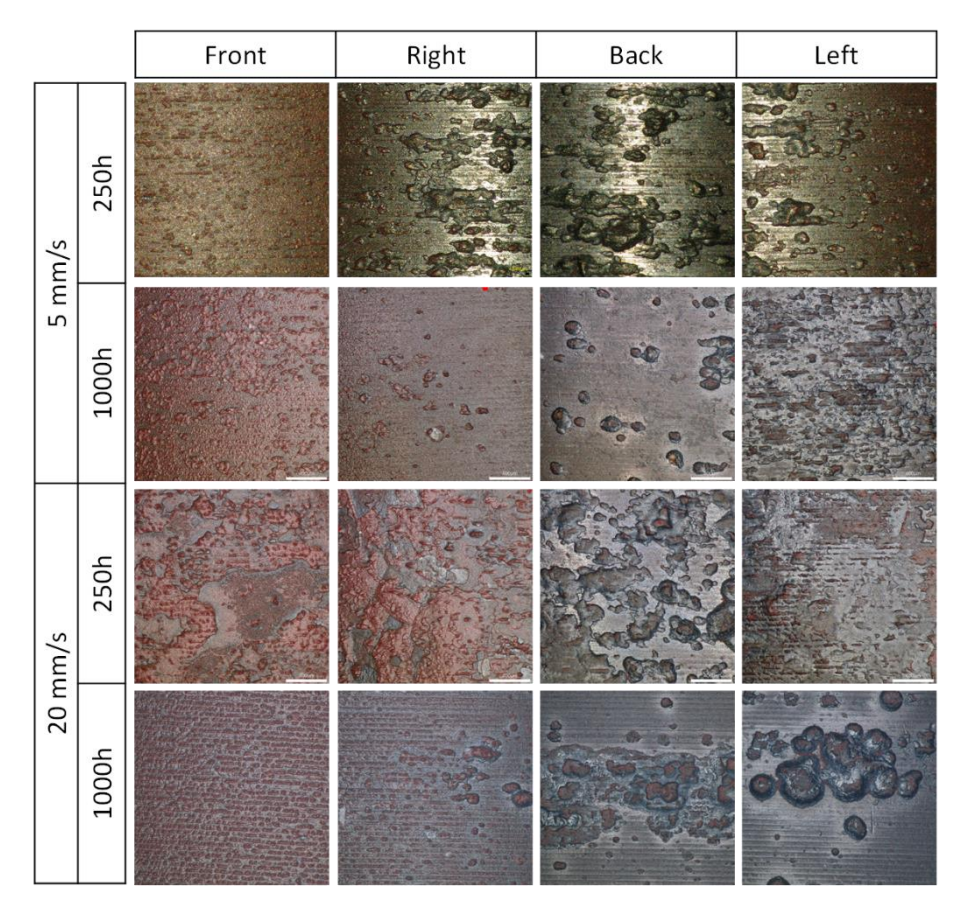


Figure 7. Surface appearance of the different faces of uncoated P92 tested with FerOx particles.

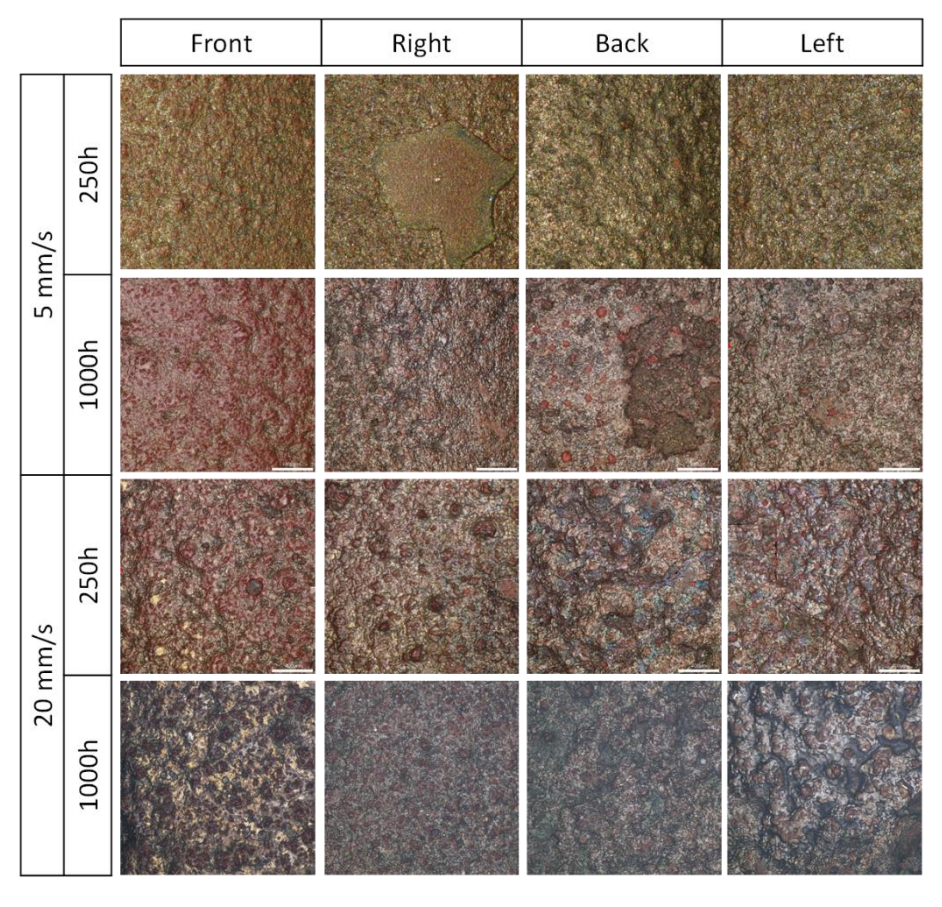


Figure 8. Surface appearance of the different faces of coated P92 tested with FerOx particles

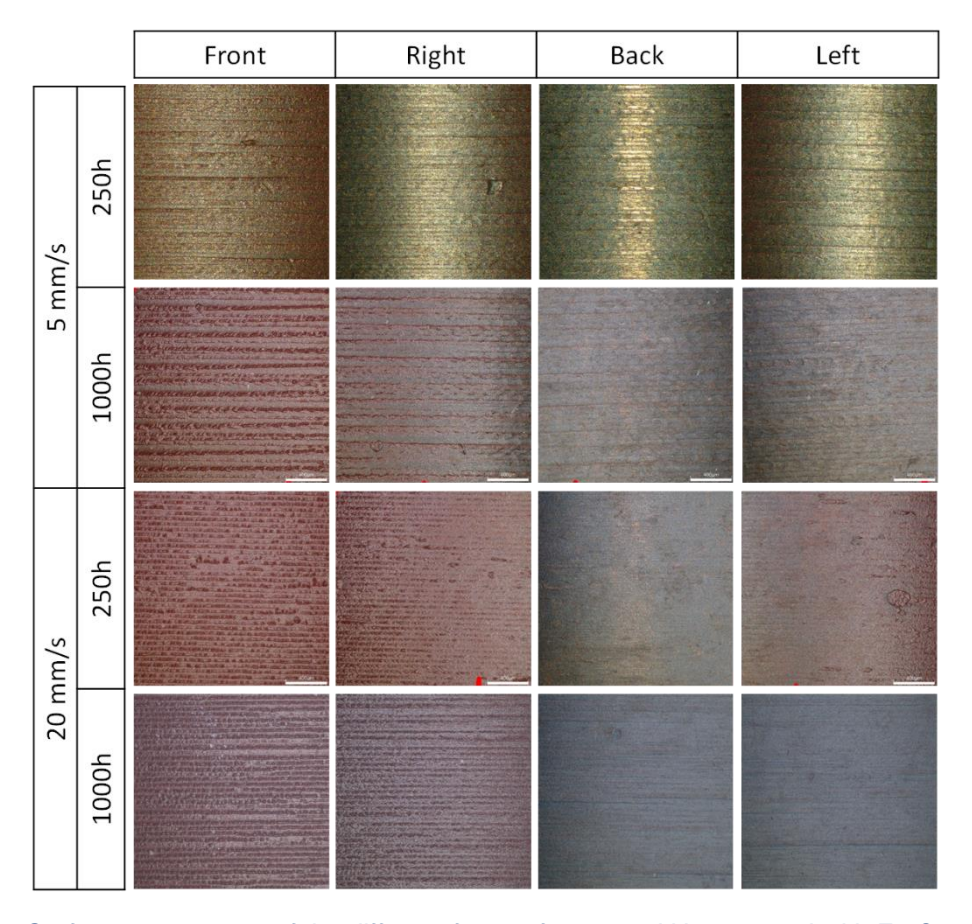


Figure 9. Surface appearance of the different faces of uncoated H282 tested with FerOx particles.

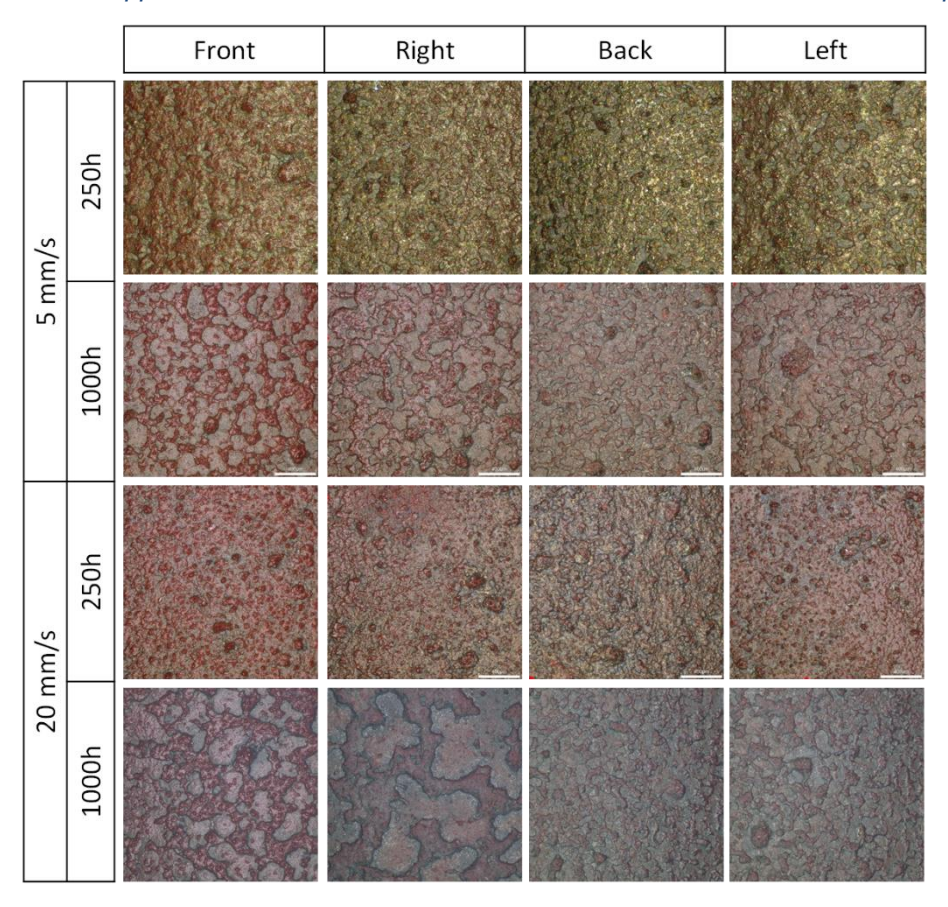


Figure 10. Surface appearance of the different faces of coated H282 tested with FerOx particles.

The extent of deposition is mainly influenced by particle velocity and testing time but also on the chemical composition of the alloy as it was observed in the SEM/EDX metallographic examination of all tested specimens. The cross-section, at the mid-section of the specimens, was studied to determine any erosion defect, the oxide formation and/or the deposition of FerOx particles. The highest depositions were obtained in the specimens tested at 700°C and 20mm/s velocity during 1000h. Figure 11 shows that uncoated P92 deposits have big and continuous growth on the front and right faces while only isolated big grains, with poor adherence, are observed on the other faces. The shape of the continuous deposits on more exposed faces demonstrates the particles impacting with the waveform typical morphology of wear/erosion degradation, which has not been observed in the free surfaces (backside) excluding the material removal in these zones.

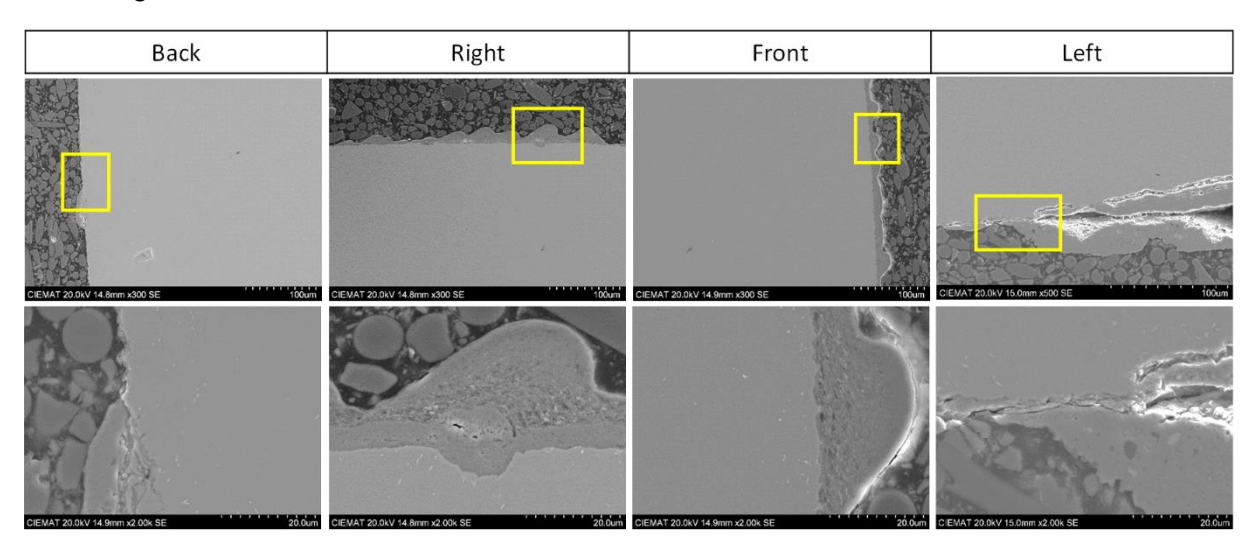


Figure 11. Cross section of uncoated P92 tested with FerOx particles at 20mm/s during 1000h.

Coated specimens of P92 (Figure 12) presented a very small FerOx deposition in the upper part of the coatings. Although the coatings are still over the entire surface, at few points of the front face are small holes that have not been filled with the deposits. The particle deposits are smaller which indicates a better performance with the coating, although as they are distributed all over surface, the final effect may not be beneficial according to the higher gain obtained under all conditions.

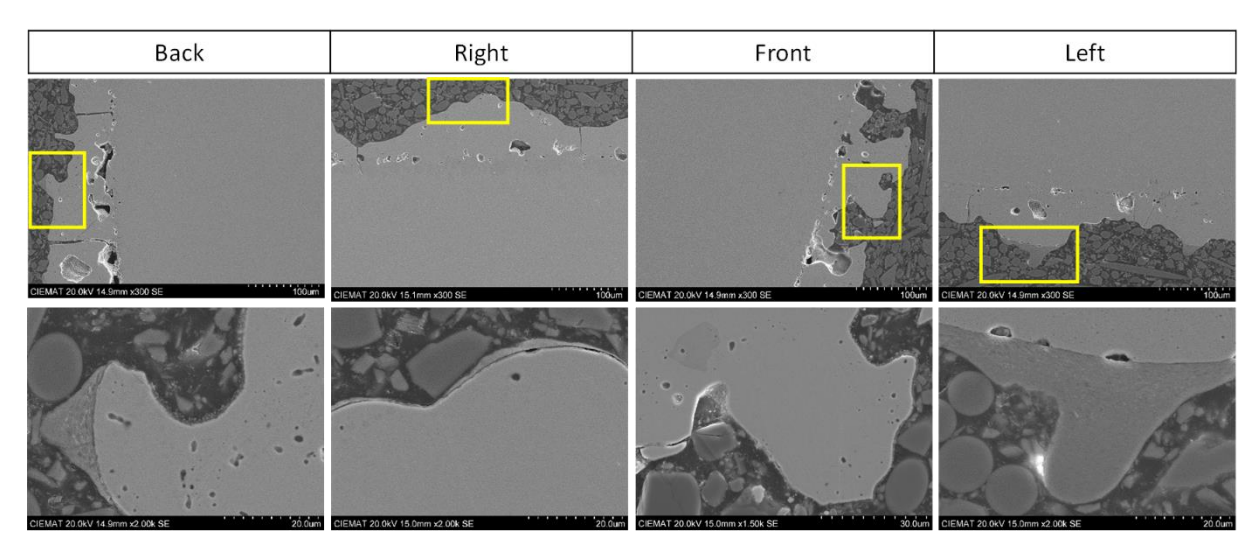


Figure 12. Cross section of coated P92 tested with FerOx particles at 20mm/s during 1000h.

Figure 13 and Figure 14 include SEM/EDX analyses of the uncoated and coated P92 tested at maximum time and velocity with FerOx particles. External layer corresponds to the particle deposits formed with his own elements of iron, oxygen, zirconium, silicon and aluminium. Under this deposit, in some zones of the uncoated P92 is possible to determine an oxide layer composed mainly by iron and chromium, the chemical elements of the alloy. In the case of the coated P92, the chemical elements of the coatings (chromium, silicon and nickel) demonstrated their presence over the entire surface and there are only small and isolated deposits of particles with the same composition than FerOx particles.

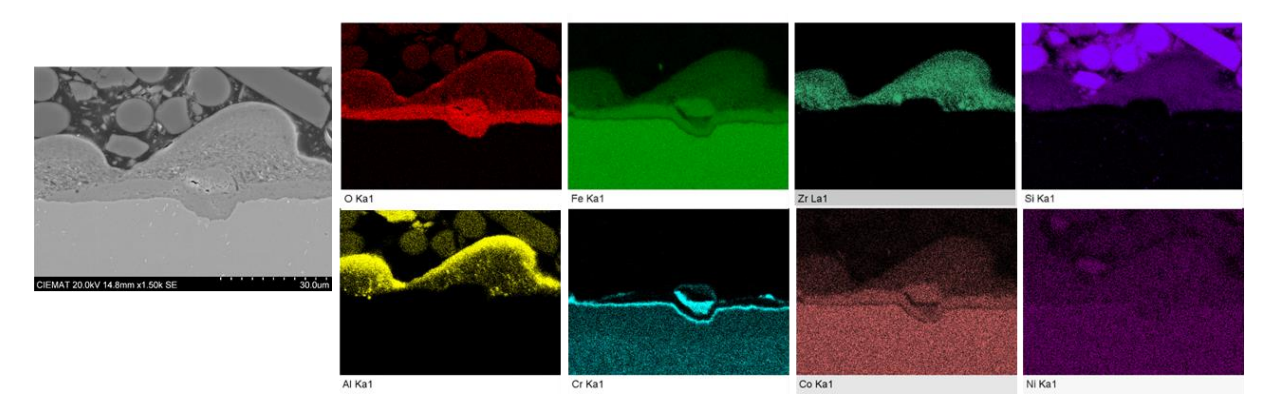


Figure 13. SEM EDX analyses of uncoated P92 tested with FerOx particles at 20mm/s during 1000h.

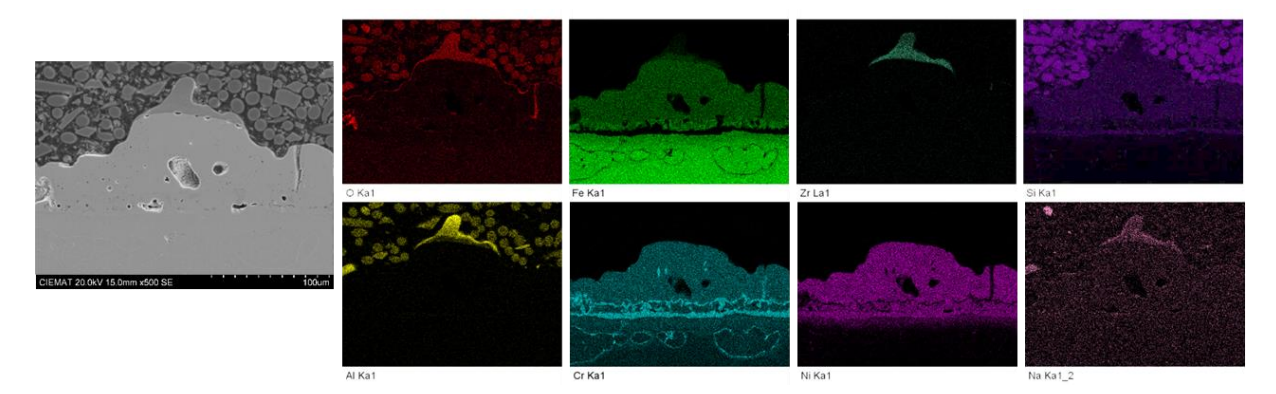


Figure 14. SEM EDX analyses of uncoated P92 tested with FerOx particles at 20mm/s during 1000h.

Figure 15 and Figure 16 show the images of the different faces of uncoated and coated H282 cross-sectioned specimens tested with FerOx particles at 700°C and 20 mm/s during 1000h. The highest deposition was obtained in the more exposed faces, front and right, and also the waveforms demonstrates the impact of new particles over the deposits producing the typical morphology of wear/erosion degradation, which has not been observed in the free surfaces (backside), excluding the material removal in these zones.

Figure 17 and Figure 18 include the SEM/EDX analyses of the uncoated and coated Haynes 282 tested at maximum time and velocity with FerOx particles. The external layer has the same composition than in P92, which correspond to the particle deposits (O, Fe, Si, Zr and Al). No oxide formation was observed on uncoated H282 although very small penetrations without oxide were detected with very low extent compare to CO₂ oxidation. In that case, the particle deposition seems to have a protective effect on the material avoiding the oxide formation. In the case of the coated H282, the coatings were observed under the deposits without any signal of degradation.

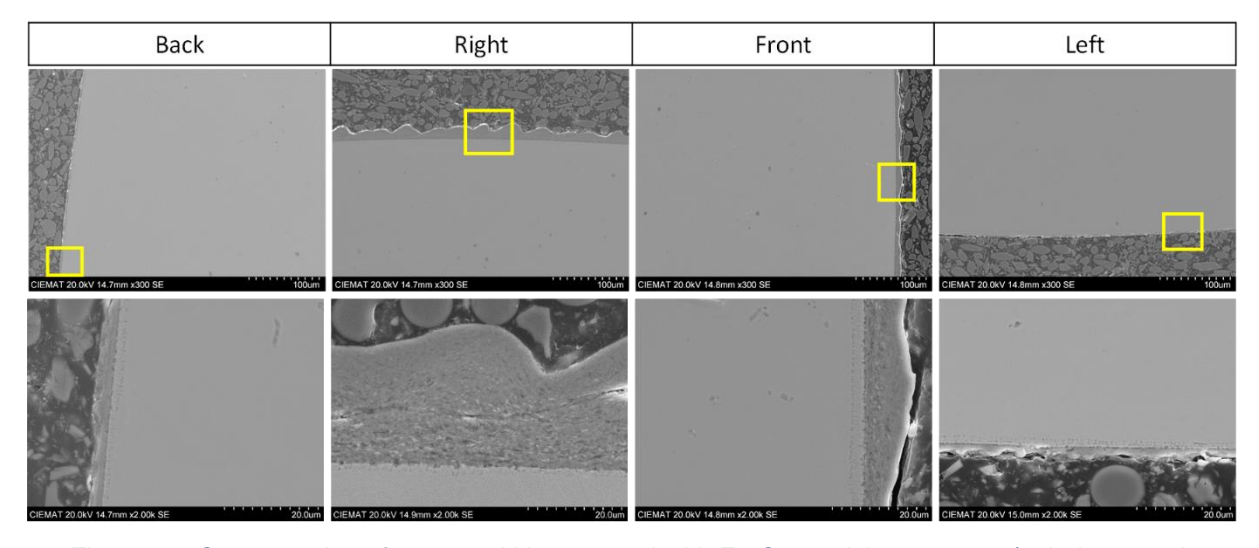


Figure 15. Cross section of uncoated H282 tested with FerOx particles at 20mm/s during 1000h.

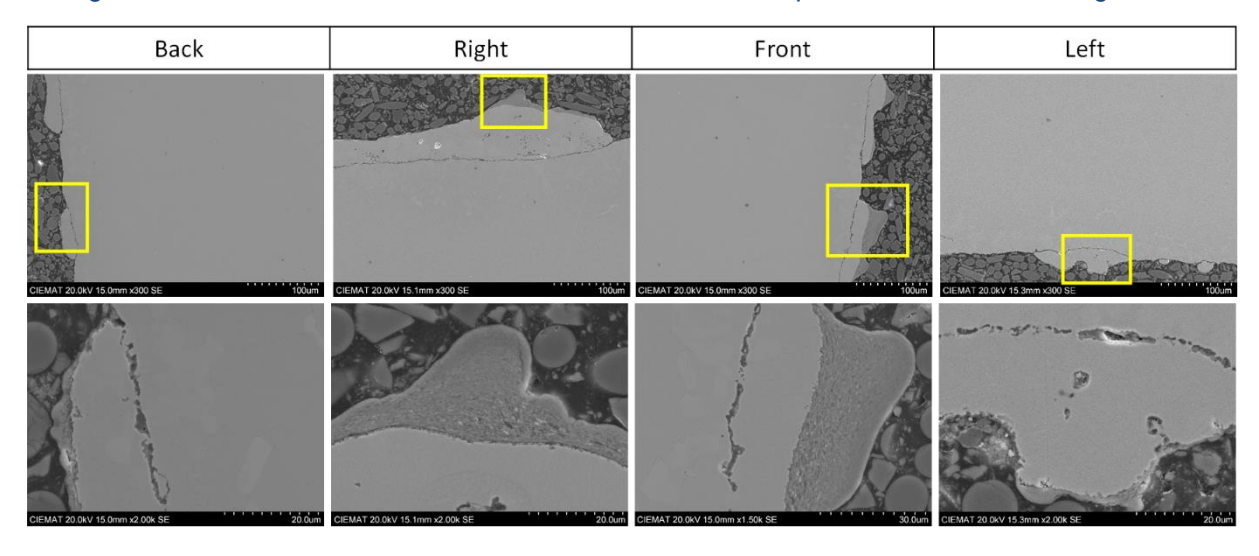


Figure 16. Cross section of coated H282 tested with FerOx particles at 20mm/s during 1000h.

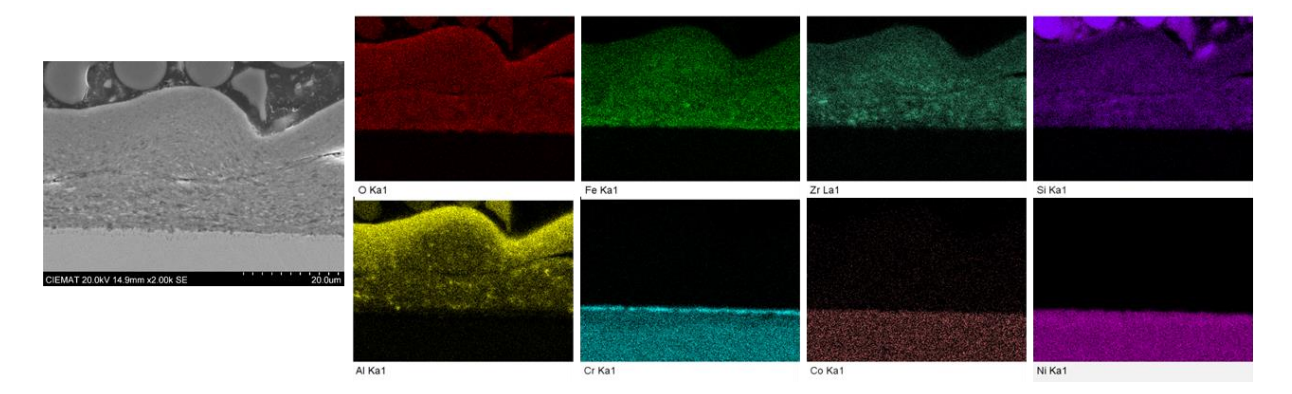


Figure 17. SEM EDX analyses of uncoated H282 tested with FerOx particles at 20mm/s during 1000h

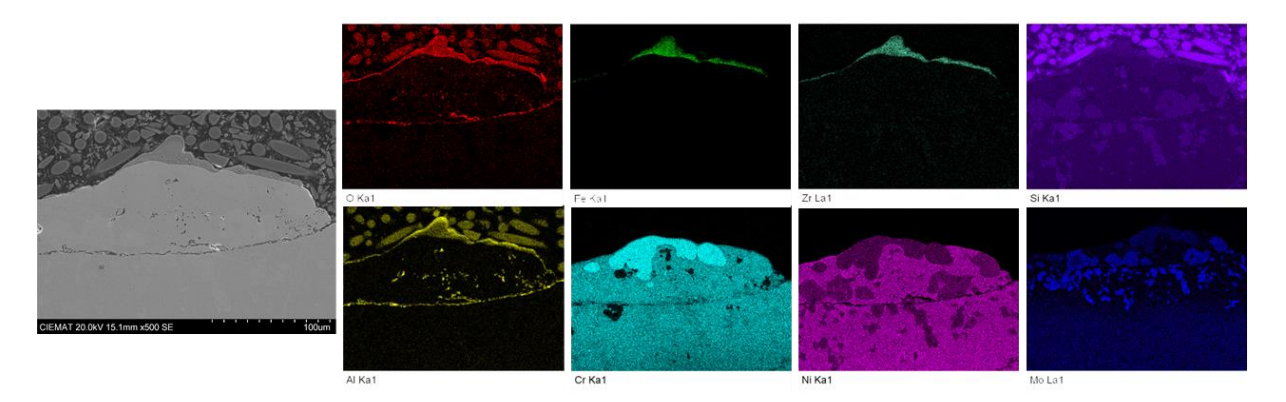


Figure 18. SEM EDX analyses of uncoated H282 tested with FerOx particles at 20mm/s during 1000h

Regarding to the coating deposited over the metallic surfaces, a good resistance to erosion degradation has been demonstrated with only an isolated detached zone in the case of P92 with the lower time and particle velocity so it could be due to a non-detected previous defect. In addition, the particle deposits on the coatings are smaller and isolated, indicating better performance with the coating. The beneficial effect of the coating on Haynes 282 was demonstrated by the lowest weight gain, which is consistent with the lower particle deposition and no oxide formation observed in the specimen examination under all conditions.

4.2 WEAR TEST AT FZJ

4.2.1 Experimental procedure

Erosion-oxidation exposures were carried out at FZJ using various granulates, provided by project partners form Saint-Gobain Research Provence, as direct heat transfer and storage media:

- BL 16/30 ("bauxite light")
- BL 30/50 ("bauxite light")
- SB 16/30 ("sintered bauxite")
- IP 30/50 ("inter-proppant")
- FerOx 16/30 ("containing iron oxide"),

where the particle size of 16/30 corresponds to 590 / 1190 $\mu m,$ and 30/50 to 297 / 590 μm respectively.

Three testing facilities were set-up for erosion-oxidation testing at temperatures of 600, 700, and 900 °C in air. The erosion testing was performed in a vertical furnace filled with particles and the specimen holder was rotated at a predefined constant speed. To simulate normal operating conditions for the particle heat exchanger, the particle velocity was set at 5 mm s⁻¹. Additionally, erosion-oxidation testing are being initiated with a higher particle velocity of 20 mm s⁻¹ corresponding to maximum possible velocity during plant operation. A schematic setup of the testing facility and the sample aperture is shown in Figure 19.

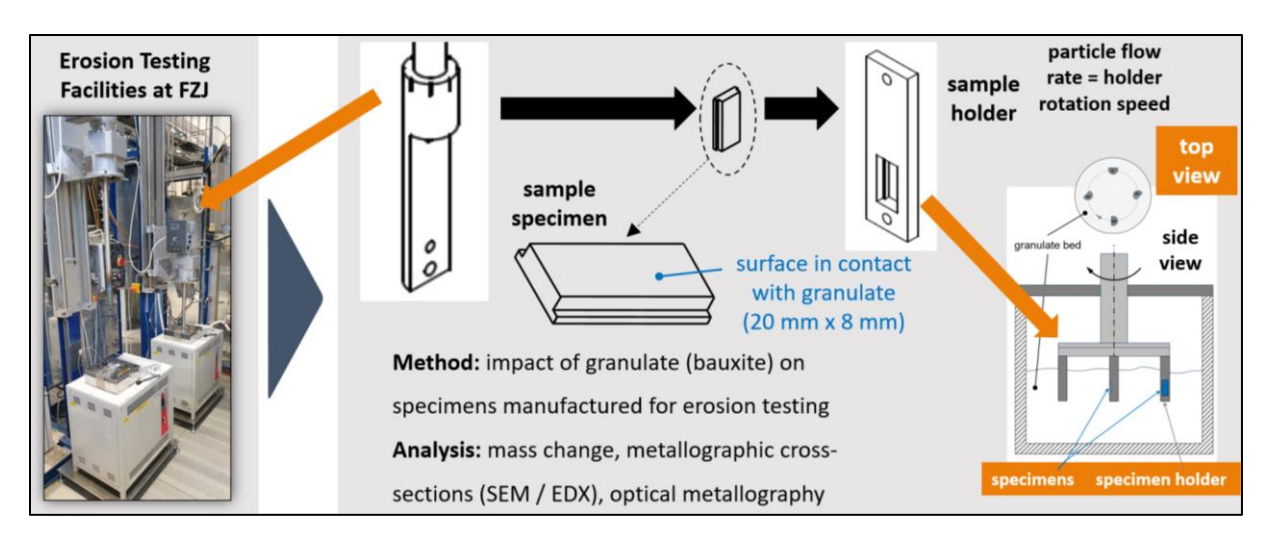


Figure 19. Schematic setup of the testing facility at Forschungszentrum Jülich (on the left), sample aperture (in the center), and a side view showing the sample holder immersed in the granulate bed.

The effective erosion was determined based on data obtained from cyclic oxidation (see Deliverable 4.1) and oxidation-erosion testing. Furthermore, data points were extracted from isothermal thermogravimetric analysis (refer to Deliverable 4.1) to obtain more accurate weight changes during the initial 50 hours of measurements.

Equation 1 presents the methodology for determining the effective erosion mass changes associated with the front surface area of the specimen in contact with granulate as shown in Figure 20.

$$\Delta m_{erosion}^{eff.} = \frac{(A_{erosion}^{whole} \cdot \Delta m_{erosion}) - (A_{cycl.\ oxidation}^{whole} \cdot \Delta m_{cycl.\ oxidation})}{A_{erosion}^{exposed}}$$
 Eq1

The variable **A** in Equation 1 represents the surface area of the specimen in cm², which refers to the entire surface of the erosion specimen $(A_{erosion}^{whole})$, the complete surface of the specimen used for cyclic oxidation testing $(A_{cycl.\ oxidation}^{whole})$, or the frontal surface of the erosion specimen $(A_{erosion}^{exposed})$ which is the surface in contact with the granulate (see Figure 19). The mass changes measured during cyclic oxidation or oxidation-erosion testing are denoted as $\Delta \mathbf{m}$ (given in mg cm⁻²).

4.2.2 Test conditions

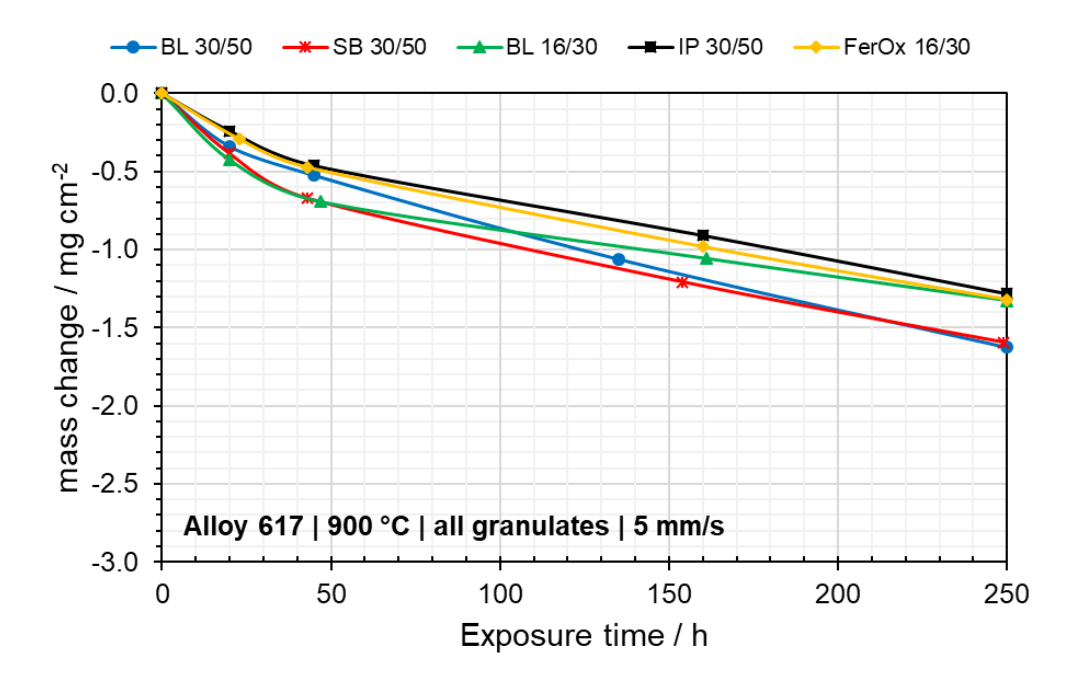
The four commercial alloys Sanicro 25, Alloy 617b (IN617), INCONEL 740 (IN740), and Haynes 282 were selected for the investigations, which represent excellent high temperature properties, designed for reheater and superheater tubes in thermal power plants (see Deliverable 4.1). IN617, IN740, and Haynes 282 are Ni-based alloys, whereas Sanicro 25 is an austenitic alloy. The analyzed chemical composition of these materials can be seen in Table 1. Specimens were cut from the as-received materials, ground to 1200 grit surface finish and cleaned with a solvent prior to further investigations. Erosion-oxidation exposures were carried out at temperatures varying from 600 to 900 °C for a maximum duration of 1000 hours, with

the standard duration being 250 hours, as this short-term testing period was found to be sufficient to observe effects. Most of the tests were performed with relative particle velocity of 5 mm s⁻¹; one test was also performed at 20 mm s⁻¹.

An in-depth characterization of the cross-sectioned alloys after erosion testing was performed by scanning electron microscopy (SEM) and energy dispersive x-ray spectroscopy (EDX). The results were compared to the data obtained from high-temperature air oxidation exposures of the studied alloys without influence of erosion.

4.2.3 Results and discussion

Mass changes were recorded during oxidation-erosion testing, and corresponding backscattered electron images of the specimen surfaces as well as cross-sectioned samples were taken. Commercial state-of-the-art materials Alloy 617, Haynes 282, INCONEL 740, and Sanicro 25 (see performance in oxidizing and carburizing atmospheres, Deliverable 4.1) were examined using bauxite-based granulates provided by Saint Gobain. For the erosion tests presented here, also the newly developed particles FerOx 16/30 were selected, as this granulate represents the latest generation (Gen 4) exhibiting enhanced mechanical properties compared to the other particles (Gen 3). The mass change data are presented for all alloys in the following (Figure 20).



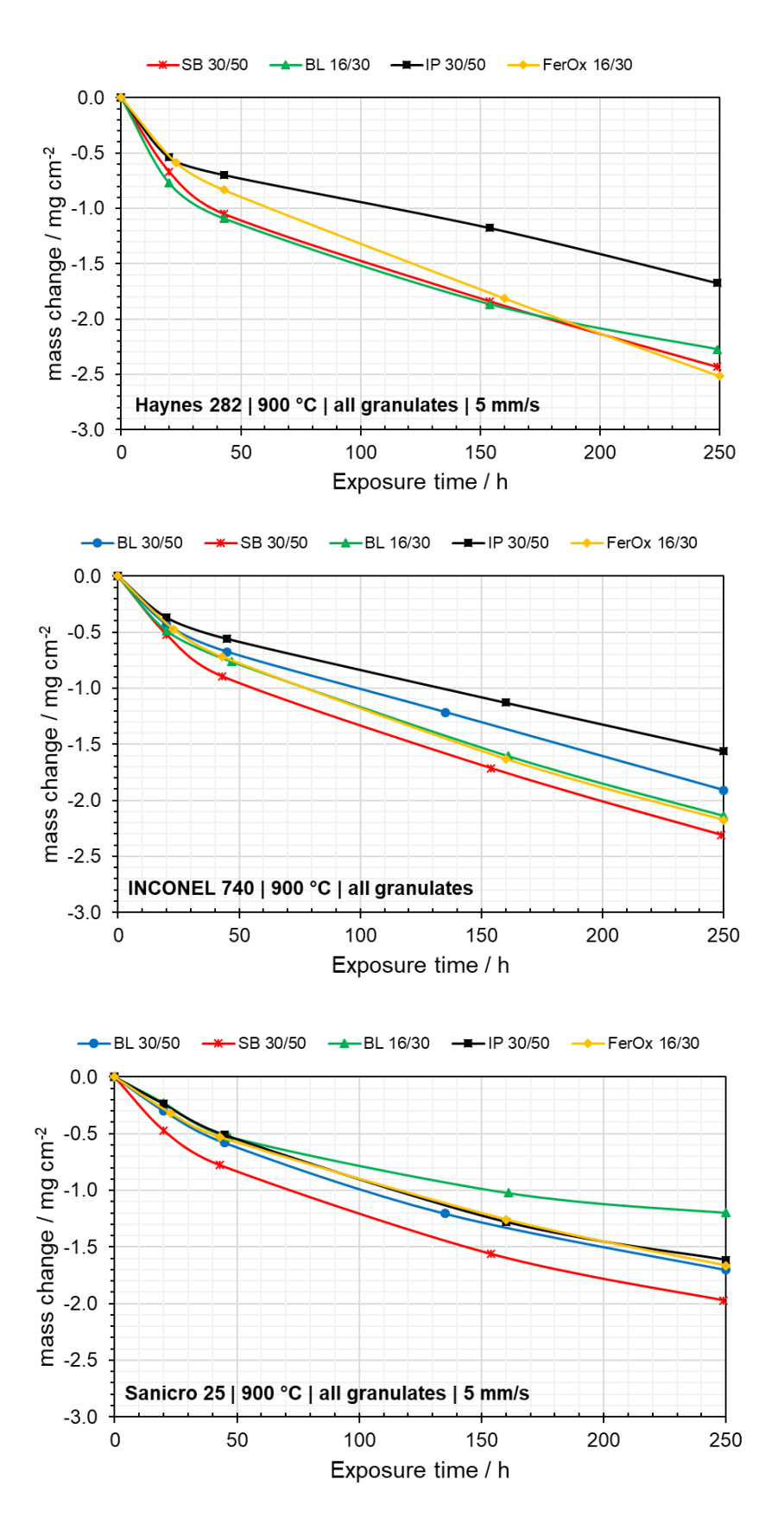


Figure 20. Effective erosion mass change data at 900°C for Alloy 617, Haynes 282, INCONEL 740, and Sanicro 25 tested with SGB granulates (BL 30/50, BL 16/30, SB 30/50, IP 30/50, and FerOx 16/30) at a particle flow rate of 5 mm s⁻¹.

Backscattered electron images of cross-sectioned alloys corresponding to the weight change data shown in Figure 20 are depicted in Figure 21. SEM images were provided for alloys that exhibited the highest and lowest weight changes after oxidation-erosion testing, based on the type of granulate used. The first cross-section demonstrates the specimen with the least mass loss, while the second cross-section depicts the greatest mass loss. It can be seen that the erosion occurs within the oxide scales in all studied cases.

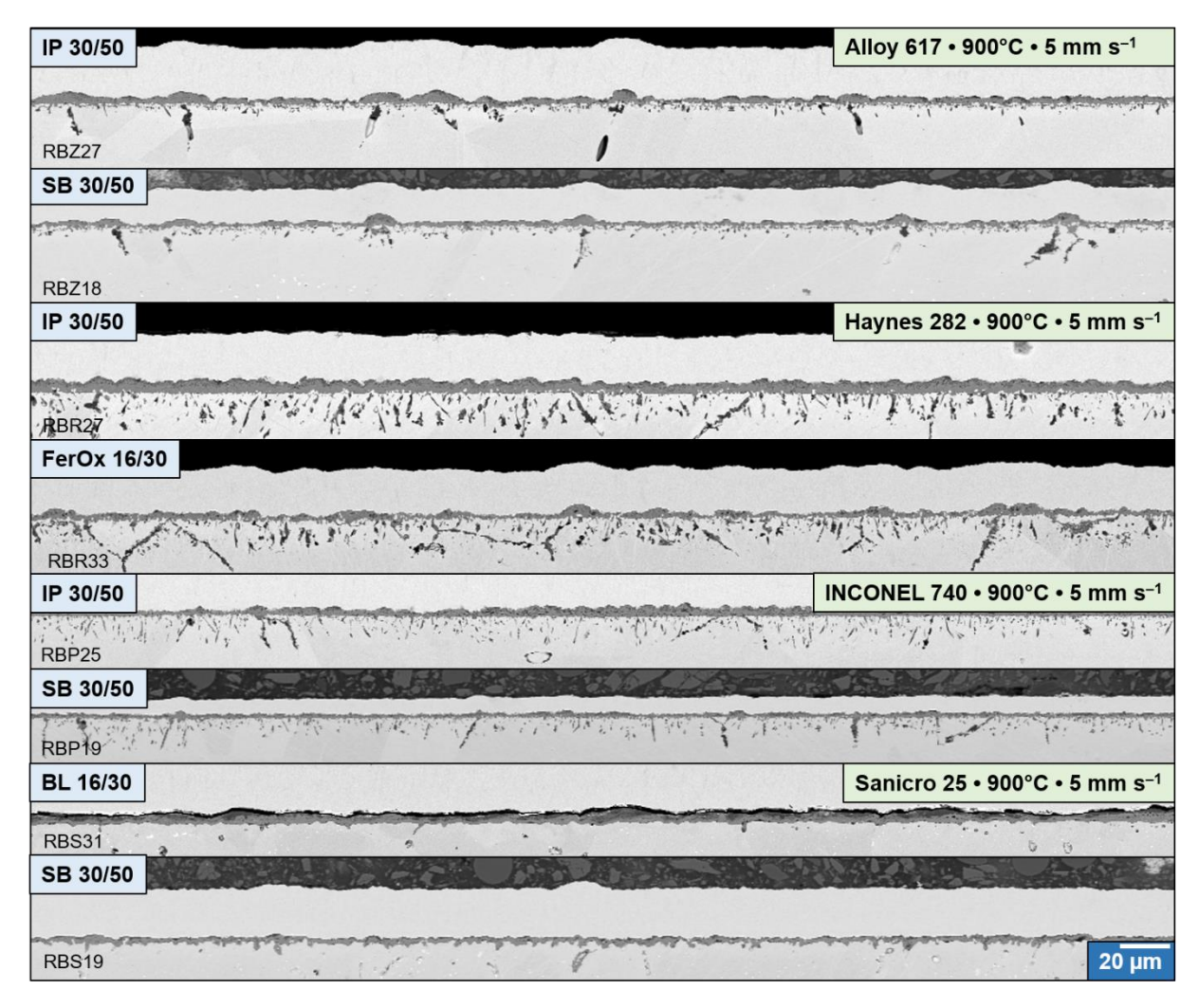


Figure 21. Selected backscattered electron images of cross-sectioned materials after oxidationerosion testing for 250 hours in air at 900 °C. The images correspond to the weight change data in Figure 20.

Sanicro 25 exhibited distinct granulate material deposition on the surface when erosion tests were conducted using BL 16/30, which was particularly evident in this scenario (compare close-up view in Figure 22).

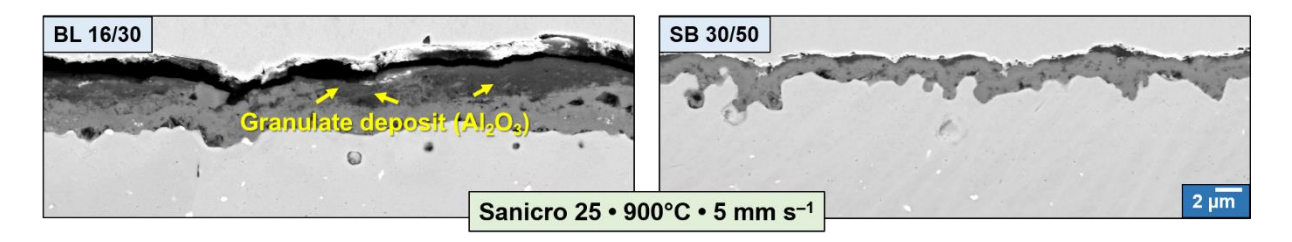


Figure 22. Backscattered electron images of a cross-sectioned sample of Sanicro 25 after undergoing oxidation-erosion testing for 250 hours in air at a temperature of 900°C using BL16/30 and SB 30/50.

These close-up images correspond to those shown in Figure 20.

A phase analysis of the ceramic constituents in the granulate indicated that the corundum content in BL 16/30 is considerably greater compared to BL 35/50.

The oxidation-erosion testing shows that for majority of the alloys the least mass loss occurred when using IP 30/50, while the highest mass loss occurred with SB 30/50. An exception was noted with Sanicro 25, where SB 30/50 displayed the highest mass loss, but the least mass loss when using BL 16/30.

In an attempt to correlate the measured erosion rates of the studied alloys with the granulate properties, the phase compositions of the granulates were identified using XRD. Table 4 presents the phases detected through XRD Rietveld analysis, alongside with the Mohs hardness values for each phase taken from literature (2, 3, 4 and 5).

Granulate	Corundum	Mullite	Hematite	m-Zirconia	Quartz	Other (mainly ilmenite)
FerOx 16/30	34		32	29	1.1	3.5
IP 30/50	83	11				6
SB 30/50	89	4				7
BL 30/50	59	30	2		0.1	9
BL 16/30	82	9	0.8			8
Mohs scale	9	6.5	5.5	8.25	9	≈ 5.5

Table 4. Phase composition of studied granulates (Rietveld refinement).

Average hardness was calculated for each granulate based on the respective room-temperature hardness values (as per the Mohs scale) of each mineralogical crystal phase whereas the presence of amorphous phases was neglected as a first approximation:

- FerOx 16/30 ≈ **7.5**
- IP 30/50 ≈ **8.5**
- SB 30/50 ≈ **8.7**
- BL 30/50 ≈ **7.9**
- BL 16/30 ≈ **8.4**

The highest estimated hardness values of the SB30/50 granulate correlate well with the highest measured mass losses of the studied materials. However, the estimated hardness values for IP30/50, SB30/50 and BL16/30 are not very much different. Moreover, the erosion rates of

Alloy 617, IN740 and Haynes 282 are lower when tested with IP30/50 granulate compared to SB30/50 in spite of similar estimated room temperature hardness. Therefore, other factors might play a role in determining the erosion rates.

Both BL 30/50 and BL 16/30 should be viewed as the same granulate, differing only in particle sizes. However, the Rietveld analysis "uncovered" notable differences in the corundum and mullite contents. This finding indicates that BL 16/30 likely possesses a lower hardness in comparison to BL 30/50.

Topographical backscattered SEM images of all samples post oxidation-erosion testing are displayed in Figure 23. The presence of black discoloration on the sample surface indicates granulate deposition (corundum). Hematite deposition from FerOx and Cr₂O₃ can be challenging to differentiate due to their similar average atomic weights (compare all alloys after oxidation-erosion testing with FerOx 16/30). Zirconia was also detected on the surface, attributed to the m-ZrO₂ rich phase in FerOx 16/30.

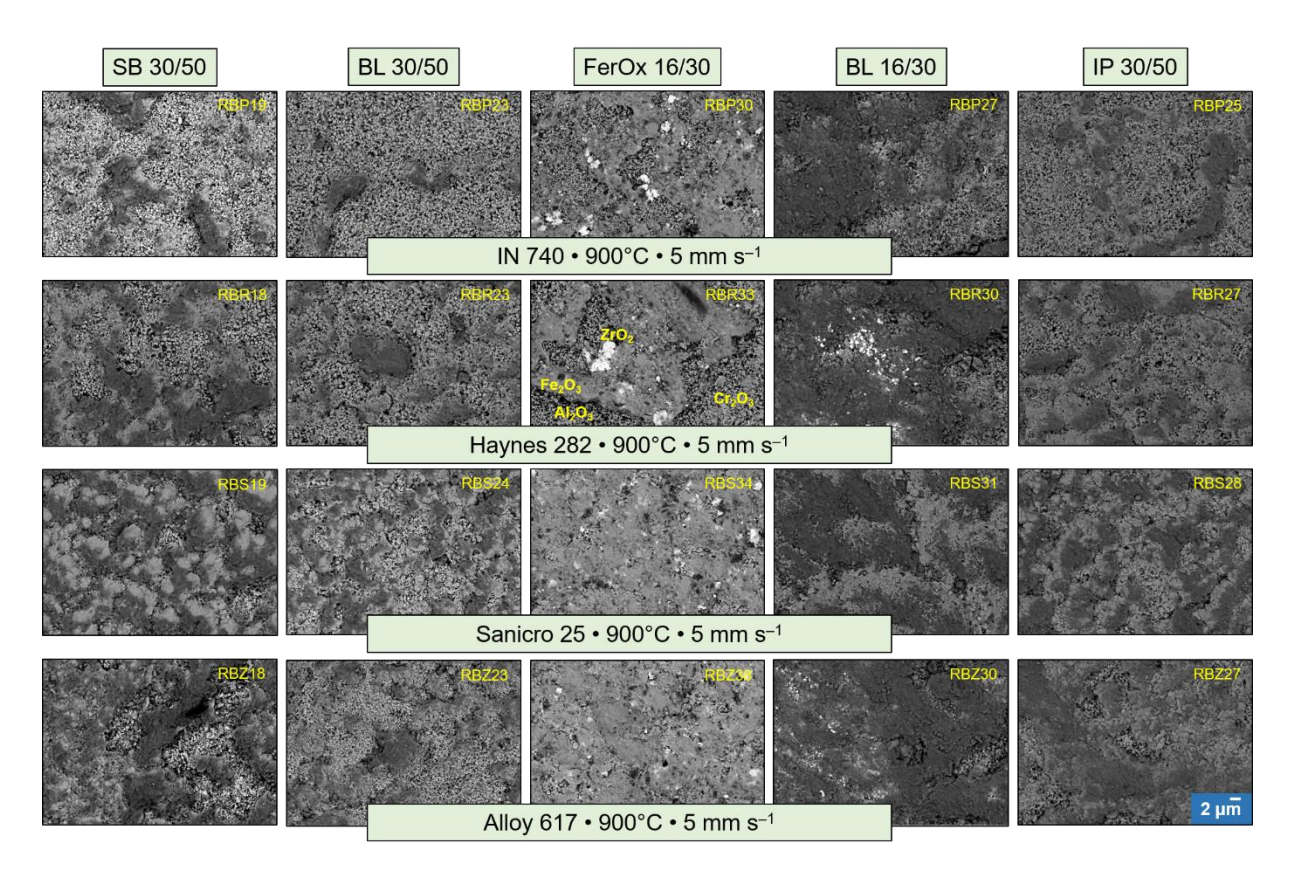


Figure 23. Topographical backscattered electron images of candidate materials after oxidation-erosion testing for 250 hours in air at 900 °C. Black coloration of the sample surface implies deposition of the bauxite-based granulate material.

The data from oxidation-erosion testing at 700°C showed minimal mass changes, ranging from +0.1 mg cm⁻² to -0.25 mg cm⁻², as anticipated due to the formation of a thin oxide scale at this temperature. Therefore, this report will focus solely on mass change data obtained at 900°C.

Figure 24 displays the effective mass changes of the studied materials during oxidationerosion long-term testing, utilizing the SB 30/50 granulate. The results indicated occurrence of erosion-wear, whereas the extent of degradation was different between the alloys studied. A comparison of the alloys following oxidation-erosion testing reveals that the least mass loss was observed for Alloy 617 (-2.5 mg cm⁻²), while the highest mass loss was noted for INCONEL 740 (-5.2 mg cm⁻²), followed closely by Haynes 282 (-4.9 mg cm⁻²). The results are in good agreement with the mass change data presented in Figure 20. The trend indicated the lowest mass loss for Alloy 617, particularly when it was tested with all granulates.

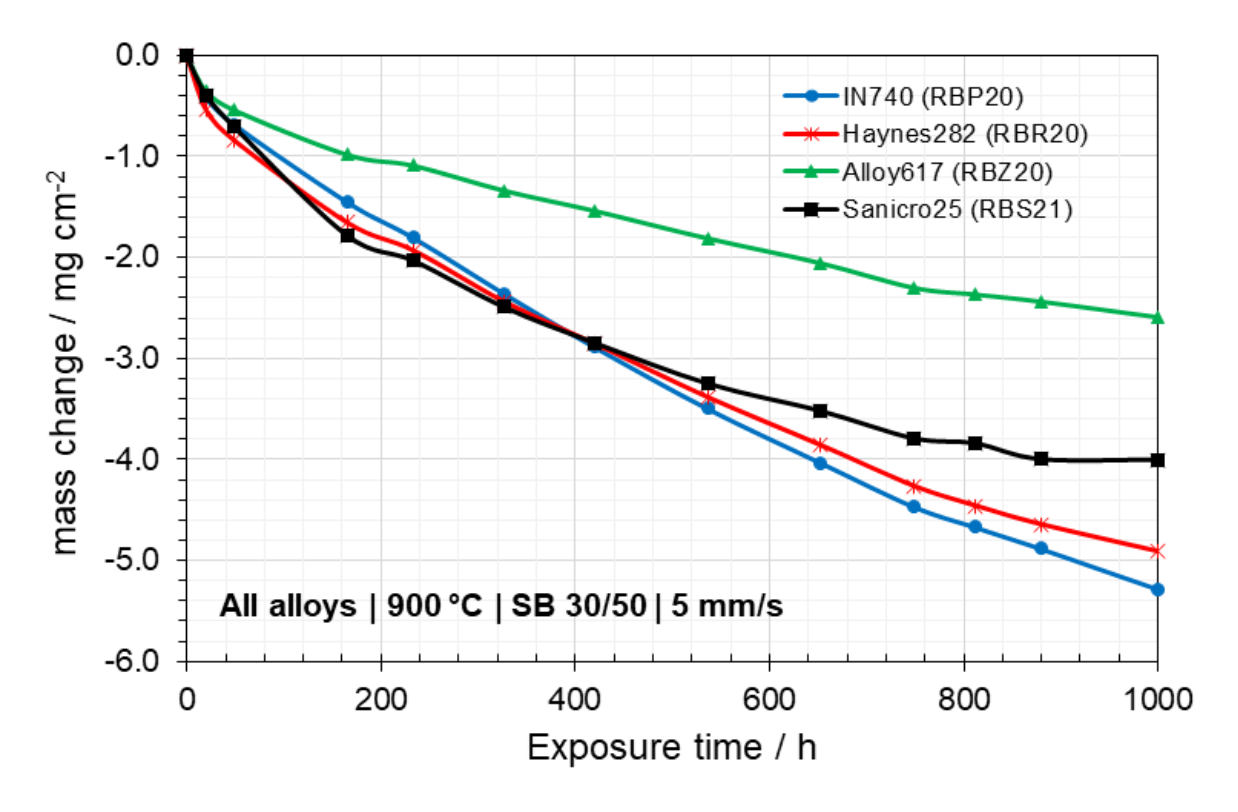


Figure 24. Effective erosion after 1000 h at 900 °C in air, using SB 30/50 (Gen 3) granulate with a flow rate of 5 mm s⁻¹.

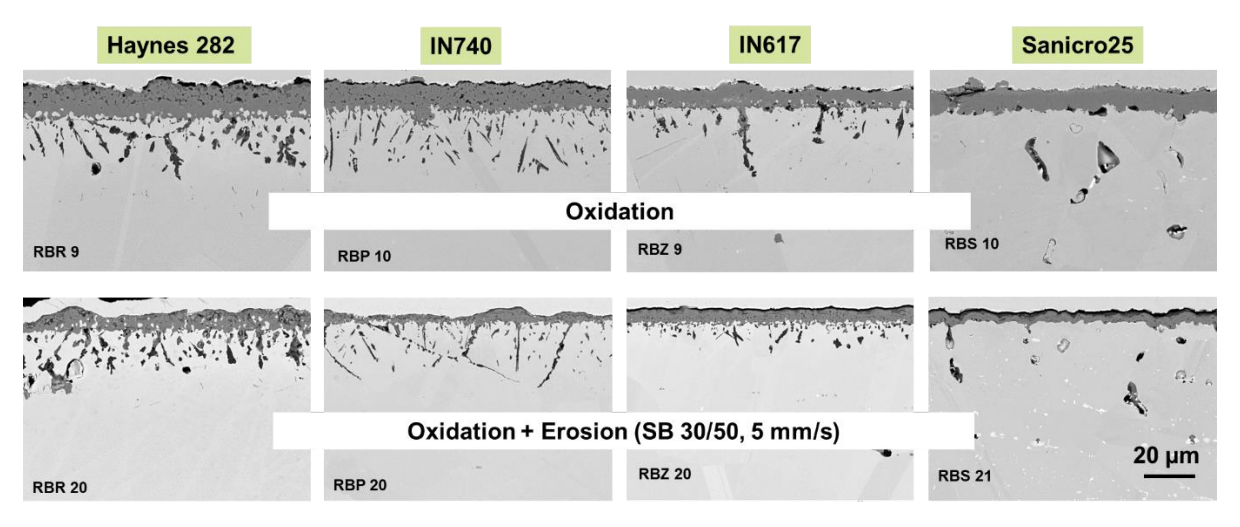


Figure 25. Backscattered electron images of cross-sectioned materials after cyclic oxidation and oxidation-erosion testing for 1000 hours in air at 900 °C. The images correspond to the weight change data in Figure 24.

Detailed analysis of the oxidation products revealed that the erosion was limited to the oxide scales.

The alloys with higher Ti-contents (IN740 and Haynes 282) having a higher mole fraction of the gamma-prime $Ni_3(Ti,Al)$ strengthening phase were expected to have a higher hardness at the test temperature compared to Alloy 617, which is commonly considered to be good for erosion resistance. However, the extent of erosion degradation was not decreased with increasing alloy Ti and Al contents (compare Figure 25) and the erosion rates were increasing in the order Sanicro25 < Alloy617 < IN740 < Haynes282. Based on the prevailing results it can be argued that the mechanical properties of the oxide scales play a more important role. In this sense, a high alloy content of Ti can be considered negative as it promotes p-type doping of chromia and thus formation of faster growing scales (compare with relative weight changes during isothermal oxidation exposure in Figure 4, Deliverable 4.1) with substantial amount of porosity, which can be susceptible to faster erosion. An interesting observation was granulate deposition, which occurred to a larger extent on surfaces of the less eroded alloys, i.e. IN617 and Sanicro25. This effect is shown in Figure 26.

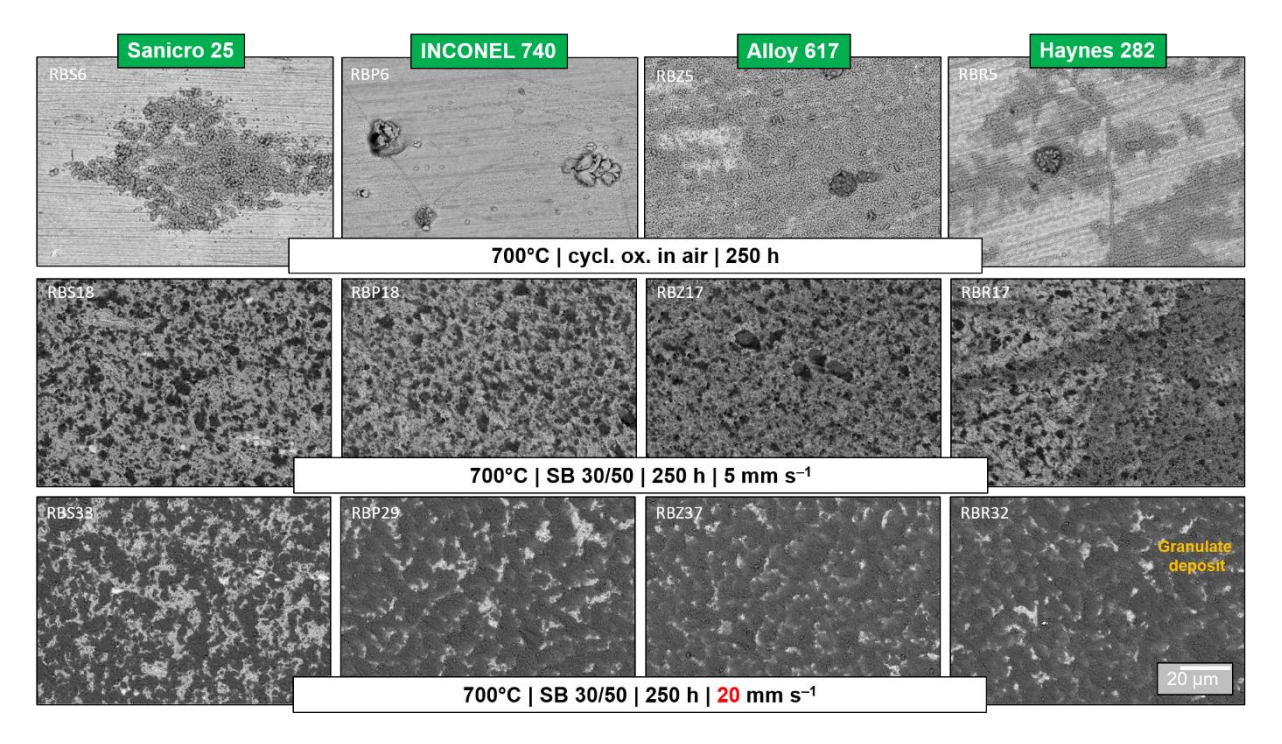


Figure 26. Topographical backscattered electron images of candidate materials after cyclic oxidation and oxidation-erosion testing for 250 hours in air at 700 °C. Black coloration within the sample matrix implies granulate deposition of the bauxite-based material SB 30/50.

At 900°C, there was no significant increase in granulate deposition on the material surfaces compared to 700°C exposure. This suggests that the extent of deposition is mainly influenced by the particle flow rate, as illustrated in Figure 26 (compare both flow rates, 5 mm s⁻¹ and 20 mm s⁻¹).

Finally, in addition to the oxidation-erosion testing, granulates were examined in their post-testing conditions to assess any self-impact.

Following the oxidation-erosion testing, the bauxite granulates, FerOx 16/30 and SB 30/50 were examined by SEM/EDX mapping analysis. Comparison with the as-received particles revealed no apparent deposition of material debris from specimen or specimen holder on the

granulate surface (refer to Figure 27) irrespective of variations in temperature (ranging from 600 to 900°C), particle flowrate (either 5 or 20 mm s⁻¹) up to 250 hours.

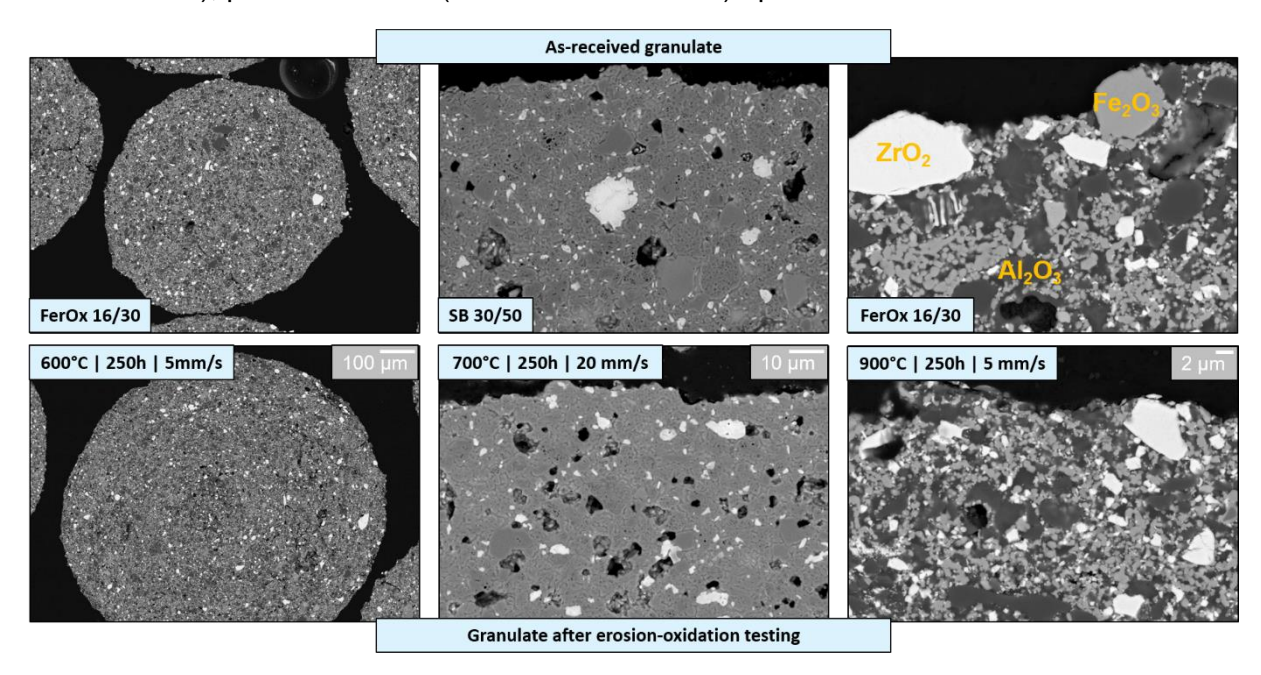


Figure 27. Comparison of selected granulates before (as-received) and after erosion-oxidation testing with particle flow rates of either 5 mm s⁻¹ or 20 mm s⁻¹.

The presented results indicate the importance of granulate deposition on the wear resistance of the studied materials. The deposition in turn seems to be affected by the surface morphology and composition of the formed oxide scales. Therefore, it appears to be important to study the effect of pre-oxidation and surface roughness of studied materials on their erosion behavior.

Further experiments on the effect of pre-oxidation were performed, utilizing FerOx 16/30 granules and a particle flow rate of 20 mm s⁻¹. Additionally, a test campaign is planned to study the wear of granulates on alloy surfaces, with various surface roughness values produced by grinding prior to oxidation-erosion testing.

Studies of Sanicro25 with different surface finish revealed that under the prevailing experimental conditions there is no substantial effect of the surface roughness on the erosion behaviour. SEM images in Figure 28 indicate very similar surface morphologies of all specimens. The dark surface layers are primarily the deposits of granulate dust, as can be clearly seen in the SEM/EDX maps in Figure 29. Only very thin Cr-rich oxide scales are formed (Figure 7f) indicating no substantial erosion.

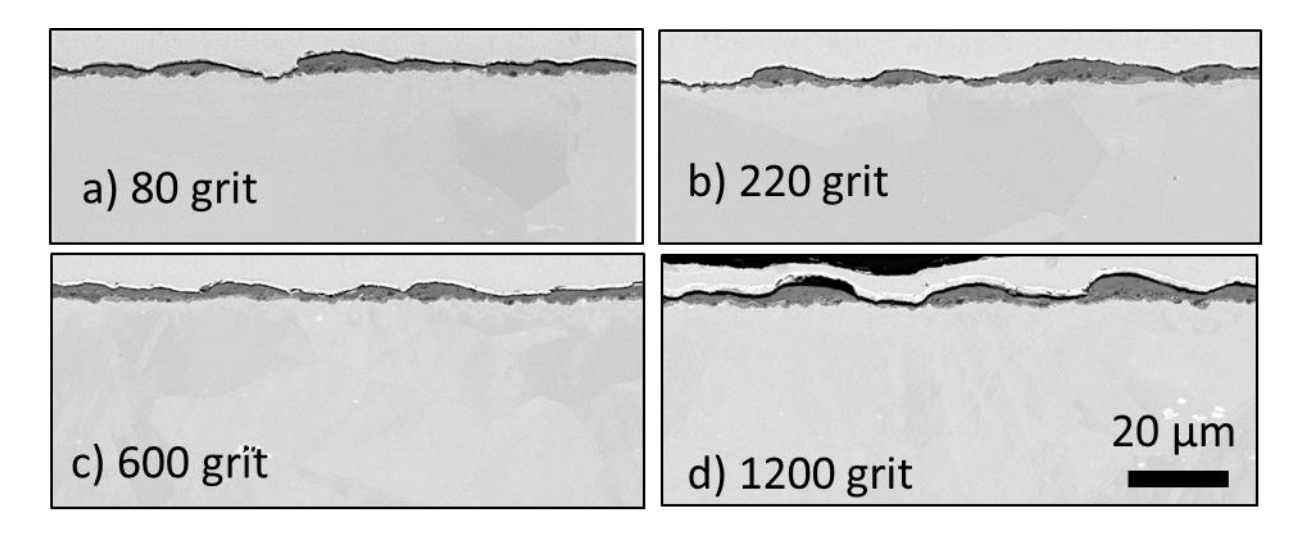


Figure 28 Sanicro 25 after erosion testing at 700°C for 250 h in a bed of FerOx16/30 particles with relative particle flow rate of 20 mm/s under ambient air

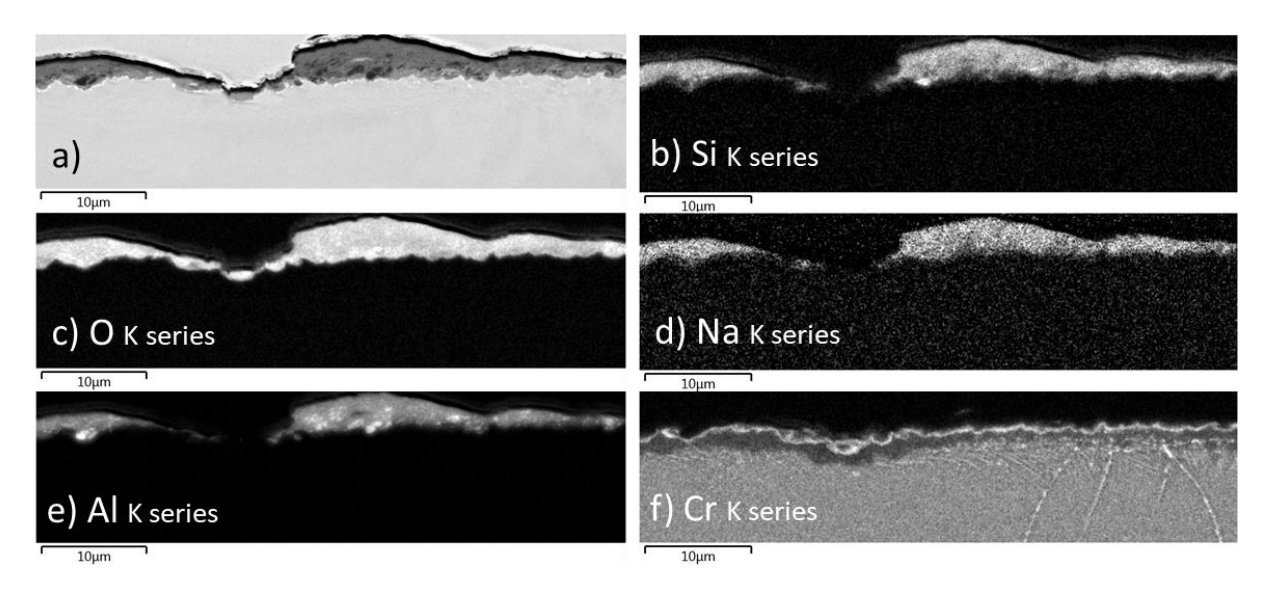


Figure 29: SEM/BSE-image (a) and corresponding elemental EDX-maps (b-f) of Sanicro 25 ground to 80 grit finish after erosion testing at 700°C for 250 h in a bed of FerOx16/30 particles with relative particle flow rate of 20 mm/s under ambient air

Figure 30 shows cross-sections of specimens that were pre-oxidized prior to the erosion testing. For comparison cross-sections of specimens after air oxidation for the same exposure time are shown. One can see that relative to the oxidation exposures, oxide scale losses due to erosion were less pronounced on sanicro 25 and Alloy 617 compared to IN740 and Haynes 282. The latter observation can be explained by the high Ti-contents of the latter two alloys. Consequently the oxide scales on the latter materials contain more Ti, causing p-type doping effect, which is known to produce fast growing oxide scales with porosity and lower mechanical strength more susceptible to erosion compared to denser oxide scales on sanicro 25 and Alloy 617.

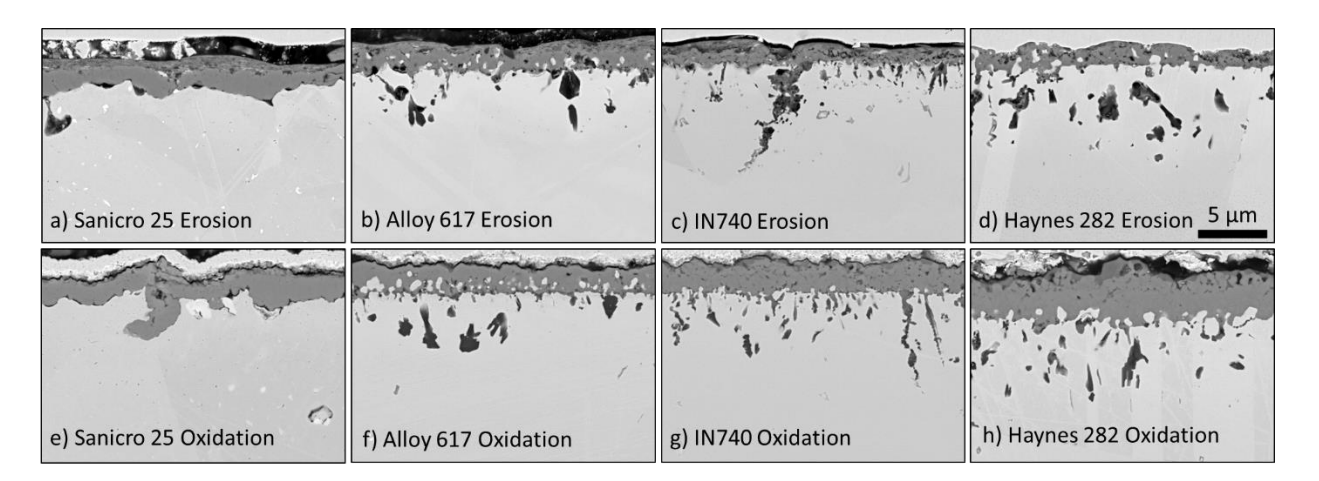


Figure 30: Specimens of studied state of the art alloys after testing: (a-d) Preoxidised at 900°C for 72 h with subsequent erosion testing at 900°C for 250 h in FerOx 16/30 granulate at relative particle speed of 20 mm/s; (e-h) Specimens after oxidation at 900°C for 250 h in lab air.

Novel developed materialss

FZJ performed testing of novel materials including Cr-based alloys produced by UoB and CrSi-coated Ni-base alloys (the latter coatings produced by Dechema). Erosion testing was performed using specimens rotating with a carousel-type specimen holder in hot granulate. The erosion tests were performed at 600, 700 and 900°C for Cr-based alloys and at 700 and 900°C for Cr-Si-coated Ni-base alloys in SB30/50 and FerOx16/30 type granulates and relative particle velocity of typically 5mm/sec.

Figure 31 shows an example of the mass change data obtained during testing at 600°C with only minor mass changes indicating no substantial damage. Cross-sections of the exposed specimens in Figure 32 show neither thick oxide scales nor substantial granulate material deposition on the metal surfaces. The latter observations are in agreement with the mass change data in Figure 31 as well as low growth rates of chromia scales at 600°C. Al-containing Cr-based alloys showed formation of Al-nitride precipitates within the alloy, which might originate from the manufacturing process as well as from nitridation reaction during testing.

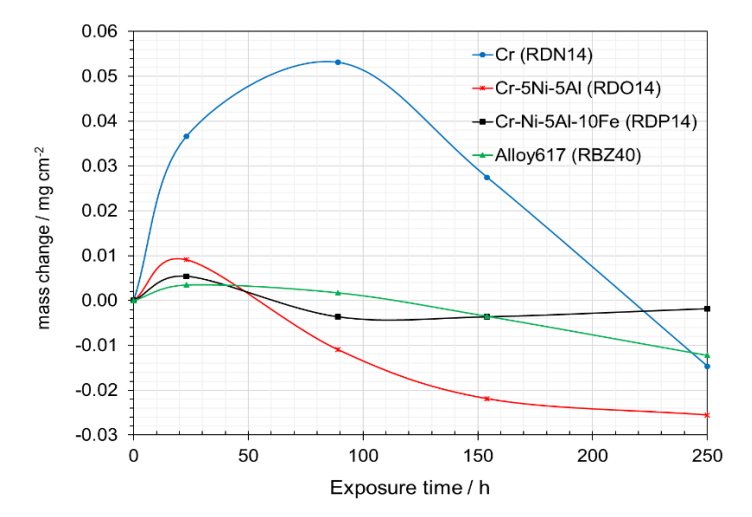


Figure 31. Mass change data measured during erosion testing at 600°C in SB30/50 granulate at 5 mm/s particle relative velocity of Cr-based alloys produced at UoB in comparison to Alloy 617

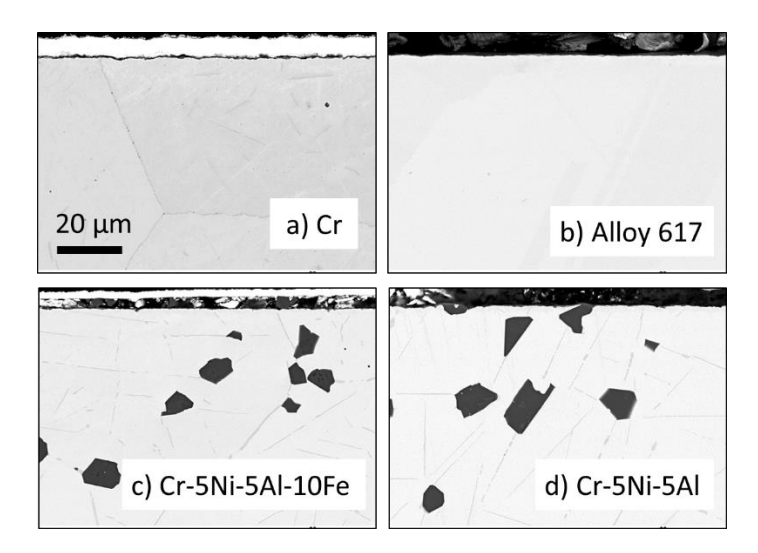


Figure 32. SEM cross-sections after erosion testing at 600°C in SB30/50 granulate at 5 mm/sec particle relative velocity of Cr-based alloys produced at UoB a), c), d) in comparison to Alloy 617 (b).

An example of the oxidation-erosion behaviour of the CrSi-coated Ni-based alloys is shown in Figure 33 and Figure 34. Positive mass changes were registered for the studied materials indicating scale growth or possibly minor granulate deposition. SEM cross-section analysis in Figure 34 indicated that only minor if any granulate deposition occurred on the specimen surface and the positive mass change in all studied materials was caused predominantly by the oxide scale growth. The CrSi-coating on Sanicro 25 showed minor amounts of scale spallation (visible in the SEM-image Figure 34 and in agreement with mass change in Figure 33). Figure 35 shows that Cr and Si diffuse into the base material to a depth of approximately 100 μ m. Such coating behaviour is known in many coating systems and represents an unavoidable effect in high-temperature applications.

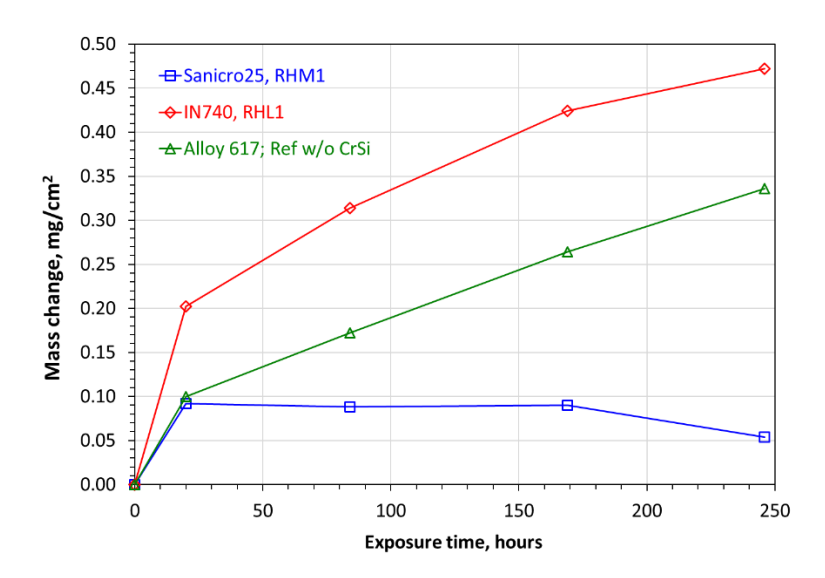


Figure 33. Mass change data measured during erosion testing at 900°C in Ferox 16/30 granulate at 5 mm/sec particle relative velocity of alloys with CrSi-coatings (by Dechema) in comparison to uncoated Alloy 617

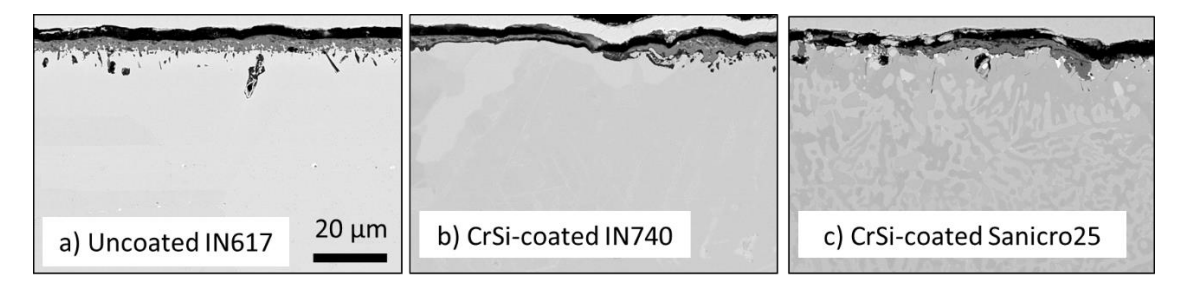


Figure 34. SEM cross-sections after erosion testing at 900°C in Ferox 16/30 granulate at 5 mm/sec particle relative velocity of CrSi-coated alloys (b,c) in comparison to uncoated Alloy 617 (a)

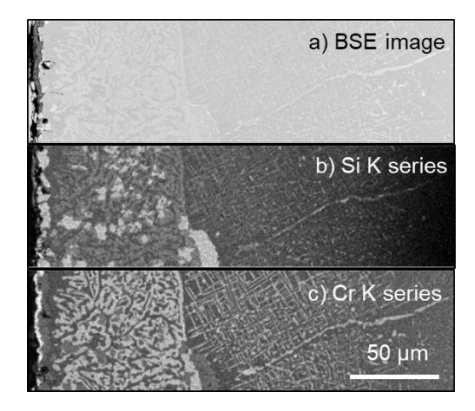


Figure 35. SEM cross-section of CrSi-coated Sanicro 25 after erosion testing at 900°C in Ferox 16/30 granulate at 5 mm/sec particle showing coating interdiffusion behaviour: a) BSE-image; b,c) EDX-maps for Si and Cr respectively

4.3 HOT-LONG TERM ABRASION TETS FOR CVR

The objective of this study was to comprehensively investigate the behaviour of newly developed materials and coatings in terms of oxidation, corrosion, wear, and mechanical properties under real particle flow conditions. The activities carried out focused on gaining a detailed understanding of the degradation mechanisms that affect the long-term performance and service life of these systems. As part of the research, the lifetime of the coatings was estimated. Furthermore, a thorough characterization of the novel materials and coatings to assess their performance based on key parameters was conducted.

4.3.1 Experimental procedure

A particle loop with an integrated test section was used to conduct the experiments. The layout of the facility is shown in Figure 36. Test specimens, in the form of tubes with outer diameters of 13,7 mm and 21.3mm and exposed length of 100 mm, were arranged in a staggered pattern at the centre of the test section, representing a section of potential heat exchanger tube bundle as illustrated in Figure 37. Abrasion testing was carried out over seven campaigns, reaching a total exposure time of 836 hours. During these tests, the temperature was maintained between 730-760°C, with a steady particle mass flow and near-wall velocities ranging 15-25mm/s.

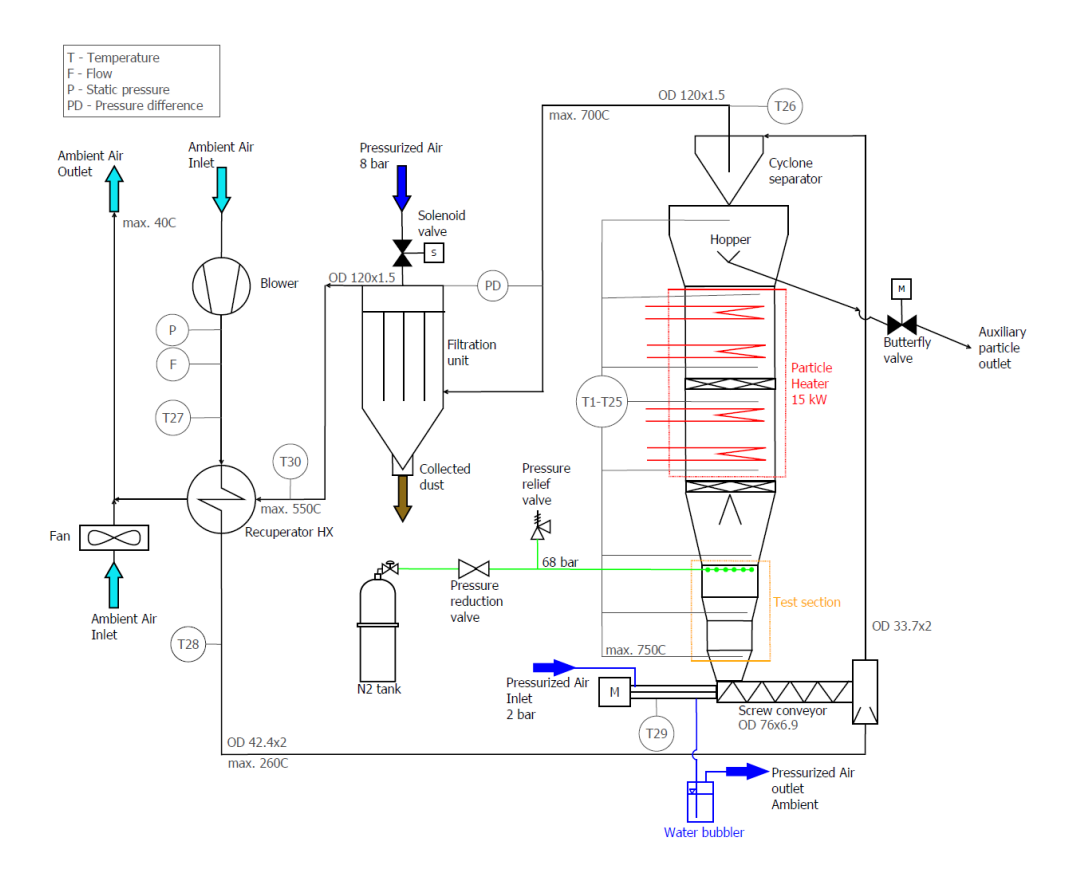


Figure 36: PID - Particle loop - hot long term test configuration.



Figure 37: Test section with the tested material samples.

4.3.2 Results and discussion

The study focused on materials such as Inconel 617, Inconel 740, Inconel 625, SS 316 (with/without coating TiAlSiN), Sanicro 25, new chromium-based alloys and Haynes 282 (with/without coating TiAlSiN). Furthermore, Inconel 617, Inconel 740, Haynes 282, and Sanicro 25 specimens with Cr-Si surface coating from project partner Dechema were also analysed. Surface morphology and internal structure were evaluated for all specimens using OM and SEM. The analysis included both the overall surface condition and detailed examination of cross-sectional cuts. In total, fifteen different types of specimens were evaluated. For each cross-sectioned specimen, three specific regions were analysed: the top, the side, and the bottom, as illustrated in Figure 38. These locations were selected because the oxide layer appeared to differ at each region, which is attributed to variations in particle flow and exposure conditions across the specimen surface. The thickness of the oxide layers was measured, and their composition was analysed using energy-dispersive X-ray spectroscopy (EDS) in combination with scanning electron microscopy (SEM).

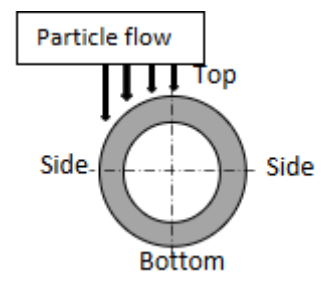


Figure 38: Three specific regions for analysis

On the top surface, a relief-like oxide layer was observed. In some cases, this layer was compact, as seen on Inconel 740 (see Figure 39a), while in other cases, such as with the Sanicro 25, a non-compact oxide layer with signs of spallation was formed (see Figure 39b).

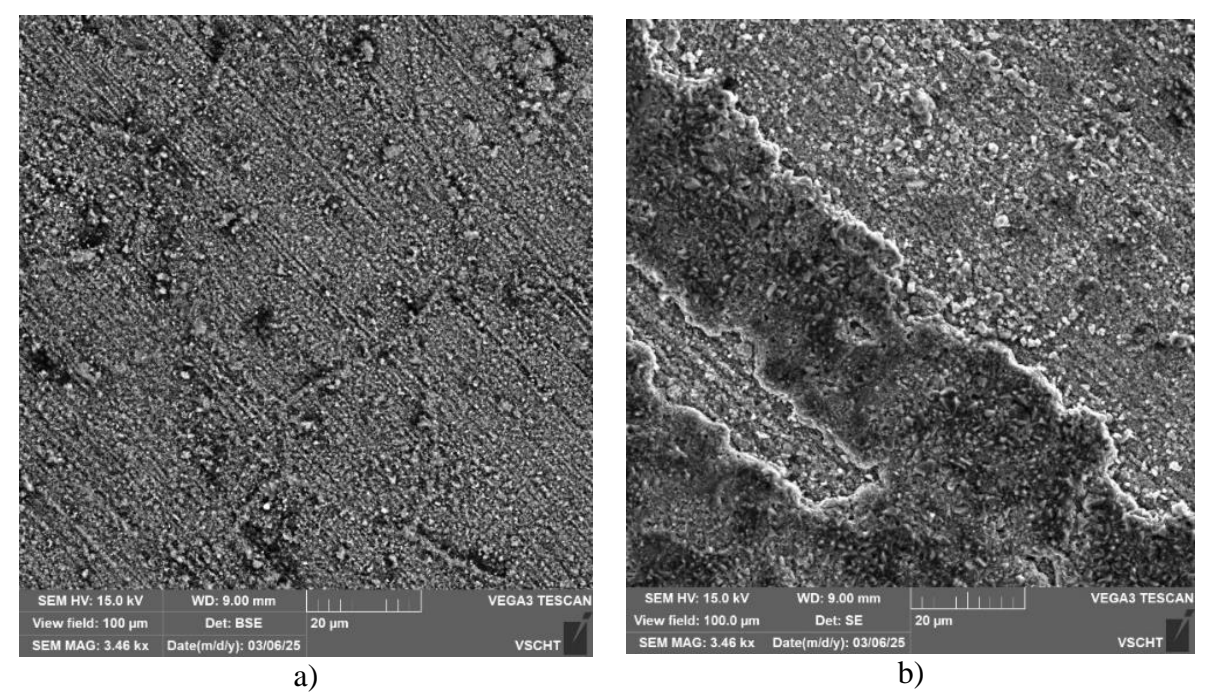


Figure 39: Top section. a) Inconel 740 with compact oxide layer. b) Sanicro 25 with non-compact oxide layer (spallation).

On the lateral sides of the specimens, a relief oxide pattern resembling grooves was identified (see Figure 40a). These groove-like features were formed as a result of the impact and erosion caused by abrasive particles. However, such groove formation was not observed in the specimens provided by Dechema, likely due to the presence of protective coatings (see Figure 40b). The specimens with Cr-Si coating exhibited surface pits in which fractured oxide fragments and erosive particles had accumulated. These pits likely originated from localized spallation and mechanical erosion, creating preferential sites for further degradation and the formation of secondary oxide layers. Such surface damage can negatively impact the long-term performance of the material by promoting localized corrosion and reducing the adhesion and protective effectiveness of surface coatings.

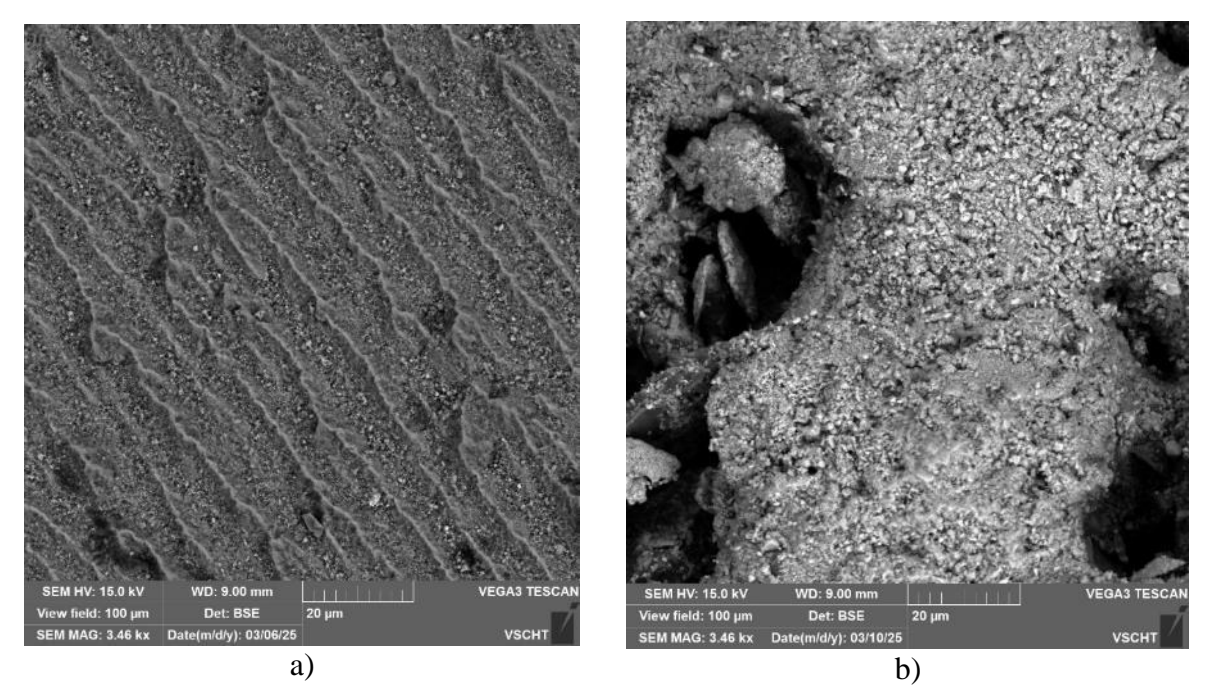


Figure 40: Side section. a) Inconel 617 with groove-like features. b) Inconel 740 sample with Cr-Si coating exhibited surface pits in which fractured oxide fragments and erosive particles had accumulated.

The bottom surface of the specimens was not directly exposed to abrasive particles. Consequently, the oxide layer formed here exhibited a morphology typical for the respective alloy or coating. In Figure 41a and Figure 41b, an intact coating layer TiAlSiN on Haynes 282 is shown as a representative example.

Cross-sectional analysis of the specimens provided valuable insights on the behaviour of novel developed chromium-based alloys from the University of Birmingham. For example, the Cr-Fe-Al-Ni alloy exhibited a non-compact protective oxide layer with visible cracking and progressing internal oxidation along grain boundaries (see Figure 42). In the case of alloys with Cr-Si coating, spallation of the oxide layer was observed, along with internal oxidation beneath the applied coating (see Figure 43).

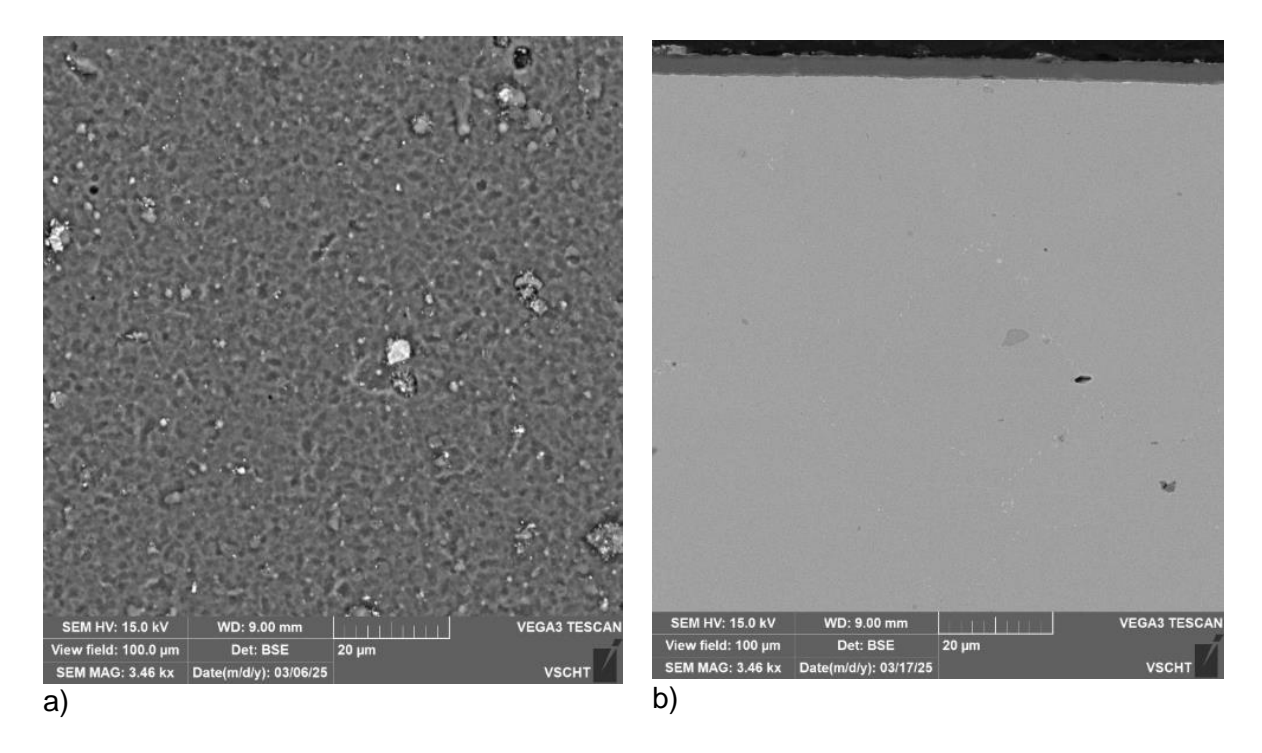


Figure 41: Bottom section. a) An intact coating layer TiAlSiN on Haynes 282. b) Cross-section SEM image of intact coating layer TiAlSiN on Haynes 282.

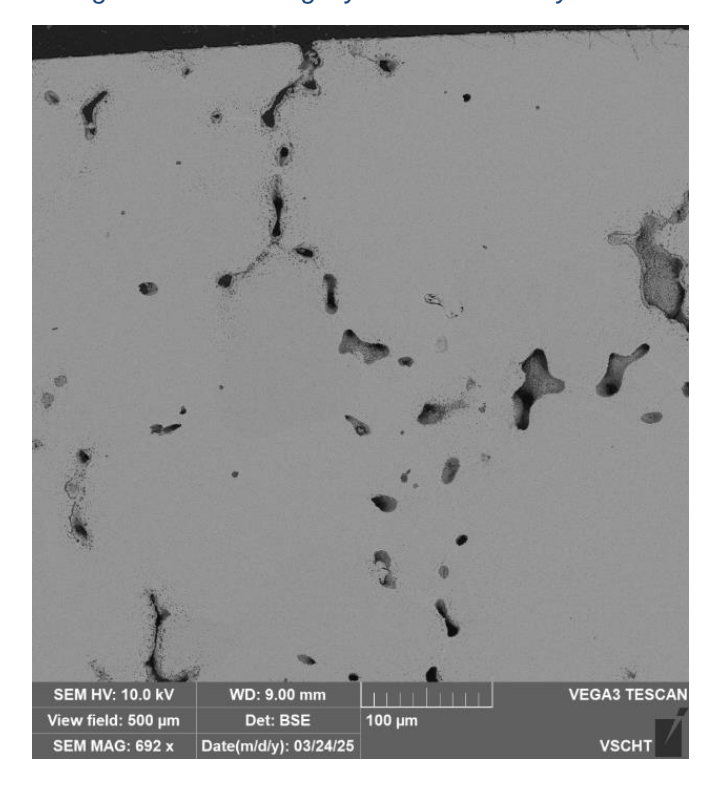


Figure 42: Cr-Fe-Al-Ni alloy with non-compact protective oxide layer with visible cracking and progressing internal oxidation along grain boundaries.

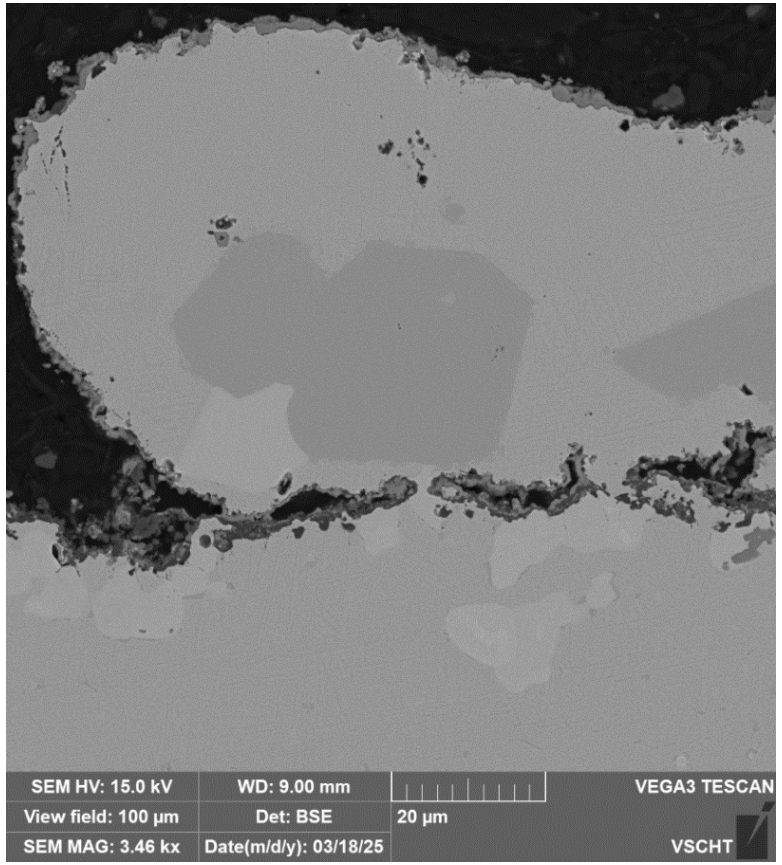


Figure 43: Haynes 282 with Cr-Si coating. Spallation of the oxide layer was observed, along with internal oxidation beneath the applied coating.

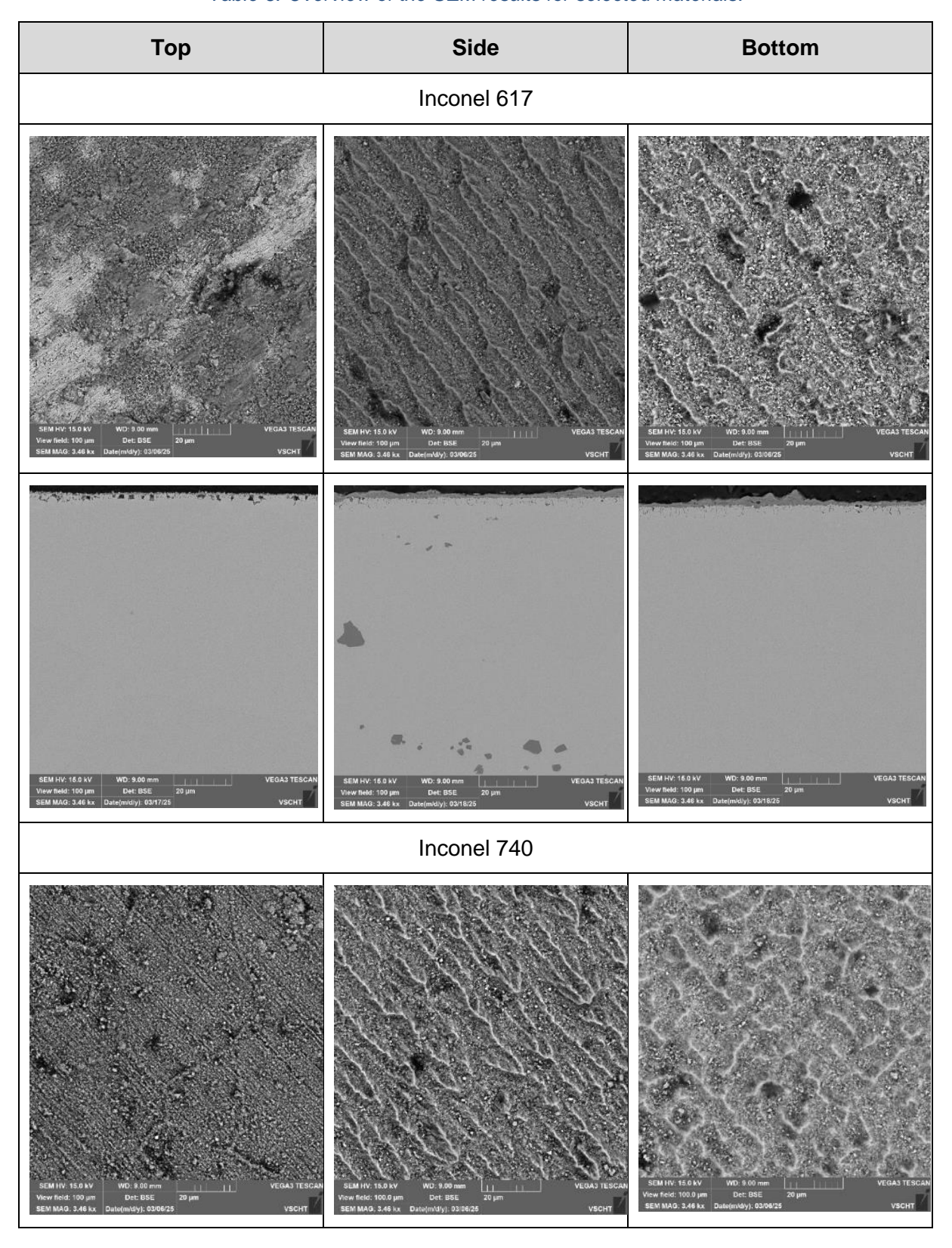
The following table summarizes the obtained information regarding the compactness of the oxide layer on the tested alloys.

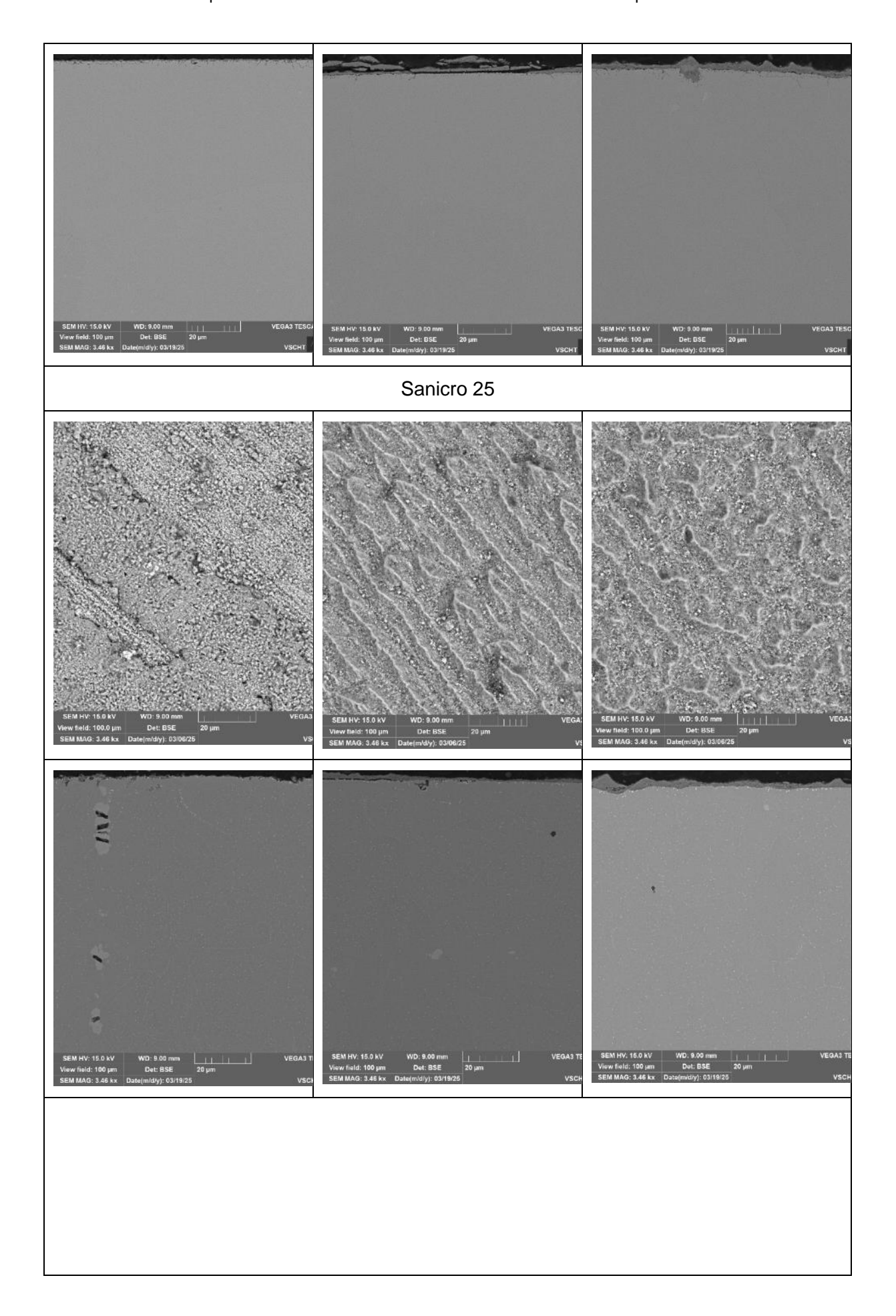
Table 5: Evaluation of the tested abrasion material samples

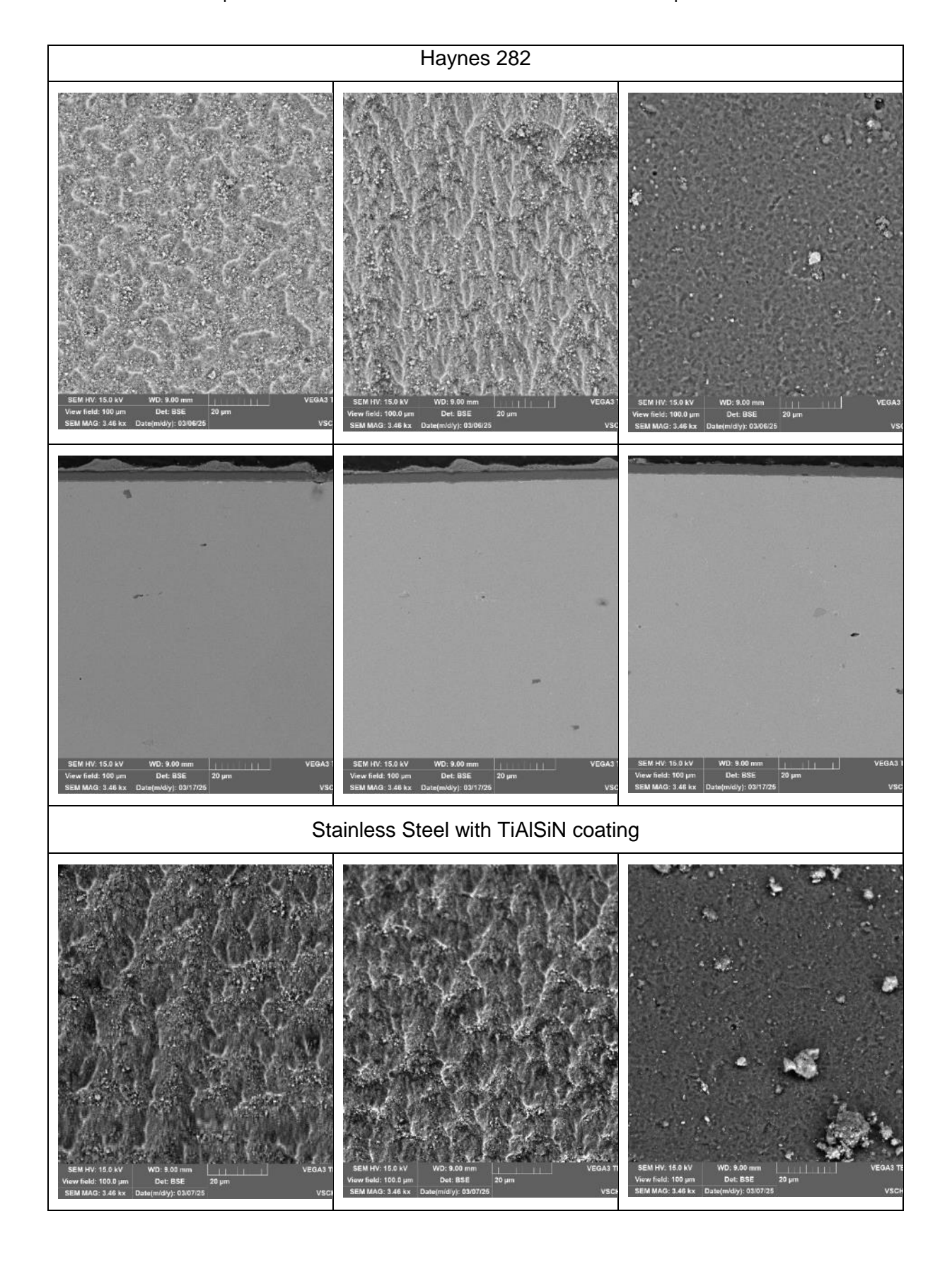
Sample	Compact oxidation layer	Non-compact -Spallation
Inconel 617	X	
Inconel 625	х	
Inconel 740	x	
Sanicro 25		X
Haynes 282	x	
SS316 + coating		X
Cr - UoB	x	
Cr-5Ni-5AI - UoB		X
Cr-5Ni-5Al - 10Fe - UoB	х	
Inconel 740 – Cr-Si coating		X
Inconel 617 - Cr-Si coating		X
Sanicro 25 - Cr-Si coating		X
Haynes 282 - Cr-Si coating	х	

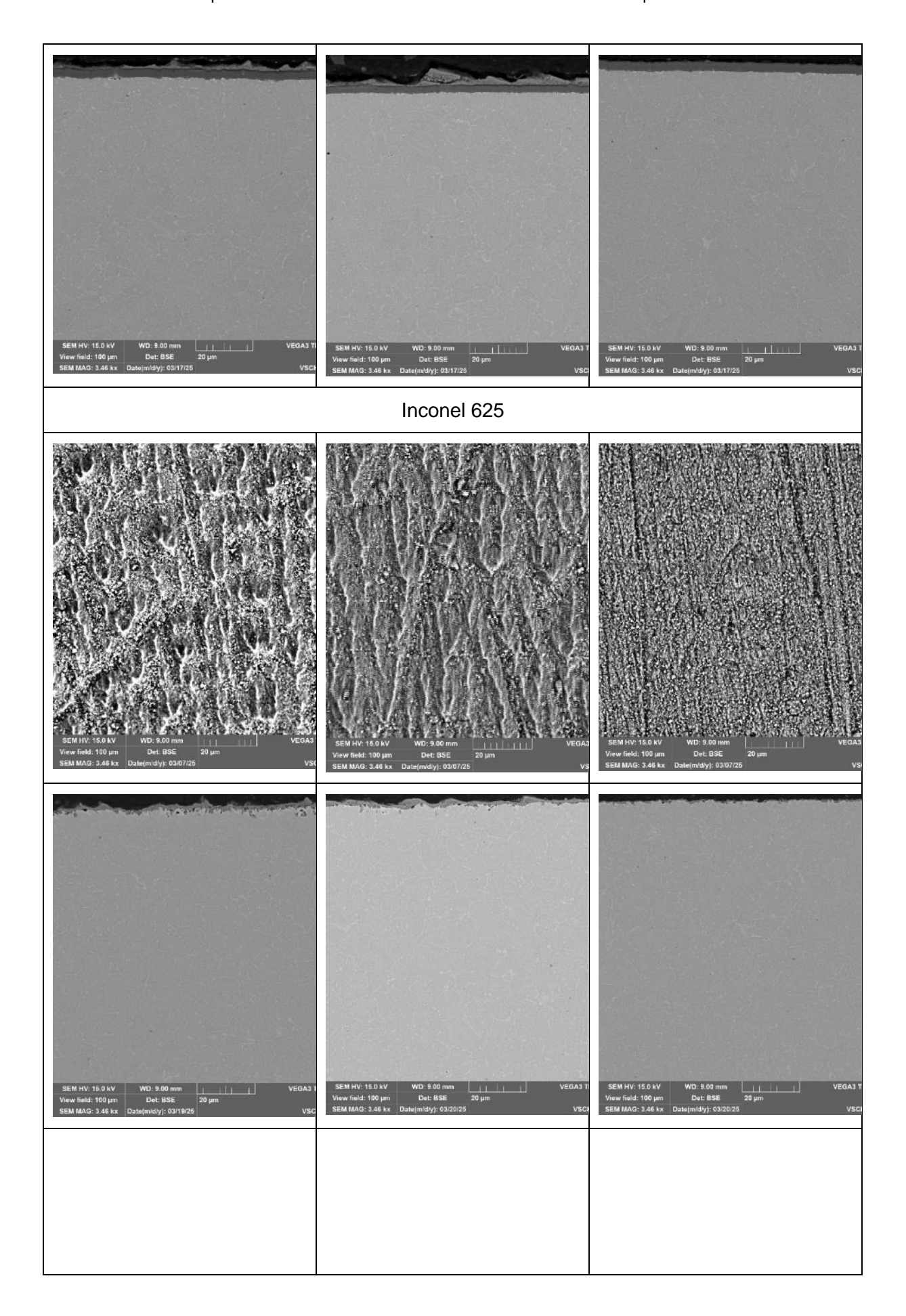
Table 6 shows scanning electron microscope (SEM) images of the specimens, with three regions—top, side, and bottom—analyzed for each. The field of view is $100\,\mu m$, and imaging was performed using a backscattered electron (BSE) detector.

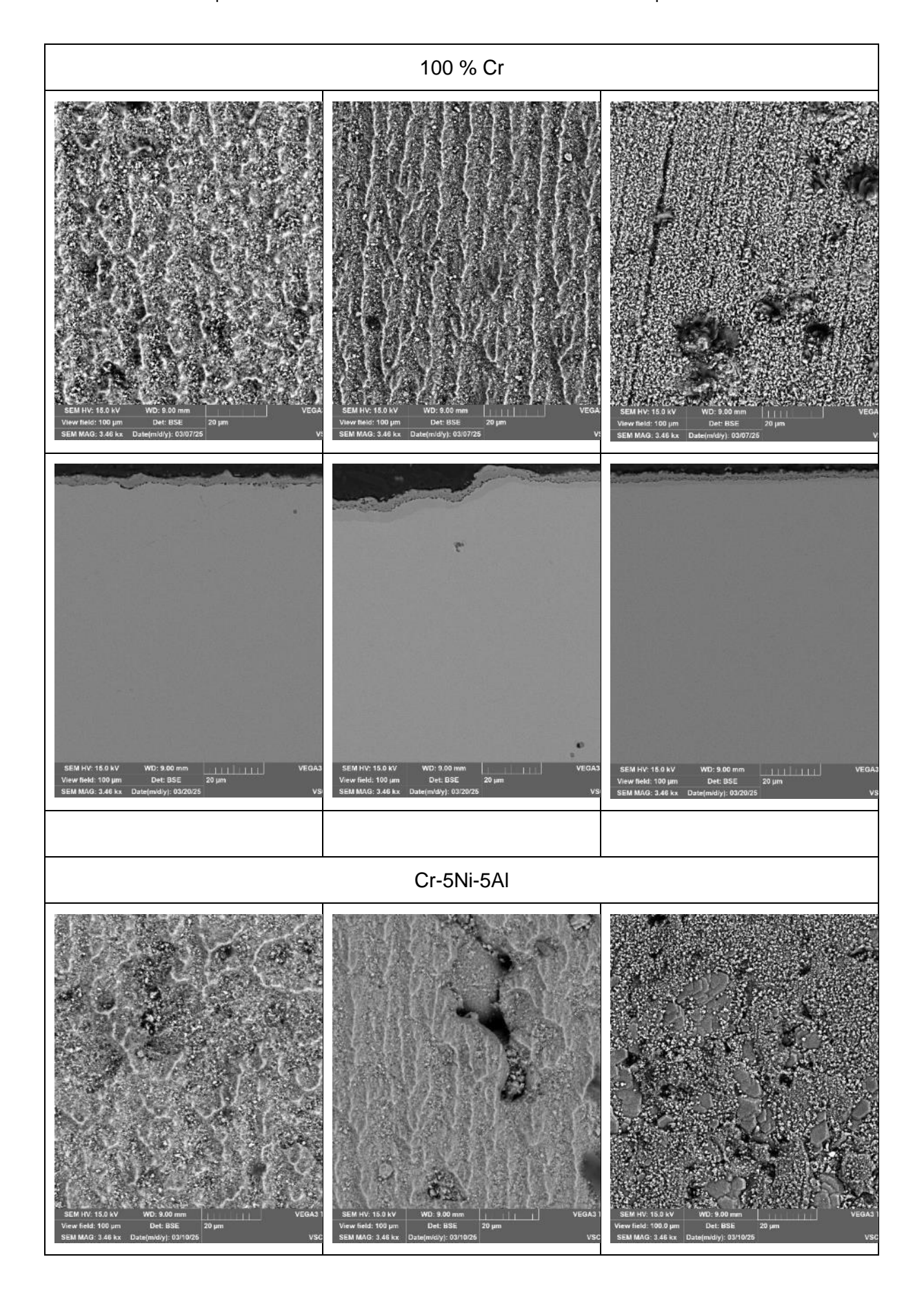
Table 6: Overview of the SEM results for selected materials.

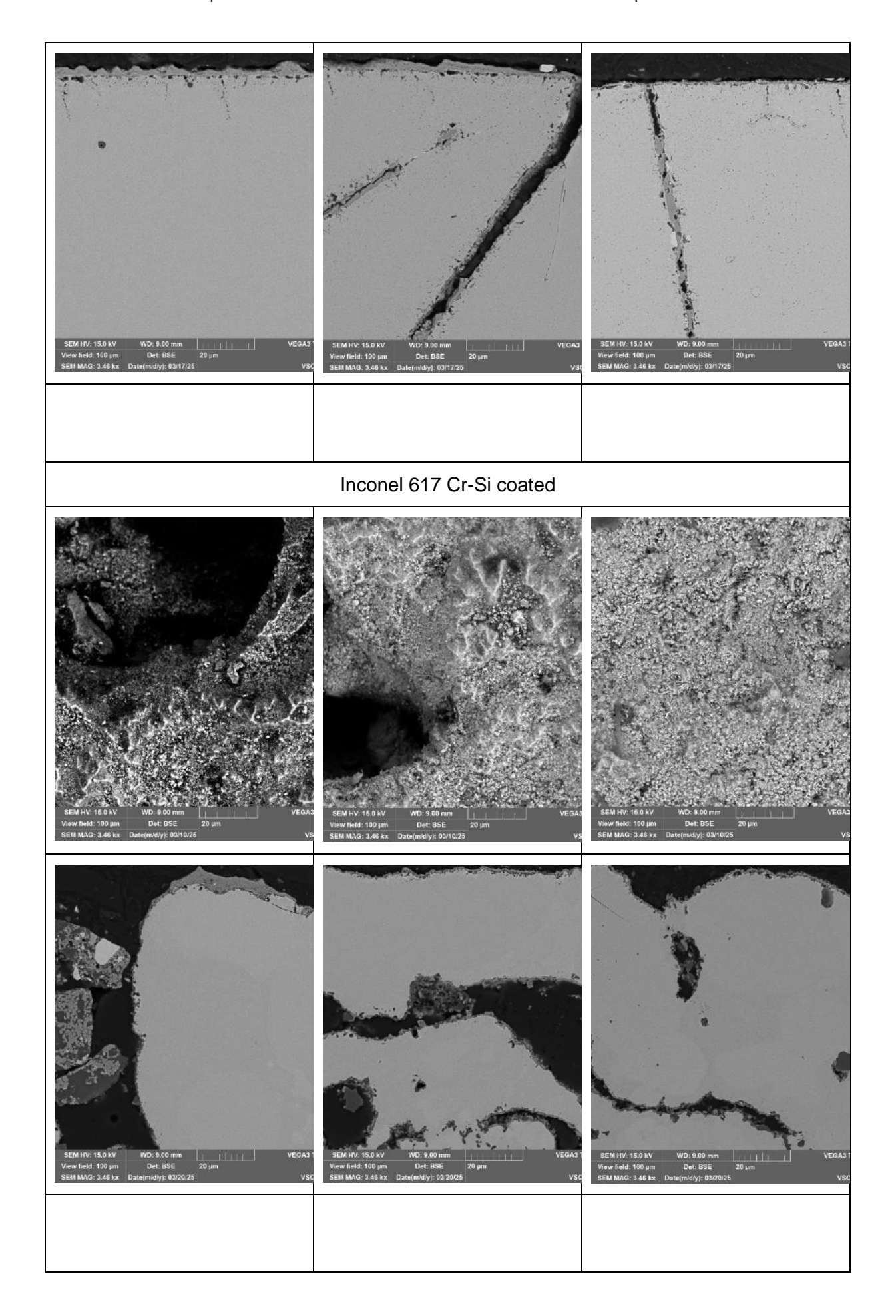


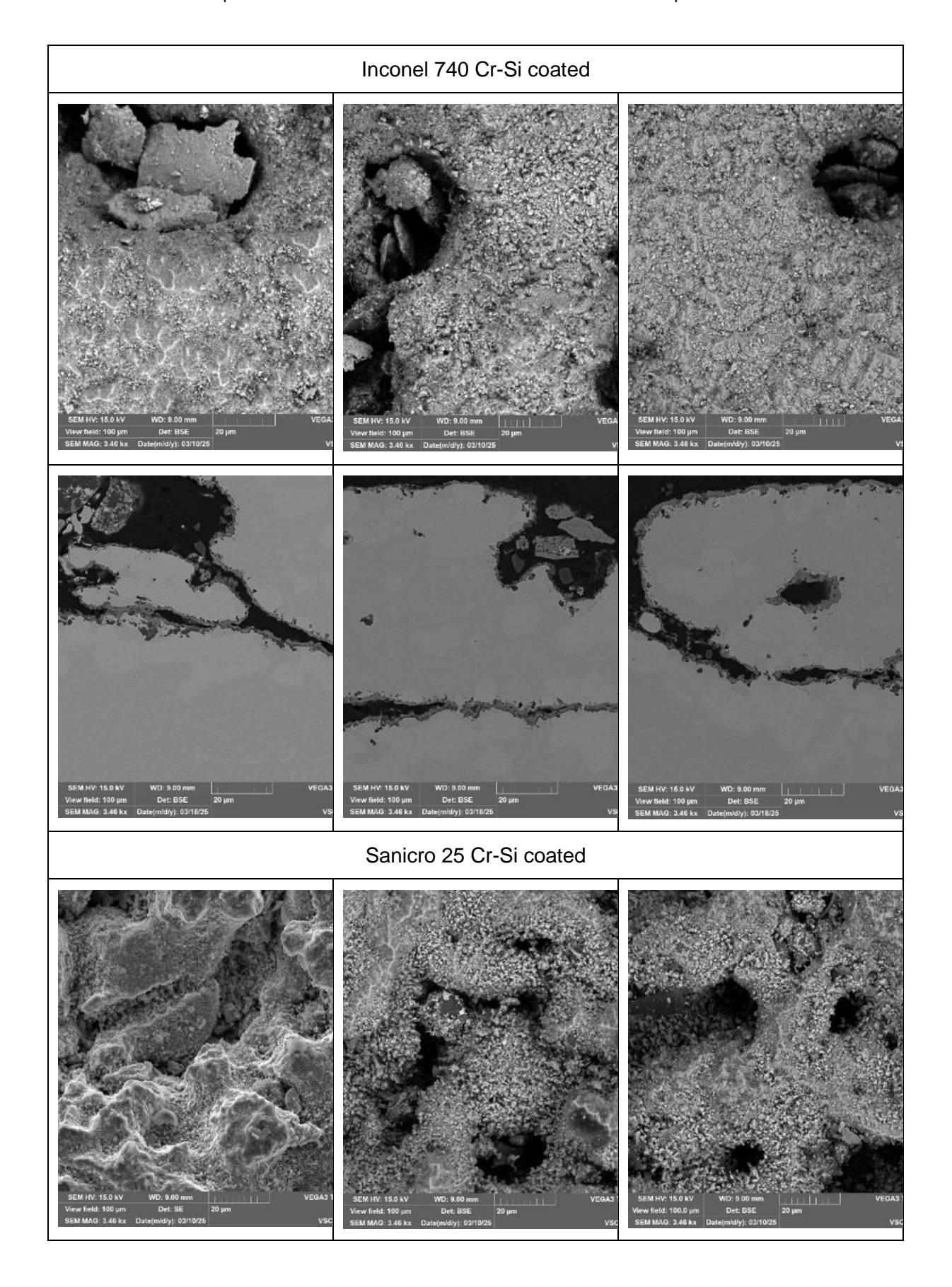


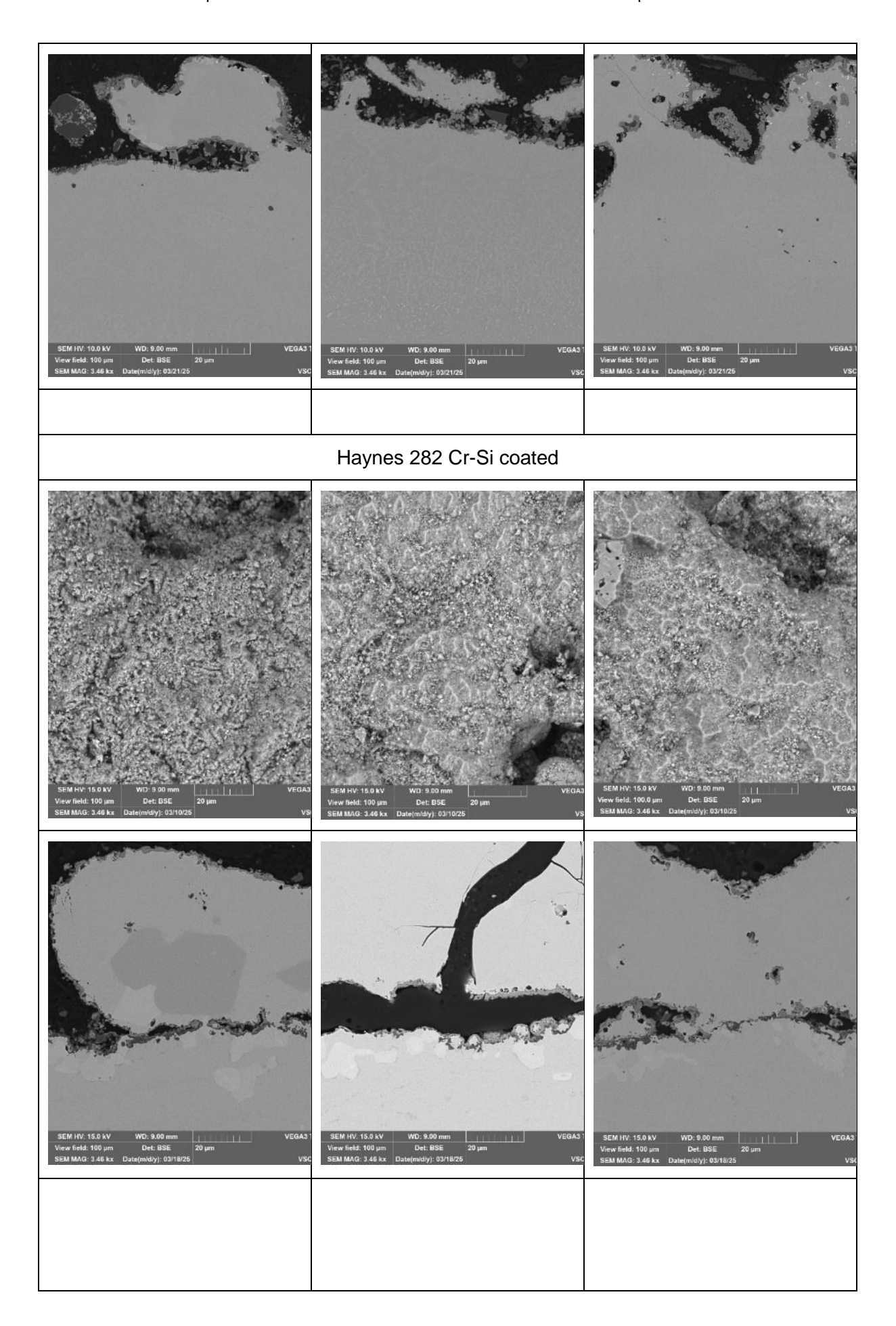


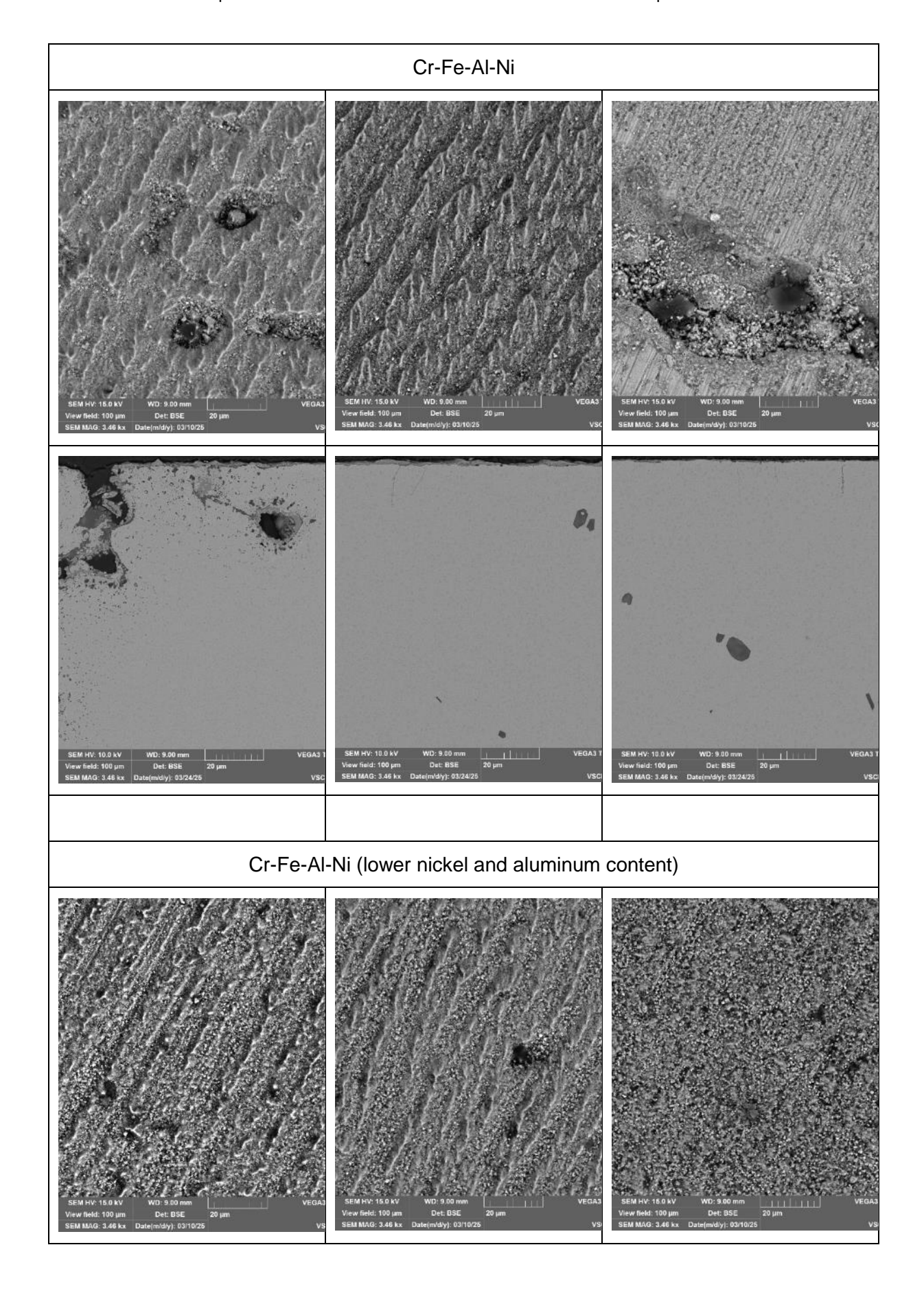


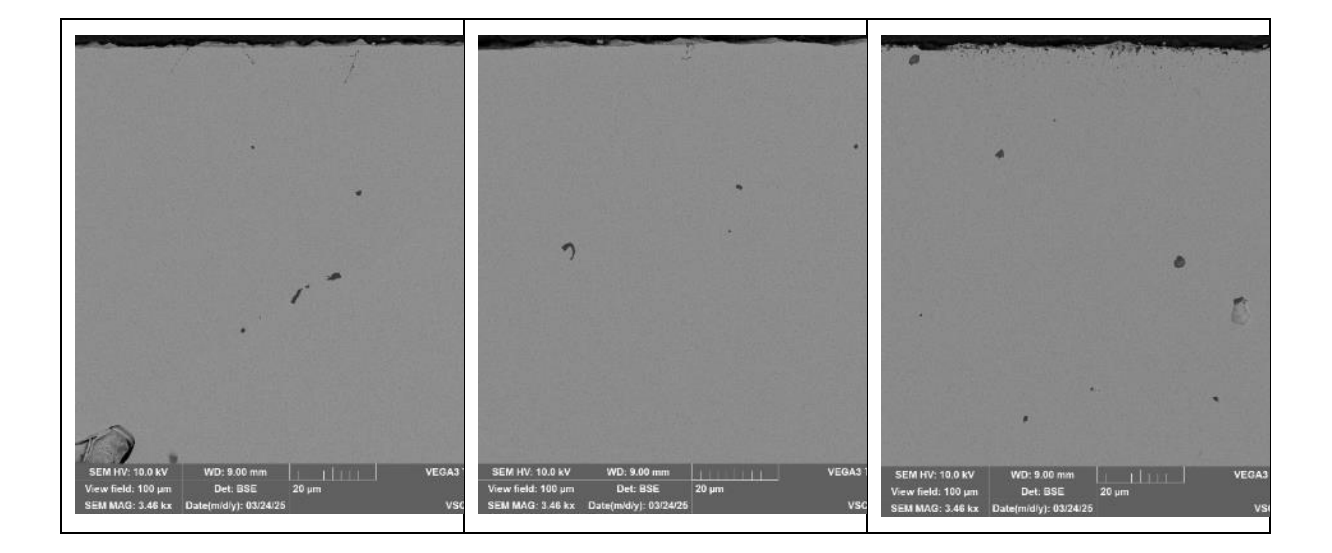












4.4 EVALUATION OF WEAR TESTS

Erosion tests were performed with the different particles in SOTA materials and coatings under same experimental conditions at 700°C and two particles velocities of 5 and 20 mm/s. Two different methodologies were used at Ciemat and FZJ laboratories, both of them based on the rotating movement of the specimens inside the particles.

At Ciemat laboratories, cylindrical specimen were tested in order to simulate the effect of particles in the actual tube geometry of the heat exchanger and to study the possible differences along the outer diameter of specimen. This methodology has shown that the particles are deposited mainly where the impact is greatest (front and right faces). The shape of the continuous deposits on more exposed faces shows the waveform typical morphology of wear/erosion degradation due to particles impact, which has not been observed in the free surfaces (backside) excluding the material removal in these zones.

On the other hand, FZJ tested planar specimens, with only front surface area of the specimen exposed to particles. With this methodology is possible to determine the effective erosion mass changes associated with granulate contact as result of the total weight measurements substracting the data obtained from cyclic oxidation (see Deliverable 4.1) and oxidation-erosion testing.

Results of weight measurements have shown a gain mass changes in the case of Ciemat laboratories, due to the effect of the simultaneously exposition of all the tube faces, while the loss mass changes at FZJ labs were obtained by subtracting the contribution of the oxidation of previous tests. These results are complementary taking into account that the use of the tube cylindrical simulates the real exposition of the tubes and the effective erosion has been determined in the front face of planar specimens.

Most relevant result, in both laboratories, is that granulated particles are deposited over the metallic surfaces. The extent of deposition is mainly influenced by the particle flow rate, testing time, material and surface finished. These results point out that further tests are necessary to determine the behavior of the particles that will be used, with special attention on the resistance of the optical coatings deposited over particles and the influence of their composition.

Deposits obtained in the case of P92 demonstrates that in some zones, an oxide layer is formed under the particle deposits, so an erosion-corrosion mechanism has to be considered and the hardness and mechanical properties of the particles may an important role. In the case of H282 and coatings, no oxide formation was detected and the deposits are only composed by the chemical elements of the particles. Particles deposition seems to have a protective effect on the material corrosion on H282 and coatings. However, this particle deposition has to be evaluated taking into account the possible effect on the heat transfer efficiency of the tubes.

FZJ analysis of the oxidation products revealed that the erosion was limited to the oxide scales and because of that these results indicate the importance of granulate deposition on the wear resistance of the studied materials. The deposition in turn seems to be affected by the surface morphology and composition of the formed oxide scales. Therefore, it appears to be important to study the effect of pre-oxidation and surface roughness of studied materials on their erosion behavior.

Regarding to the coating deposited over the metallic surfaces, a good resistance to erosion degradation has been proved with only an isolated detached zone in the case of P92 with the lower time and particle velocity, so it could be due to a non-detected previous defect. In addition, the particle deposits on the coatings are smaller and isolated, indicating better performance with the coating. The beneficial effect of the coating on Haynes 282 was demonstrated by the lowest weight gain, which is consistent with the lower particle deposition and no oxide formation observed in the specimen examination under all conditions.

The hot long-term test results, performed at CVR, show that all tested samples exhibit erosion patterns on the sides of the microstructure, corresponding to areas with a particle velocity gradient, which leads to uneven wear.

Furthermore, the nickel-based alloys, along with some of the experimental chromium-based alloys, developed a compact and uniform oxidation layer. In contrast, most of the coated samples, as well as Sanicro 25, exhibited signs of spallation.

5 MECHANICAL PROPERTIES

5.1 CREEP PROPERTIES AT CIEMAT

5.1.1 Experimental procedure

Tests were carried out under constant dead load in air according to ASTM E139 at the CIEMAT creep laboratory (Figure 44). The loading system for each machine consists of a standard lever arm design where a dead load is applied to the specimen once the test temperature is reached. The temperature is measured and controlled by three thermocouples, one in the lower, one in the middle and one in the upper part of the specimen. The testing temperature is measured with ±2°C in accordance with the ASTM E139 test standard. Specimen strain in creep tests is measured using a rod-in-tube type extensometer attached to the shoulders of the specimen. A linear variable differential extensometer (LVDT) is located at the lower end of the extensometer assembly outside the furnace.

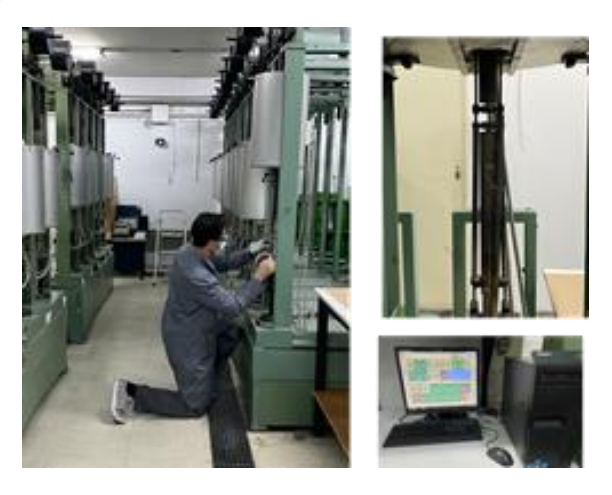


Figure 44. CIEMAT creep lab

The first geometry selected for the creep tests for the DFI and CIEMAT was a M8 re-designed specimen (Figure 45).

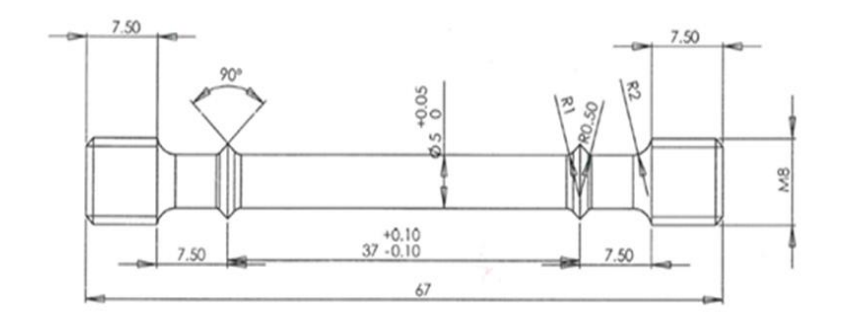


Figure 45. M8 specimen to perform creep tests at CIEMAT

As the high nickel alloys Haynes 282 and Inconel 740 show an exceptional creep strength at high temperature, the load needed to obtain time to rupture lower than 1000 hours exceed the load capability of CIEMAT machines. Therefore, a smaller geometry was selected to decrease

the load needed to achieve the same stress level. Specimen with a gage diameter of 3 mm was then selected, as previous experience exists at CIEMAT (see Figure 46).

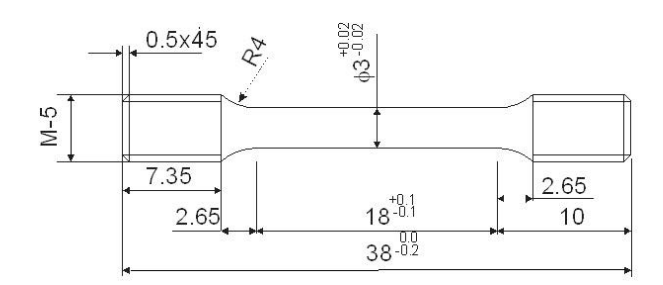


Figure 46. New M5 specimen for CIEMAT creep tests



Figure 47. M8 vs. M5 specimen. M5 specimen machined from M8 specimen.

The cross-section area of each specimen is measured at the center of the reduced parallel section before the tests. The constant axial force applied to the specimen is then calculated multiplying the cross-sectional area measured at room temperature by the selected stress value. Strain is calculated by dividing the extension measured by the LVDT by the extensometer gage length measured at room temperature before applying force to the specimen. As the extensometer is attached to the specimen shoulders, the reference length, Lr, for calculation of percentage extensions/elongations should be calculated. However, for the specimen geometry tested, the difference between the calculated reference length and the extensometer gauge length, is less than 0.5 % and then Lr can be chosen as equal to L0 or Le, in this case 18 mm as recommended at ISO 204 Uniaxial creep testing in tension test method

5.1.2 Test conditions

The predicted times to rupture were estimated from literature, from the materials specifications and from the allowable design stresses included in the ASME Code (see Deliverable 1.3) in order to obtain representative data during the project. Therefore, in order to obtain the creep properties, it was necessary to create three groups with comparable stress levels and times to rupture.

CREEP TESTS 700°C (Constant load (MPa))					
Time to rupture (h)	In740	H282	IN617	San25	P92
<1000	400		220		70
<700	450		23	30	80
<500	500		250		100
<100	550		30	00	150

Table 7. Initial creep test matrix

In WP3, tensile tests were performed at CIEMAT to determine yield strength (Rp02, MPa), ultimate tensile strength (Rm, MPa), percentage total extension at maximum force (Agt %), percentage total extension at fracture (A, %) and percentage reduction of area (Z, %) for each SOTA material at temperatures between room temperature and 760 °C. Figure 48 presents the Stress [MPa] – Strain [%] curves obtained:

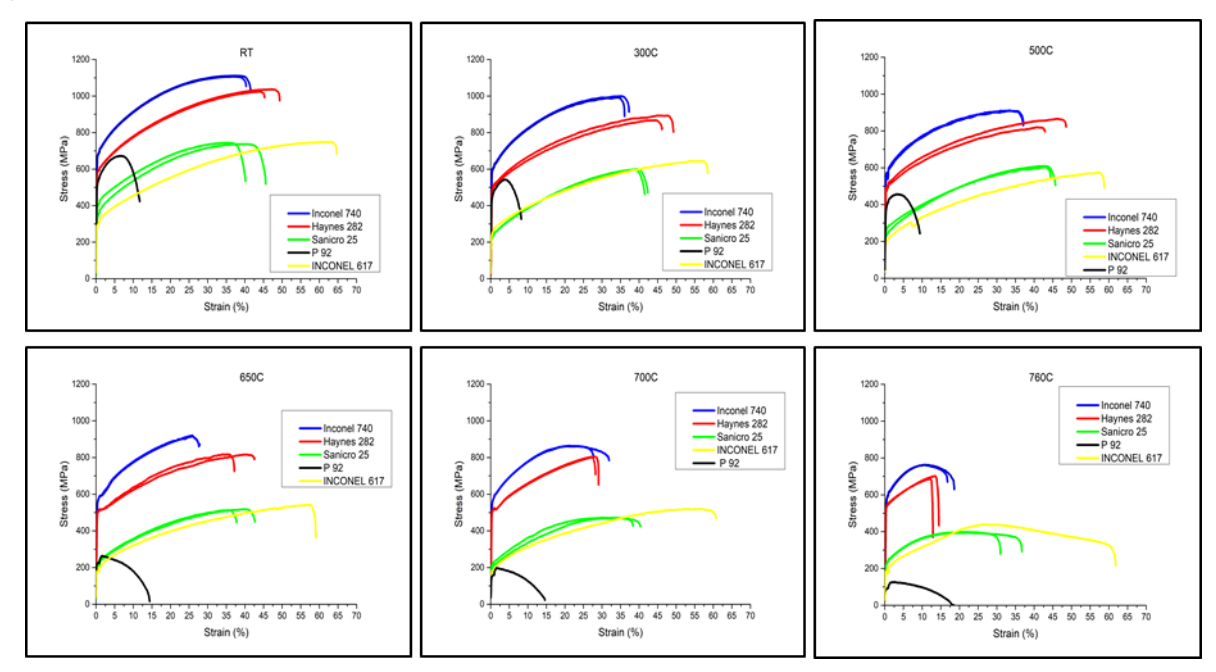


Figure 48. Tensile curves obtained for each SOTA material.

The following table summarizes the tensile properties obtained for SOTA materials at 700°C:

Rm A Z Agt **Rp02 Material** T(°C) (MPa) (%) (MPa) (%) (%) **IN740** 700 883 22 **565** 29,8 20,7 H282 700 809 28 507 28,7 20,8 San25 700 479 32 203 39,4 28,7 **IN617** 700 527 55 180 60,8 40,0 1,72 207 154 14,6 85 P92 700

Table 8. Tensile properties

The ½ Rp02 or/and 1/3 Rp02 criterion is widely used to design the creep test matrix according to the design codes. Due to the high creep resistance of the tested material, the load values selected are close to the value of the yield strength value to achieve rupture times within the COMPASCO2 project duration.

Table 9 summarizes the test matrix carried out by CIEMAT in air. In addition, P92 alloy was tested to complete the study of all candidate materials (candidate material to be used with coating) and to study the effect of the mechanization and the sample size.

Alloy	Sanicro 25	IN617B	Haynes 282	IN740	P92
Stress (MPa)	300, 250, 230, 220	300, 250, 230, 220	550,500, 450, 400	550, 500, 450, 400	150, 100, 80.70

Table 9. Applied stresses for the creep tests in air at CIEMAT.

5.1.3 Results and discussion

Table 10 summarizes the creep results obtained for each SOTA material. The CIEMAT creep laboratory was affected by a major refurbishment work of the building and consequently several power shutdowns occurred. For this reason, interrupted tests are also reported here. Interrupted creep tests are valuable tests to calculate the minimum creep rate if the interruption occurs at the secondary creep stage. It was also found that machining miniature specimens from large specimens caused defects in the specimens (particularly on the head thread), resulting in shorter times to failure. These tests were discarded and new test were performed, confirming this effect. It is also the reason why two tests are still ongoing.

 	Strain at	Minimum

Table 10. Creep results obtained for H282 at 700 °C.

H282	tr (h)	Strain at rupture (%)	Minimum strain rate (/h)
	829	13.3	6.71E-06
<1000h (400MPa)	168**	2.17	1.11E-05
(100 4)	40*	Stopped*	-
<700h	593	8.56	6.38E-06
(450MPa)	141*	Stopped*	1,11E-05
<500h (500MPa)	391	6.39	1.15E-05
<100h (550MPa)	90	2.76	2.81E-05
(*): Interrupted tests (**): Failed tests (mechanization of the specimen)			

Table 11. Creep results obtained for IN740 at 700 °C.

IN740	tr (h)	Strain at rupture (%)	Minimum strain rate (/h)		
<1000h	680	10.5	2.30E-05		
(400MPa)	209**	10.36	7.31E-05		
	652*	Stopped*	2.06E-05**		
<700h (450MPa)	523	6.43	1.15E-05		
	315	11.07	1.01E-05		
<500h (500MPa)	127	3.70	2.21E-04		
<100h (550MPa)	74	4.67	1.36E-04		
(*): Interrupted tests (**): Failed tests (mecha	(*): Interrupted tests (**): Failed tests (mechanization of the specimen)				

Table 12. Creep results obtained for IN617 at 700 °C.

IN617		tr (h)	Strain at rupture (%)	Minimum strain rate (/h)
40001-		1275	ON-GOING	8.70e-06
<1000h (220MPa)		1207***	Stopped*	9.64E-06
		257*	Stopped*	-
<700h		1182***	ON-GOING	1.11E-05
(230MPa)		338*	Stopped*	1.16 E-05*
<500h (250MPa)		308	5.77	2.07E-05
<100h (300MPa)		50**	Stopped*	-
(*): Interrupted tests (**): Failed tests (mechanization of the specimen) (***): Test still running.				

Table 13. Creep results obtained for Sanicro25 at 700 °C.

San25	tr (h)	Strain at rupture (%)	Minimum strain rate (/h)
	1058*	Stopped	3.52E-05
<1000h	1016	24.57	4.35E-05
(220MPa)	245*	stopped	-
	271*	stopped	-
<700h (230MPa)	485	22	1E-04
<500h (250MPa)	149	29	1.07E-04
<100h (300MPa)	123	28	1.30E-04

Figure 49 shows the creep curves of the tested materials in air. The need for re-testing due to machining problems means that there are tests still running on IN617 alloy. Nevertheless, IN617 (solid-solution strengthened Ni-based alloy) showed a significantly longer creep rupture life than Sanciro25 steel under the same creep test conditions. Sanicro 25 shows high creep elongation as expected for an austenitic steel. For the γ '-strengthened nickel base alloys, H282 shows higher creep rupture life compared to IN740.

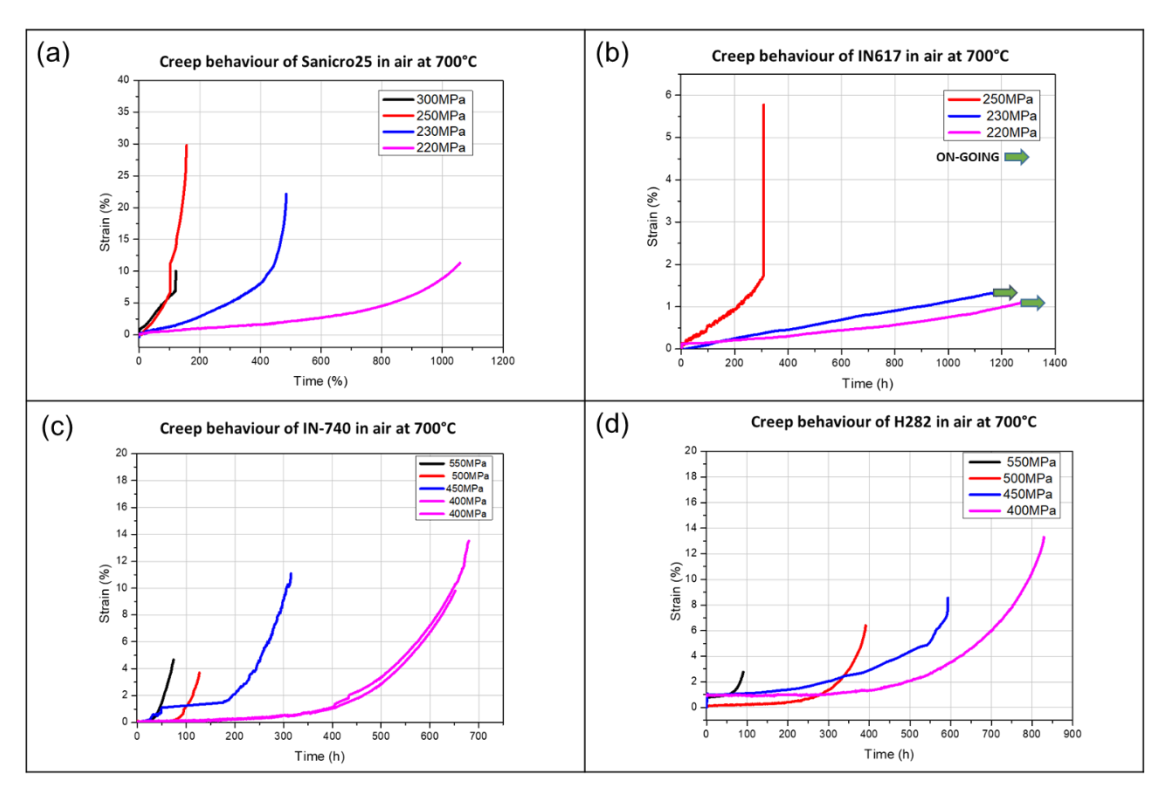


Figure 49. Creep curves of (a) Sanicro 25, (b) IN-617B, (c) IN-740 and (d) Haynes-282 in air at 700°C. Please note the varying x- and y-axes in the respective diagrams.

Figure 50a shows the minimum creep rates obtained at 700°C versus the applied stress for each material. The H282 alloy shows the minimum strain rate values following the IN617. The IN740 alloy shows a large scatter in the trends shown, highlighting how the use of miniature samples can show large scatter. Further testing should be carried out in the future to better understand this unexpected behaviour. However, the results for the other alloys seem to be in good agreement with the stress exponent. The austenitic steel Sanicro 25 shows the highest minimum creep rates among the tested alloys.

The Larson-Miller parameter (LMP) relationship is used to predict the creep rupture life for the investigated alloy (see Figure 50. b). LMP was calculated by the equation:

$$LMP = T \cdot (\log(t_r) + C)$$

where, T is creep testing temperature in K, t_r is the rupture time. C is the Larson-Miller constant. The value of the C constant for metallic materials, particularly for steels, is usually 20 (6). In most of the literature it is also used for nickel based alloys as Imayev (7). In accordance with the results obtained, linear correlations between the LMP and the stress were observed for the investigated alloys. The H282 alloy showed the highest creep rupture life, followed by IN-740, according to the literature (8). In the lower stress range, IN617B presented higher creep life than Sanicro 25.

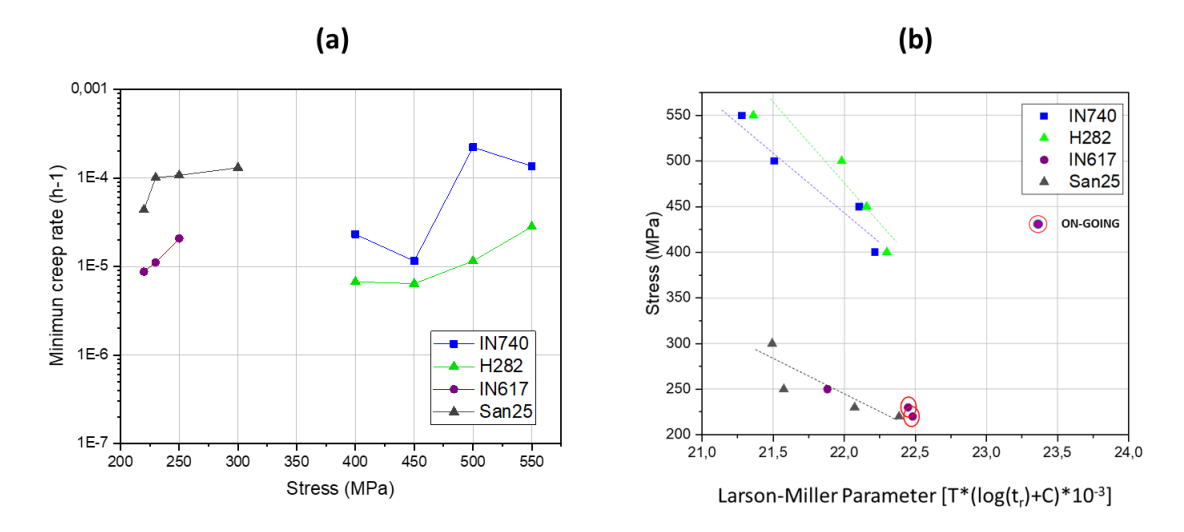


Figure 50. (a) Minimum creep rate of the investigated alloys as a function of applied stress, (b) Larson-Miller plot of the investigated alloys. Tests performed in air at 700 °C.

CIEMAT also tested P92 steel to obtain creep reference values in air and to study the effect of sample size. Shorter times to rupture and high minimum strain rates were observed compared to the literature. The creep properties (Table 14) and curves (Figure 51) are presented below:

P92	ID	tr (h)	Strain at rupture (%)	Minimum strain rate (/h)
<1000h (70MPa)	PL18	165	9.63	1.06E-04
<700h (80MPa)	PL24	82	11.2	2.11E-04
<500h (100MPa)	PL8	13	7.49	1.23E-03
<100h	PL10	5	9.56	3.03E-03

Table 14. Creep properties obtained for P92 alloy.

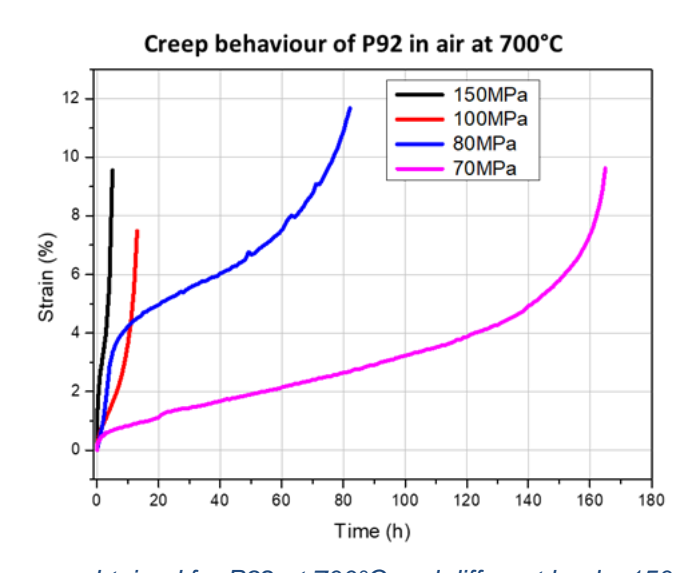


Figure 51. Creep curves obtained for P92 at 700°C and different loads: 150, 100, 80 and 70MPa.

Selected post-mortem samples were used to study the oxide scale formed after creep tests in air. The samples were prepared in the longitudinal direction and analysed by means of Scanning Electron Microscopy (SEM). The composition of the oxide scale and internal oxidation in those cases that were observed, were studied by Energy-dispersive X-ray Spectroscopy (EDS). A few examples have been selected to explain the general behaviour of the different state of the art materials.

Figure 52 shows the SEM images of the fracture area and oxide scales for P92 material tested at 700 °C and 70 MPa as an example. EDS analysis of the same area is also shown. A thin oxide layer has been formed in all the tested condition for P92, thinner as the applied load increases, as expected. The mean value of the thickness of the oxide scales are shown in Table 15.The oxide scale is enriched in Cr, Mn and traces of Mo. In this case, internal oxidation was not observed.

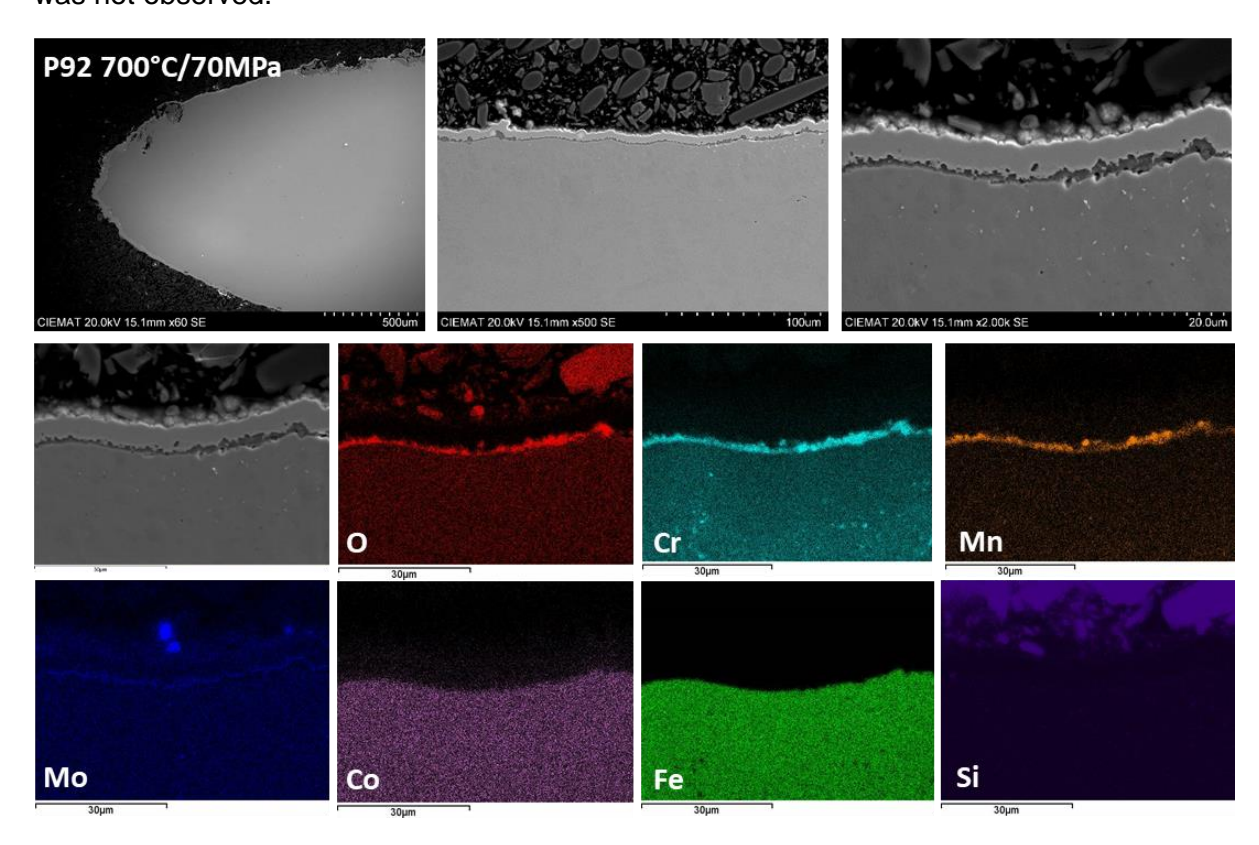


Figure 52: SEM images and EDS maps of P92 tested at 700 °C/70MPa

Test condition

Oxide scale thickness (μm)

700 °C/70MPa

1.2±0.1

700 °C/80MPa

1.0±0.1

700 °C/100MPa

0.48±0.06

700 °C/150MPa

0.62±0.06

Table 15: Thickness of oxide scales for P92 under different test conditions

In the other SOTA materials the evolution of the thickness of the oxide scales is the same, a thinner oxide layer as the load applied increases.

Figure 53 shows and example of the behaviour of Haynes 282 after creep tests in air. The example corresponds to the material tested at 700 °C and 400MPa. Again, a thin oxide scale has been formed, in this case with a thickness of $(0.74\pm0.04)~\mu m$ and composed of Cr and Ti. There is also internal oxidation associated to the presence of O and Al. The values of the oxide scales for the test conditions studied by means of SEM/EDS are shown in Table 16. The values are similar since the applied load change a little.

Just below the oxide layer, there is a depletion of Cr that can be associated to the migration of this element to the oxide scale. Finally, during the test, radial cracks have been formed that emerged from the surface in many regions and, as can been seen in the EDS maps, are also affected by oxidation.

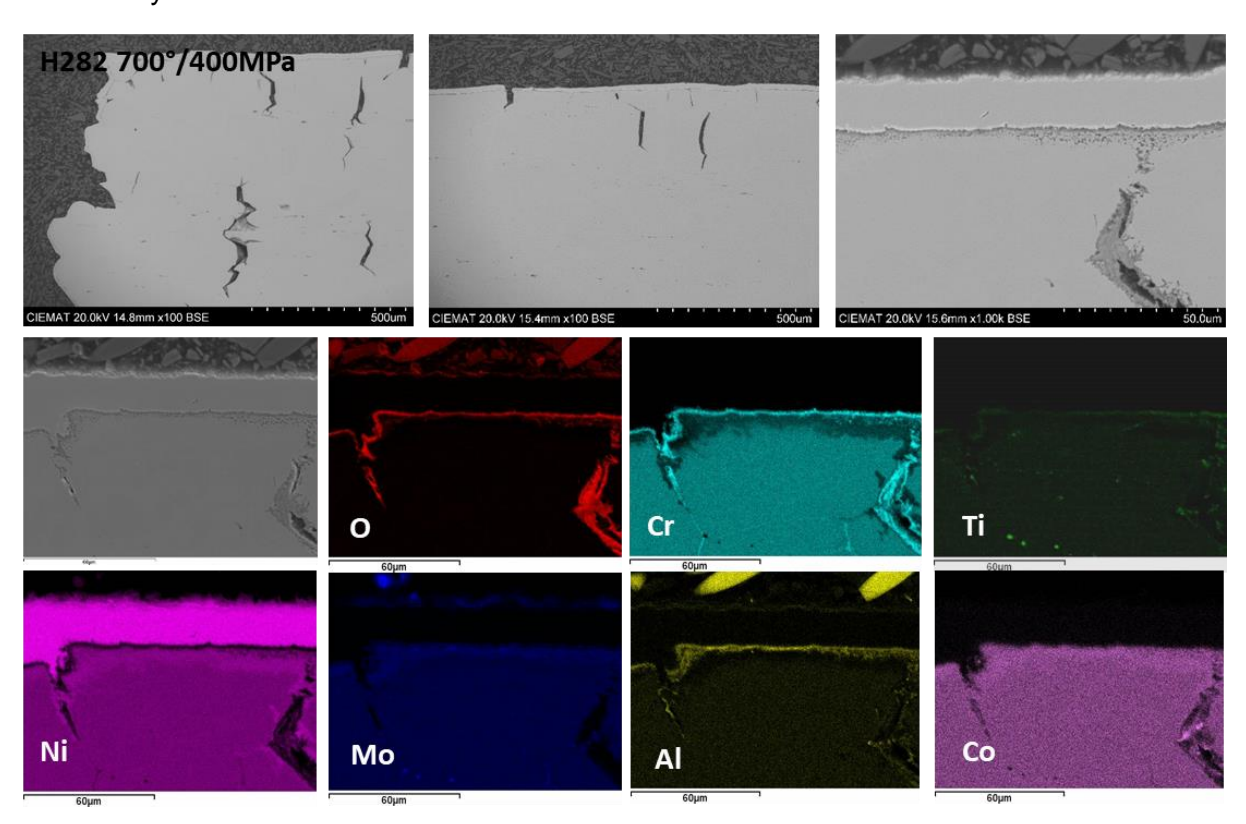


Figure 53: SEM images and EDS maps of Haynes 282 tested at 700 °C/400MPa

Table 16: Thickness of oxide scales for Sanicro25 two different test conditions

Test condition	Oxide scale thickness (µm)
700 °C/400MPa	0.74±0.04
700 °C/450MPa	0.73±0.03

Figure 54 shows the microstructure of Sanicro 25 tested at 700 °C and 230MPa. In this case the mean value of the thickness of the oxide scale corresponds to (0.8 \pm 0.1) μ m. The values of thickness for the other test conditions studied by means of SEM/EDS are shown in Table 17.

As it was expected, the thickness decreases as the applied load increases. The oxide scales are enriched in Cr, Nb and Mn and there is also a depletion of these elements underneath the oxide layer and an enrichment in Ni due to the selective oxidation of Cr to form the oxide scale. This region contains also large Cr rich precipitates with small amounts of W.

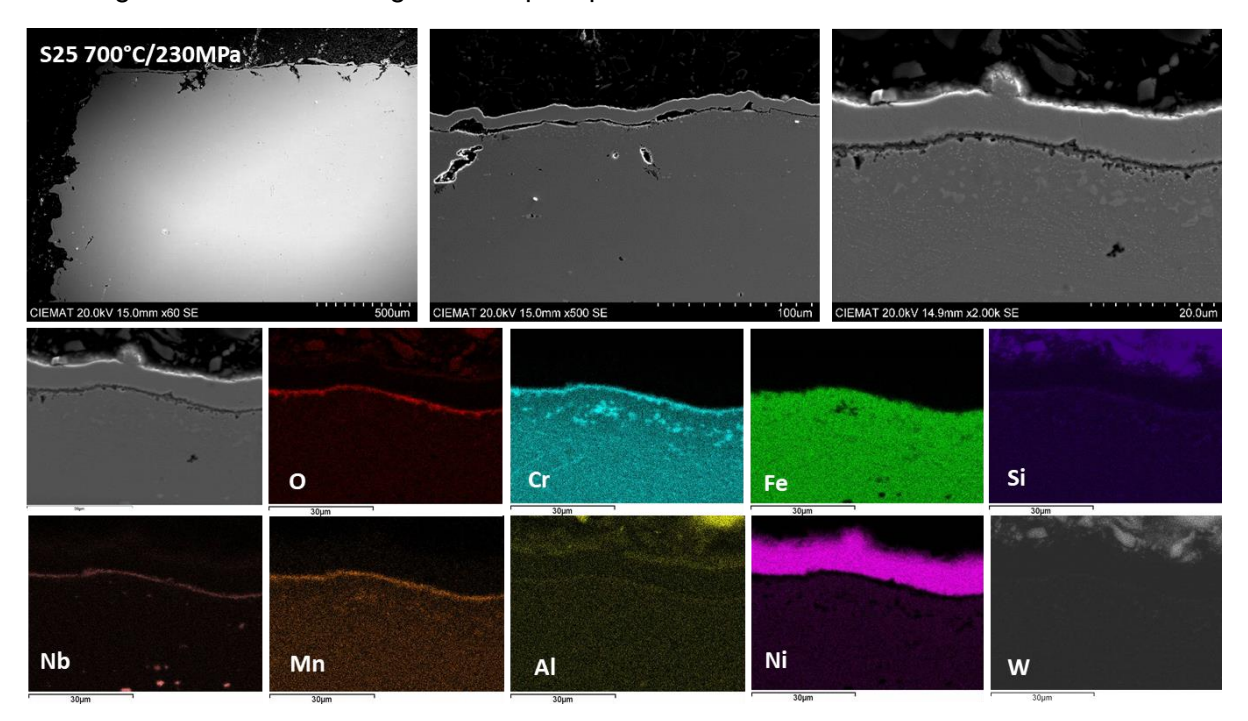


Figure 54: SEM images and EDS maps of Sanicro 25 tested at 700 °C/230MPa

Table 17: Thickness of oxide scales for Sanicro25 under different test conditions

Test condition	Oxide scale thickness (µm)
700 °C/220MPa	1.4±0.2
700 °C/230MPa	0.8±0.1
700 °C/300MPa	0.45±0.04

Figure 55 shows the microstructure of Inconel 740 tested at 700 °C and 400 MPa. In this case the thickness of the oxide layer corresponds to (1.4±0.7) µm and is formed by Cr, Mn and Nb. The thickness of the conditions studied by means of SEM/EDS for Inconel 740 are shown in Table 18. An internal oxidation is detected underneath the oxide scale by the presence of O and Al. There is a depletion of Cr just below the oxide scale associated with the migration of this element to the oxide layer. The radial cracks that emerged from the surface are also affected by oxidation.

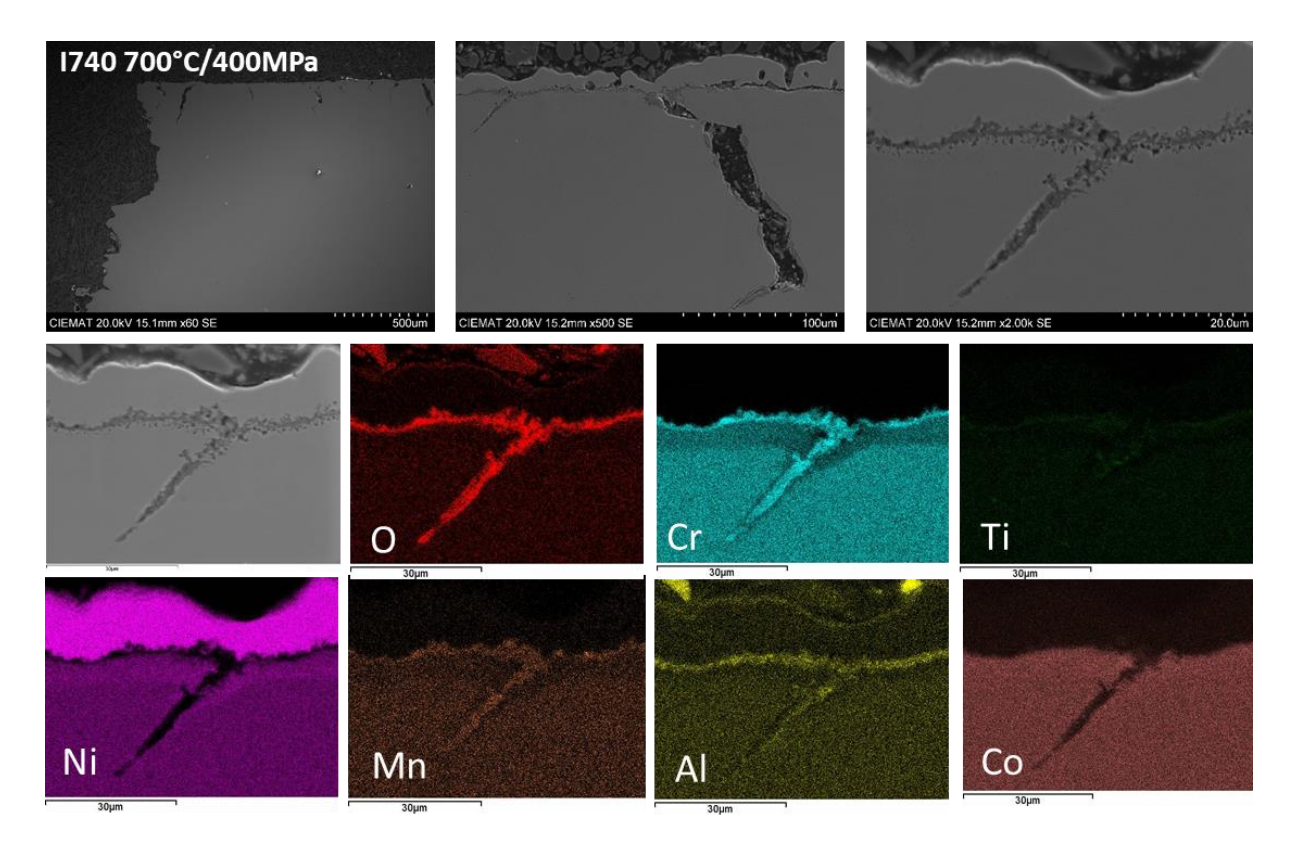


Figure 55: SEM images and EDS maps of Inconel 740 tested at 700 °C/400MPa

Table 18: Thickness of oxide scales for Inconel 740 under different test conditions

Test condition	Oxide scale thickness (µm)
700 °C/400MPa	1.4±0.7
700 °C/500MPa	0.59±0.03

Finally, Figure 56 shows the microstructure of Inconel 617 after creep test at 700 °C and 250 °C. The thickness of the oxide scale corresponds to $(0.90\pm0.06)~\mu m$ and it is mainly enriched in Cr and Mn with Ti in some regions of the oxide layer. An internal oxidation it was also detected below the oxide layer by the presence of O and Al and, as in the case of the other Nibase materials, there is a depleted region in Cr, just below the oxide scale, associated with the migration of this element to the oxide layer.

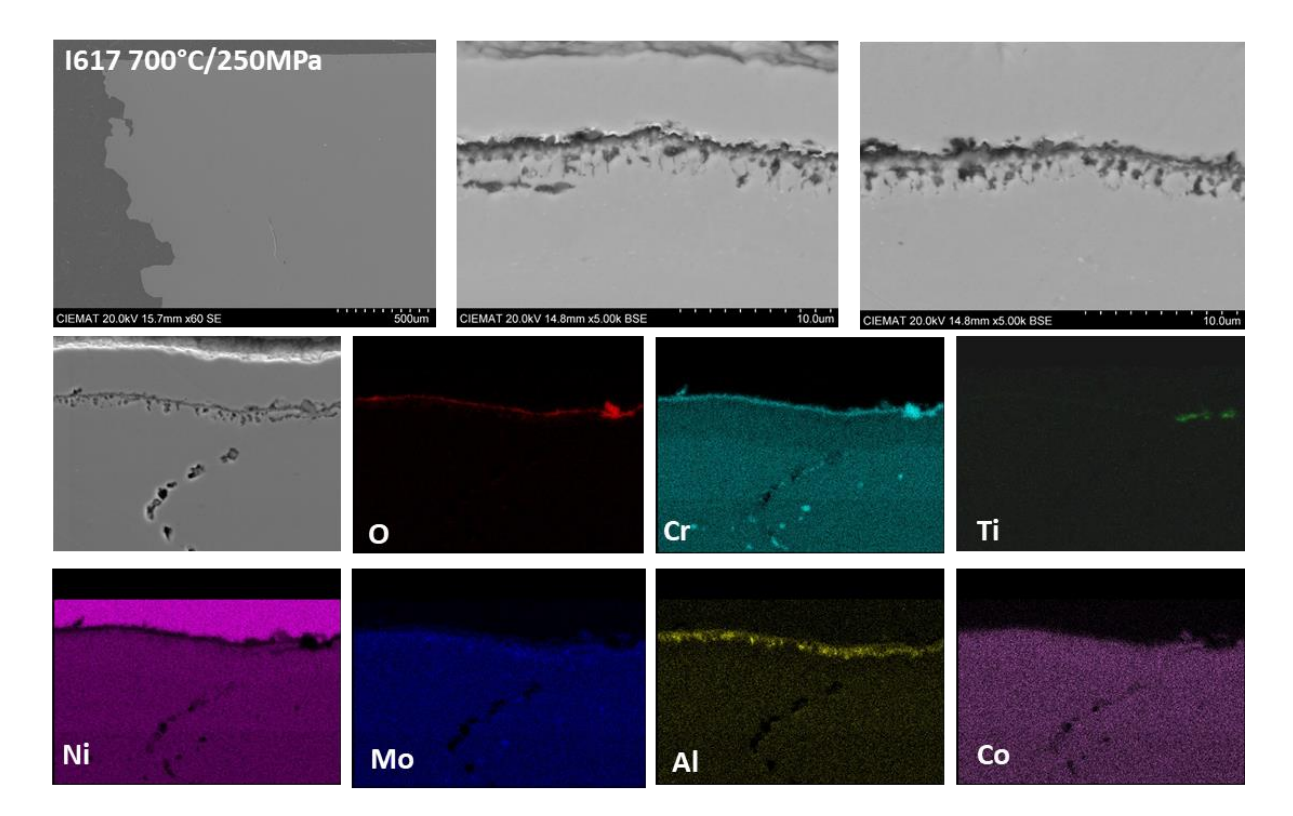
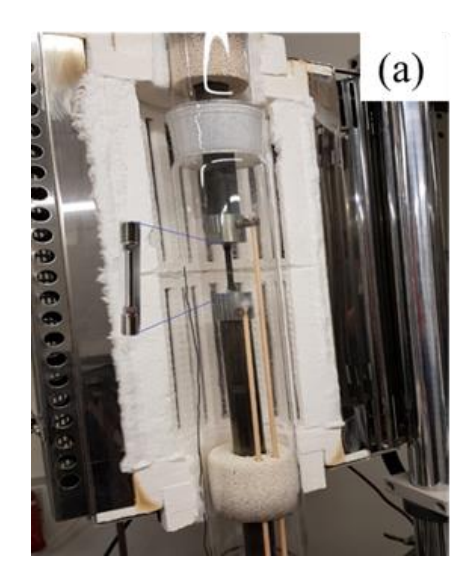


Figure 56: SEM images and EDS maps of Inconel 617 tested at 700 °C/250MPa

5.2 CREEP PROPERTIES AT DFI

5.2.1 Experimental procedure

The creep tests in flowing CO₂ have been conducted at DFI at 700°C under flowing (6 L/h) industrial grade (IG, 99.5%) CO₂ using the in-house constructed test rig (Figure 57.a). Creep test samples with the gauge length of 37 mm were machined from received cylinders to the testing geometry by the DFI mechanical shop (see Figure 57.b). The samples were heated up to the testing temperature of 700°C under flowing Ar to avoid the oxidation during heating. After reaching the exposure temperature, the gas was switched to IG-CO₂ and the load was applied through a 1/10 lever. Linear Variable Differential Transformer (LVDT) was used to record the displacement during the creep test with a data acquisition frequency of 1/60 s⁻¹ and afterwards to calculate the strain. In most cases, the tests were concluded with the rupture of the specimens. Nevertheless, some tests were finished within the tertiary creep regime. After the tests, rupture times were compared by plotting the creep curves for each sample. Furthermore, creep curves were used to determine the minimum creep rate together with double logarithmic plots to determine the influence of stress on the minimum creep rate. Lastly, Larson-Miller plots were used to characterize the creep rupture behavior of investigated alloys.



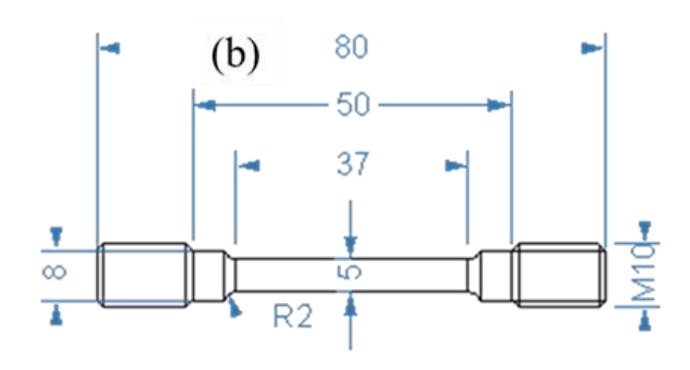


Figure 57. (a) Test rig constructed by DFI for creep testing in flowing CO₂, (b) dimensions of creep test samples tested at DFI.

After the tests, macroscopic images of the crept samples were recorded, cross and longitudinal sections were prepared using conventional metallographic methods including grinding with SiC paper and polishing down to 1 μ m using diamond suspensions. Cross sections were analyzed using light-optical microscopy (LOM) and elemental probe micro-analysis (EPMA) to characterize the oxide scales and alloy sub-surfaces.

5.2.2 Test conditions

DFI and CIEMAT selected the creep test loads in close cooperation with the project consortium and taking into consideration the creep rupture data of the selected alloys in air. The selection of the same or in some cases comparable loads enables a direct comparison of the creep strength in air and in CO₂. In order to investigate the reproducibility of the data, additional tests with intermediate loads were added to the test matrix. After the conduction of preliminary tests, the loads were adapted and, in most cases, increased to reach the targeted testing durations. For most cases, an additional sample was exposed to flowing CO₂ in the creep test rig, however without any external mechanical load. This investigation was performed to determine the influence of external load on the scale thickness and on the Cr-depletion in the alloy subsurface. At the time of writing, creep testing in CO₂ campaign have been completed at DFI, for which an overview is provided in Table 19.

Table 19. Applied stresses for the creep tests in CO₂ at DFI.

Alloy	Sanicro 25	IN617B	Haynes 282	IN740
Stress (MPa)	300, 270, 240,	350, 330, 315,	550, 525, 500,	550, 525, 500,
	220, 200	300, 280, 250	450, 400	450, 400

5.2.3 Results and discussion

Figure 58 shows the creep curves of investigated alloys in CO_2 . Expectedly, the austenitic steel, Sanicro 25 exhibited high creep deformation, whereas the solid-solution strengthened Ni-based alloy IN-617B demonstrated a notably prolonged creep rupture lifetime under similar loads (please note the varying x-axes). In the case of γ -strengthened nickel-based alloys IN-740 and Haynes-282, despite identical tested loads, distinct variations of creep strain and time to rupture were observed. Specifically, IN-740 displayed lower levels of both creep strain and creep rupture lifetime in contrast to Haynes-282.

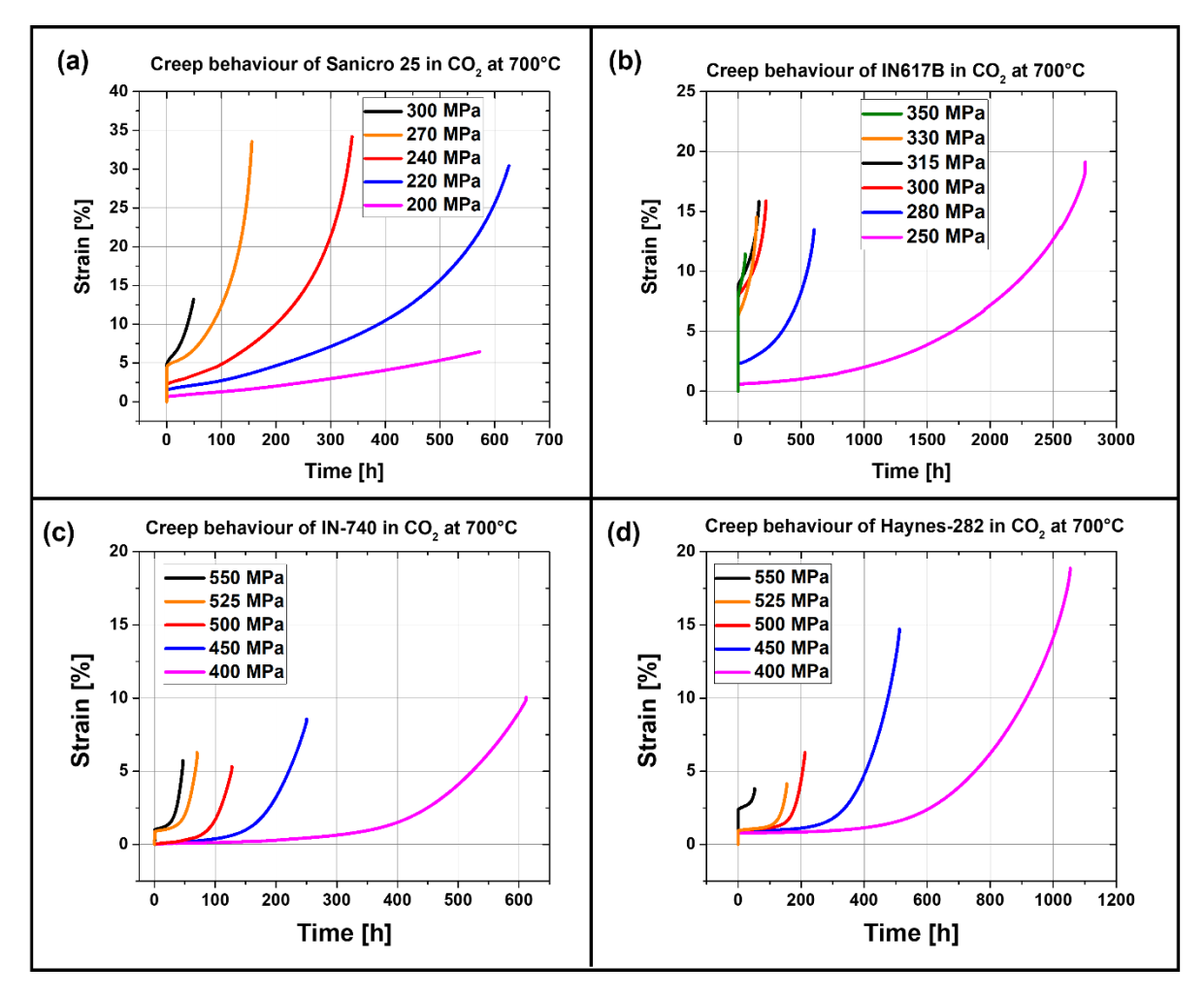


Figure 58. Creep curves of (a) Sanicro 25, (b) IN-617B, (c) IN-740 and (d) Haynes-282 in flowing IG-CO₂ at 700°C. Please note the varying x- and y-axes in the respective diagrams.

The minimum creep rates of these alloys under different loads were plotted in Figure 59a against the applied stress. Sanicro 25 exhibited the highest minimum creep rates among the tested alloys, followed by IN-617B. While the minimum creep rate of Sanicro 25 linearly increased with applied stress, IN-617B showed a higher dependency of minimum creep rate on the stress, namely the slope of the curve, or in other words, the stress exponent between 250-300 MPa. However, above 300 MPa, the stress exponent for IN-617B unexpectedly decreased. It should be noted that, only one sample per load was tested. For a better clarification of this unexpected behavior, further tests in the future should be performed. Both γ '-strengthened nickel-based alloys displayed lower minimum creep rates, with IN-740

showing slightly lower rates compared to Haynes-282. Despite displaying a slightly higher minimum creep rate, Haynes-282 can withstand higher creep strains prior to rupture compared to IN-740. Moreover, the stress exponent seems to increase significantly between 500 and 550 MPa for both alloys. Figure 59.b depicts the creep rupture behavior of the investigated alloys using the industrially well-established Larson-Miller Plots (LMP plot), for which the Larson-Miller parameter (LMP) includes the information on the rupture time and temperature and is usually plotted against the applied stress. LMP is calculated by the following equation:

$$LMP = T \cdot (\log(t_f) + C)$$

wherein, T denotes the testing temperature in K, t_f is the rupture time and C is a material constant and for metallic materials (and in this case) is usually 20.

Given that the LMP plot incorporates temperature, it provides insight into the "thermal load" experienced by the tested alloys, enabling relative lifetime predictions. Despite conducting all the creep tests at 700°C in this task, LMP plots will enable a direct comparison of the experimental data with the literature in the future. A linear correlation between the LMP and the stress was observed for all investigated alloys. Briefly, Haynes-282 showed the highest creep rupture lifetime followed closely by IN-740. Within the lower stress region, IN-617B showed a significantly higher creep rupture lifetime compared to Sanicro 25.

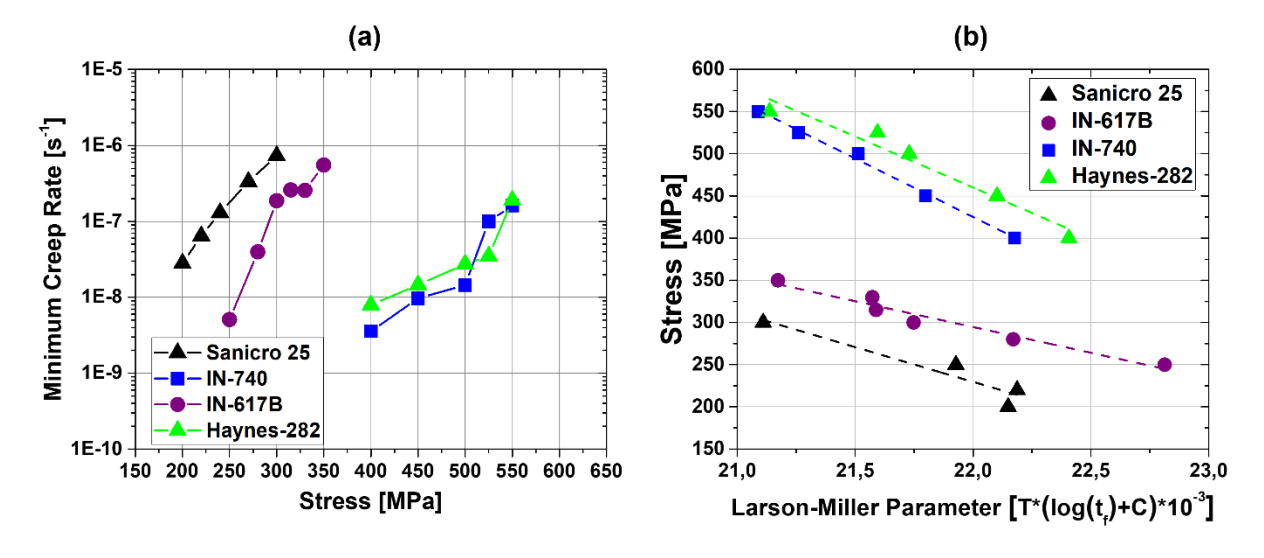


Figure 59. (a) Minimum creep rate of the investigated alloys as a function of applied stress, (b) Larson-Miller plot of the investigated alloys.

Cross and longitudinal sections of samples were investigated to assess the influence of the CO_2 atmosphere, load, and high temperature exposure on the microstructural degradation and the failure mechanism. Figure 60 shows cross sectional images belonging to representative spots for each investigated alloy (with and without external load). Solid solution strengthened alloys exhibited a common failure pattern characterized by a depletion of stable oxide formers near the surface of the substrate and the consequential formation of carbide denuded zones, serving as crack initiation points (not shown here). In the case of γ -strengthened alloys, the exposure resulted in the formation of γ -depleted sub-surface zones due to the oxidation of γ -forming elements. Nevertheless, a significant influence of the load on the microstructural

degradation of the investigated alloys was not observed. The post-exposure characterization of the samples at DFI will be completed in the upcoming months.

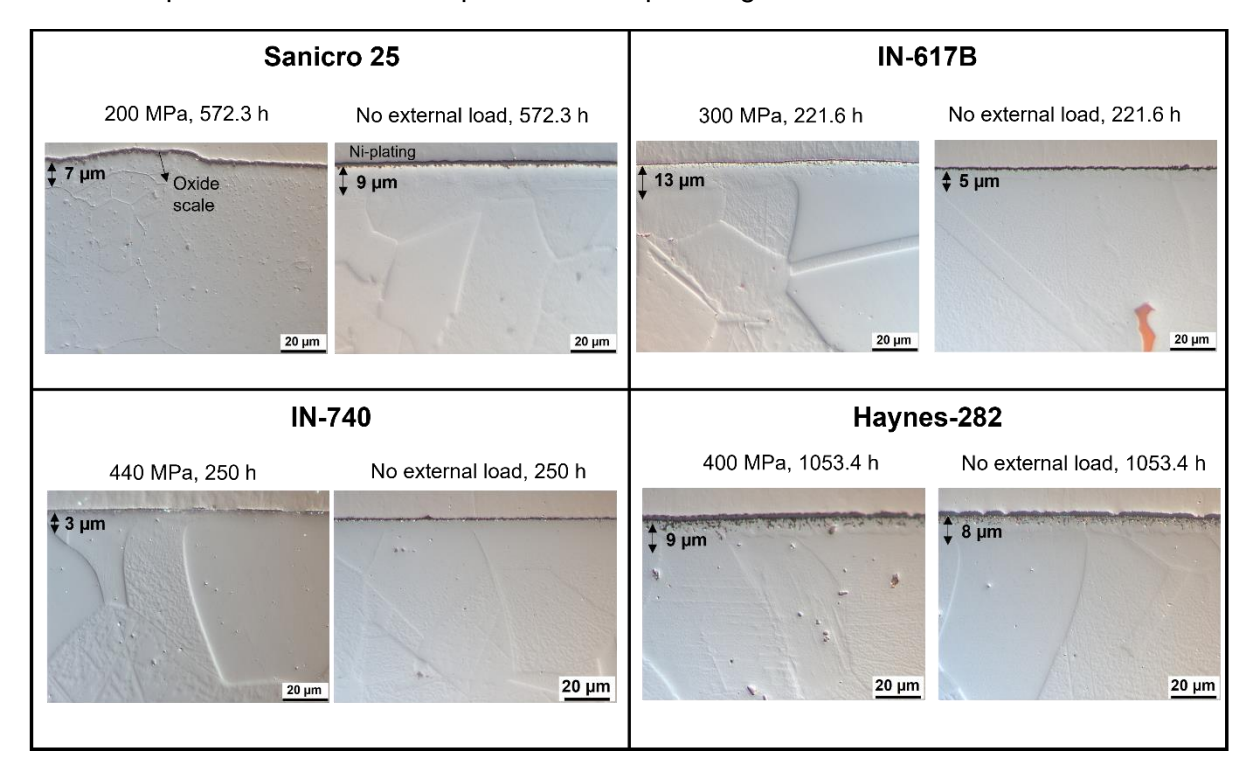


Figure 60. Cross sectional LOM images of the investigated alloys after creep tests. Please note for each alloy, the images on the left-hand side belong to creep test samples, whereas the images on the right-hand side belong to the samples without external load. The depletion zones are indicated by an arrow in the respective images.

5.3 SMALL PUNCH CREEP

Small punch (SP) is a methodology that uses small amounts of material (disk of 3 or 8 millimeters of diameter and 0.25 or 0.5 millimeters of thickness) to estimate mechanical properties of metallic materials. For the characterization and development of new materials, CIEMAT carried out conventional SP tests for SOTA materials in WP3 in order to compare with the new development materials that will be fabricated in small amount. In addition, to complete the creep properties of the SOTA materials and have data to compare with the new materials in future work, CIEMAT has carried out small creep (SPC) tests with the remaining material.

5.3.1 Experimental procedure

The tests have been carried out on a small punch creep testing machine designed and developed by CIEMAT and SERVOSIS. The disc specimen is compressed by a hemispherical head punch under a constant load and temperature. In the experiment, the specimen is mounted in a specimen holder and placed in the high temperature furnace. The hemispherical head punch is used to transfer the load from the weight. The deflection of the center of the SPC specimen surface was recorded by an extensometer mounted in the lower die, and in direct contact with the specimen. The displacement is also recorded by another extensometer mounted in the loading system.

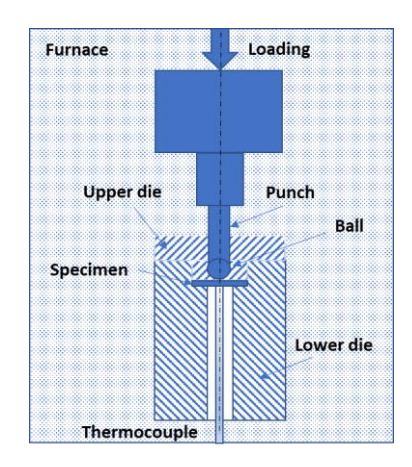


Figure 61. Schematic diagram of small punch creep system.

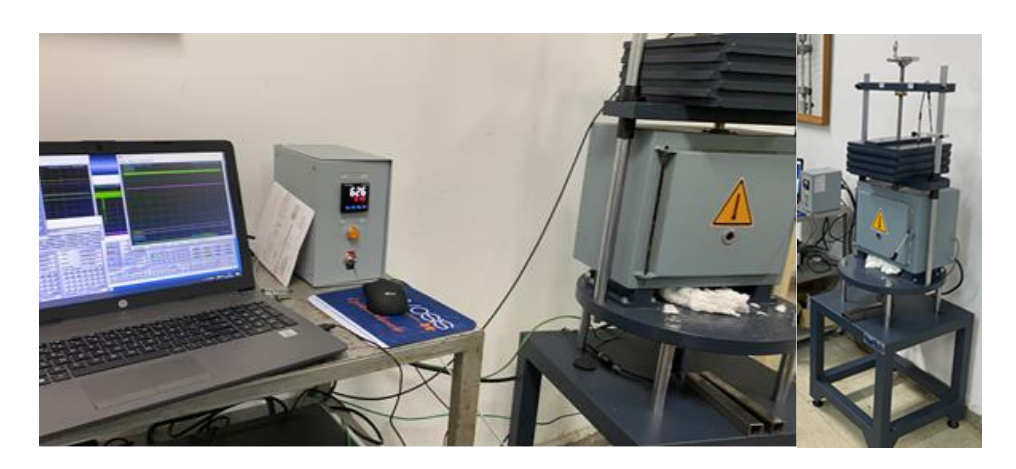


Figure 62. CIEMAT small punch creep machine.

CIEMAT carried out SPC test on the remaining SOTA material after mechanization and completion of all test campaigns in WP3 and WP4. The materials investigated were: IN740, Sanicro25 and IN617. The specimens were mechanized and prepared at CIEMAT following the standard EN 10371:2021 (9) in longitudinal (L) orientation. The test pieces are circular discs with a diameter of D_s =8mm and an initial thickness of h_0 =0.5 mm.

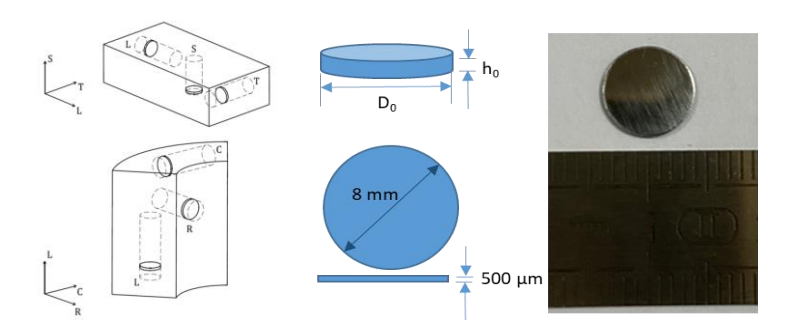


Figure 63. Orientation of SP specimens. SP/SPC specimen.

SPT discs were cut out from a previously obtained cylinder using EDM wire cutting. After EDM cutting the thickness of the disc is $h_{0\text{EDM}}$ =0.65. The targeted thickness of 0.5 millimetres was achieve by grinding and polished steps and measurements between steps. Both sides of the

disc were manually grinded with abrasive papers with increased fineness to reach the final tolerance (1%) and surface roughness (Ra< 0.25) requested by the small punch testing standard (EN 10371. Before SPC testing, the thickness of the test disc specimen is measured at five positions.



Figure 64. Finished procedure to obtain discs for SPC tests.

5.3.2 Results

The load selection for the small punch creep is based on the results of the conventional small punch tests (Constant displacement rate small punch tests). Small punch tests of all the SOTA materials were performed by CIEMAT within COMPASSCO2 WP3 at room temperature, 300°C and 500°C. Although these tests were not performed at 700°C due to CIEMAT machine upper temperature limitation, the 500°C tests gives an approximation for the selection of creep load in small punch creep. according to CIEMAT previous experience, the measured permanent displacement of the SP sample during small punch creep tests is close to the value of the disc displacement at the force Fi defined by Alstadt et al (10).

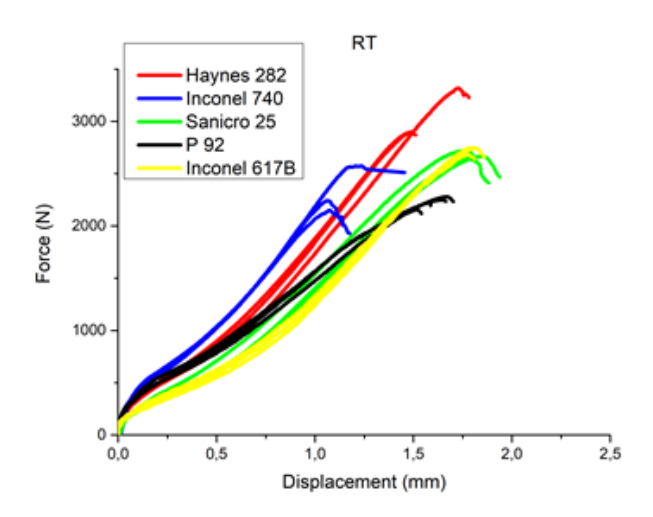


Figure 65. Small punch curves for SOTA materials at room temperature (RT).

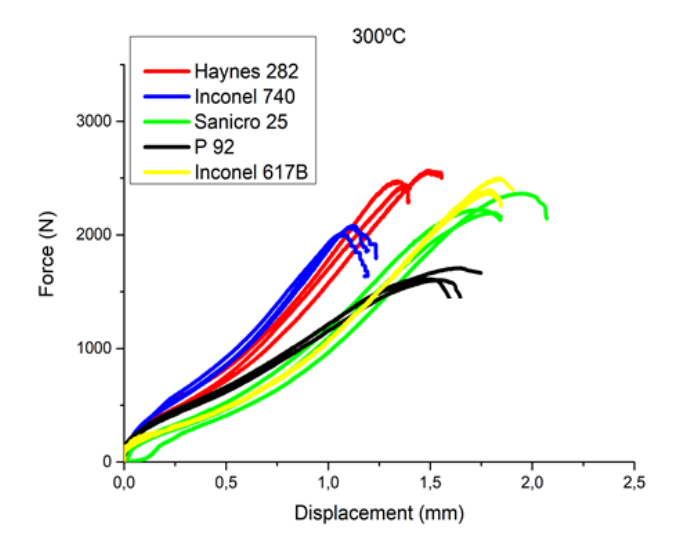


Figure 66. Small punch curves for SOTA materials at 300 °C.

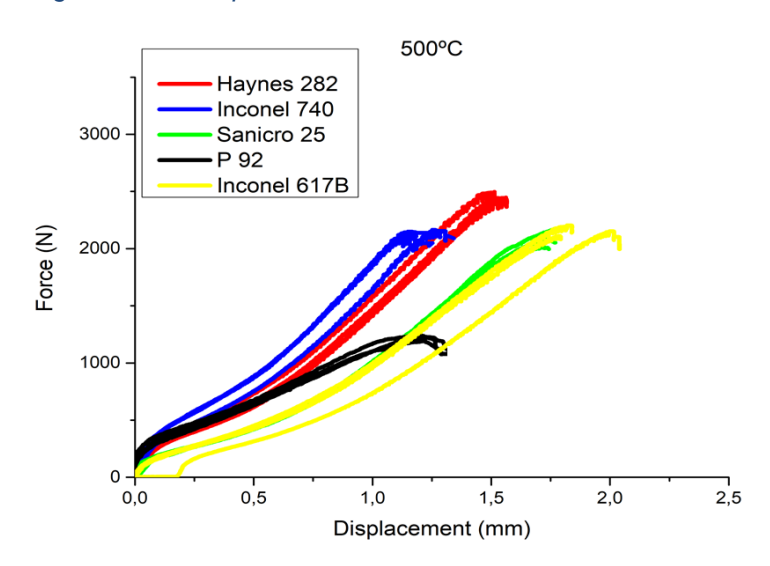


Figure 67. Small punch curves for SOTA materials at 500 ℃.

The results obtained are comparable to those obtained with standard tensile tests. Ni Superalloys show superior mechanical properties over Stainless steel and martensitic steels according with the reference data studied and the literature review performed in WP1 and WP3. IN740 has the highest yield strength. H282 and IN617 shows the greatest ductility at all temperatures.

The three following tables show the summary of the main small punch parameters obtained for the studied materials to be tested in small punch creep, and which have influenced the design of the test matrix to obtain representative values, within the duration of the project. The analyses of Small Punch tests in this study were performed by means of a Microsoft Excel macro-enabled spreadsheet from CIEMAT. Test results shown in the next tables where:

- T: test temperature, (°C)
- h0: Initial thickness of the test piece (at the beginning of the test), (mm)
- · ue: Deflection at Fe, (mm)

- Fe (ASTM): Force characterizing the transition from linearity to the stage associated with the spread of the yield zone (N)
- Fe (EN 10371): Elastic-plastic transition force in a small punch test, (N)
- um: Deflection at Fm, (mm)
- Fi (EN 10371):Force at deflection ui or displacement vi, (N)
- Fm: Maximum of F during the test, (N)
- ESP (ASTM 3205): Fracture energy calculated under the area under the F-u curve up to uf.
- Em (ASTM 3205) or ESP (EN 10371): total energy (elastic + plastic) calculated under the area under the F-u curve up to um, (J)

According with Annex C and Annex D of EN 10371:2022 standard, small punch test can be used to estimate ultimate tensile stress (Rm) and yield strength (Rp0,2).

IN740 Fe ISO (N) Fi(N) Fe/h0² (MPa) Fm/um*h0 (MPa) T (°C) u (mm) Fm (N) E (J) IN740 L1 1.07 IN740 L2 1.21 IN740 L3 1.06 IN740 L4 1.08 IN740 L5 1.12 IN740 L6 1.1 1.25 IN740 L7 IN740 L8 1.15 IN740 L10 1.14

Table 20. SP results obtained for IN740 alloy.

Table 21.	CD	rooulto	abtained	for C	Caniara 25	otool
Table 21.	SP	resuits	oblairied	101 3	SariiCr025	Steer.

San25	T (°C)	Fe ISO (N)	u (mm)	Fm (N)	Fi (N)	E (J)	Fe/h0^2 (MPa)	Fm/um*h0 (MPa)
S L1	22	165	1.77	2646	799	2288	661	2994
S L2	22	188	1.75	2723	914	2429	753	3107
S L3	22	173	1.85	2668	787	2456	691	2886
S L4	300	154	1.82	2196	605	1932	618	2418
S L6	300	159	1.73	2223	677	1888	635	2567
S L7	300	138	1.78	2152	596	1833	550	2418
S T7	500	117	1.78	2176	542	1746	467	2450
S T8	500	137	1.73	2081	558	1660	549	2402
S T9	500	153	1.72	2017	559	1609	613	2348

IN 617 T (°C) Fe ISO (N) Fm (N) Fi(N) E (J) Fe/h0² (MPa) Fm/um*h0 (MPa) u (mm) IN617 L1 24 2744 702 2289 3031 150 1.82 605 IN617 L2 24 789 2293 150 1.78 2741 605 3093 IN617 L3 24 1.78 752 2219 160 2683 640 3018 603 | 1905 IN617 L4 300 160 1.79 2364 648 2665 IN617 L5 2497 607 2014 300 150 1.82 598 2735 IN617 L6 142 1.78 2395 618 1916 300 566 2683 543 | 1704 IN617 L7 500 1.79 2112 540 2360 135 578 1831 IN617 L8 500 142 1.82 2204 568 2423

Table 22. SP results obtained for IN617 alloy.

As it is mentioned previously, the SPC load should be close to the value of Fi. To have a good comparison between materials, the SPC loads were selected according to the Inconel 740 SPT results, as this material is expected to have longer rupture times. Based on the results obtained and in order to achieve time-to-rupture within the project timeframe, the following test matrix was designed:

2152

409

1808

598

2130

Table 23. Applied loads for the small punch creep tests in air and at 700°C at CIEMAT.

Alloy	Sanicro 25	IN617B	IN740
Load (kg)	60,50,40	60,50,40	60,50,40

Novel developed materials

500

150

2.02

SP tests were carried out for the novel materials developed by the UoB at RT, 300 and 500 °C. UoB made a short stay at CIEMAT in order to perform part of the small punch tests.

Test pieces are discs with 8 millimetres of diameter and 0.500 millimetres of thickness (D_S =8 mm, h_0 =0,5 mm) and smaller test pieces ((D_S =3 mm, h_0 =0,25 mm)), according with the EN10371:2021 standard. The materials studied were:

Cr

IN617 L9

- Cr rolled
- Cr5Ni5Al5Fe
- Cr5Ni5Al10Fe
- Cr5Ni10Al10Fe

A microstructural study and fractography of each specimen prior and after to testing were carried out. The fractography obtained shows an example of the brittle fracture at the three temperatures tested. An example is shown below:

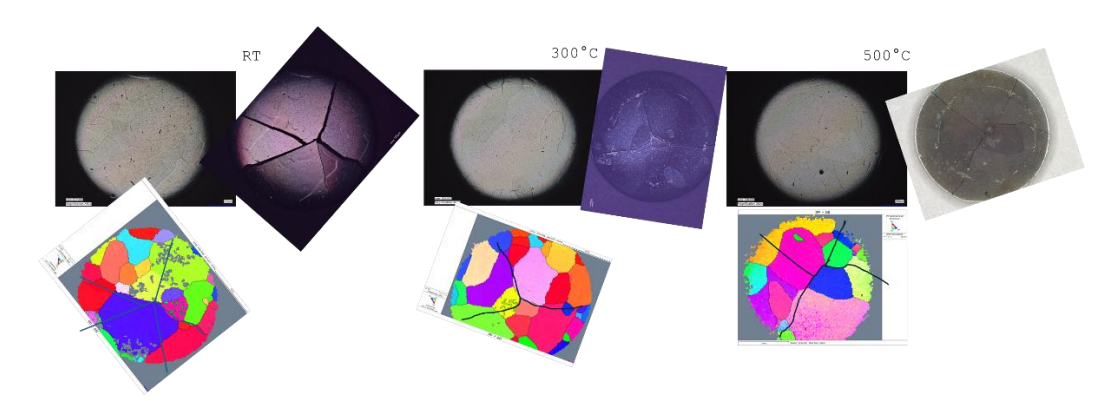


Figure 68. Microstructural study and fractography of the samples before and after testing for the Cr5Ni5Al 10Fe by UoB.

The brittle behaviour of the studied samples of the novel materials does not allow the estimation of the SP parameters. Therefore, the estimation of Fe and Fm becomes very difficult. For example, the EN 10371 provides two methods for estimating the Rm:

- Maximal measured force, Fm.
- Or the force at the onset of plastic instability, Fi.

Using the Fm for estimating Rm could be problematic as damage may begin to occur at load levels close to Fm. These results does not seem suitable for the characterization of these brittle materials, accelerating the specimen breakage and certainly not allowing to reach the maximum strength of the material if it were studied in a conventional tensile test. In the light of the results obtained, a correct estimation of Fm and Fi is not possible for the new materials.

In the absence of a valid Fm/Fi, the study of the energy under the SP curve (E_{SP}) may also result in underestimated values. In this case, the fractography provides information on the brittleness of materials in this case (Figure 68).

A possible future work would be the application of simulation through damage models in the small punch results. Studies are already underway with the application of small punch damage models to model crack initiation and evolution, such as the Gurson-Tvergaard-Needleman damage model.

The curves obtained for the tests performed on 8 mm specimens are shown below.

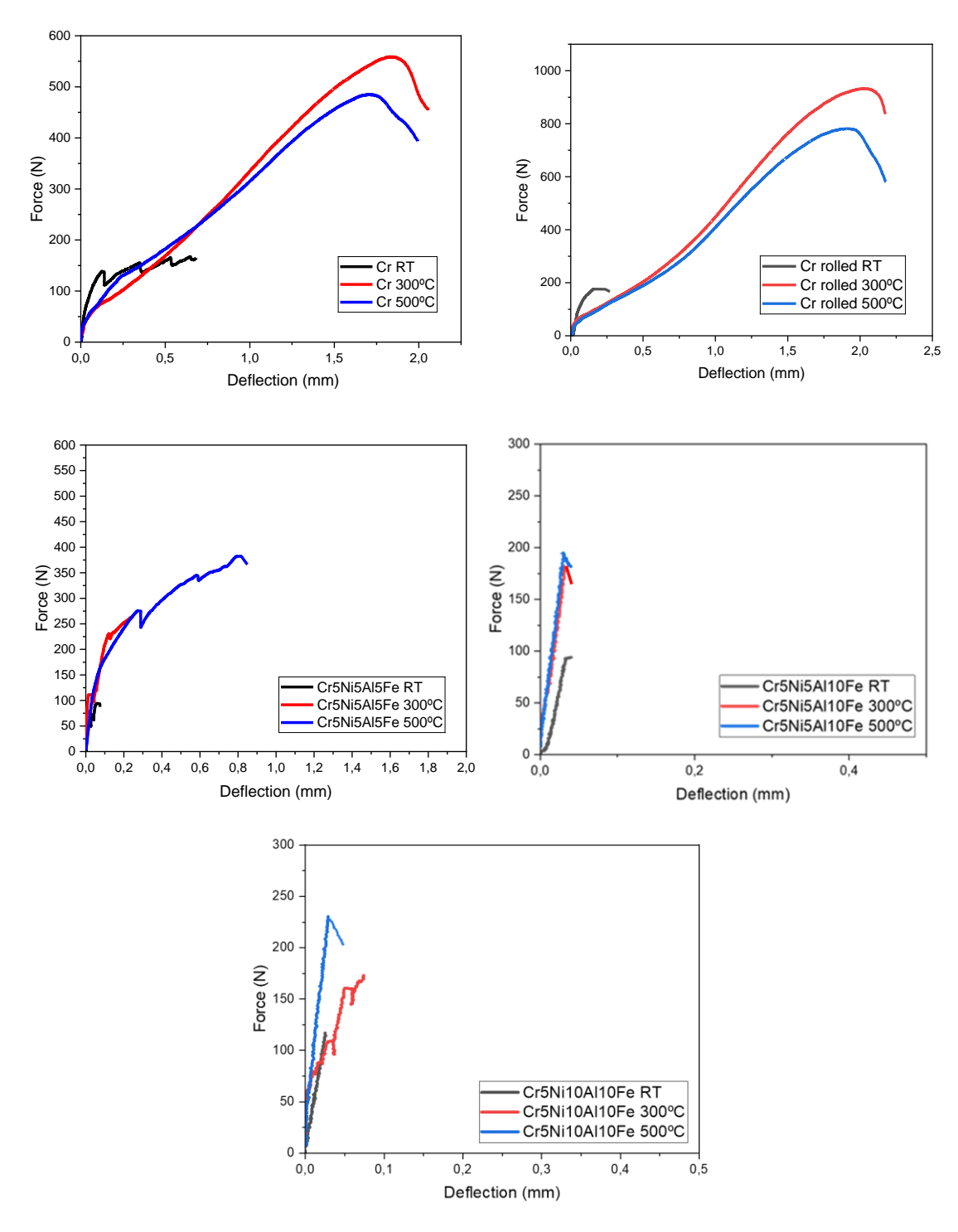


Figure 69. Small punch curves obtained for UoB materials

Novels alloys show lower small punch energy (ductility) than SOTA materials. The brittle behaviour of the studied samples of the novel materials does not allow the estimation of SP parameters.

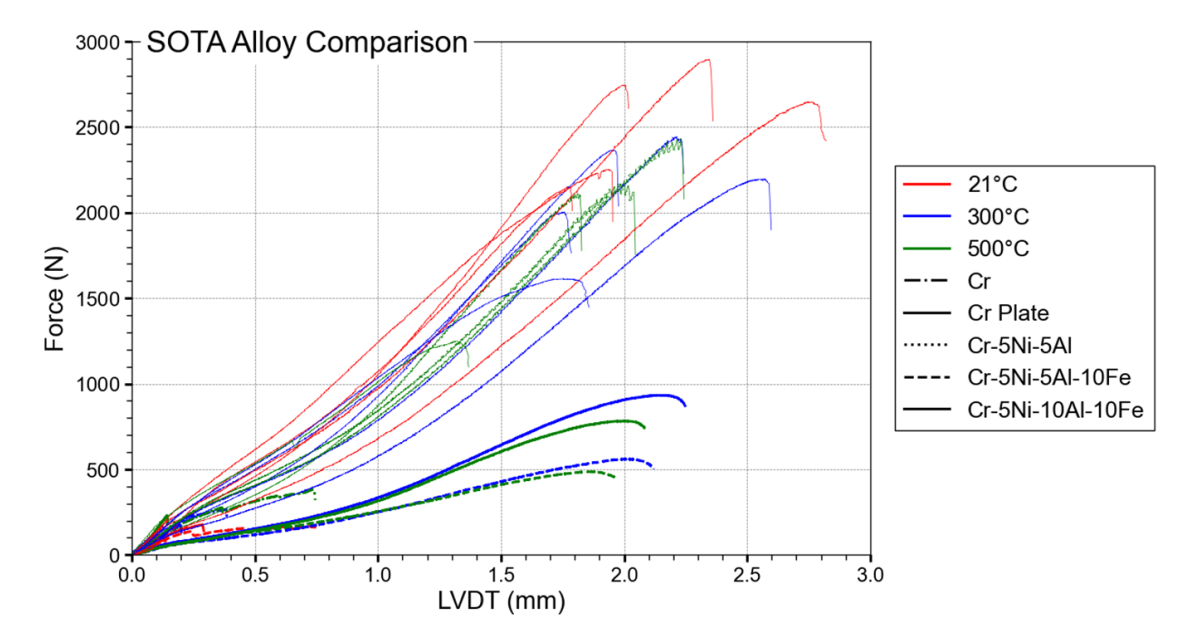


Figure 70. Small punch curves: SOTA and novel alloys.

In order to complete the mechanical characterization, small punch creep tests were performed only for the chromium material (Figure 71). In the following graph, only these small creep curves of Cr are shown. Due to the short times recorded for the chromium material, new materials were not tested because the small punch creep data obtained could not be representative.

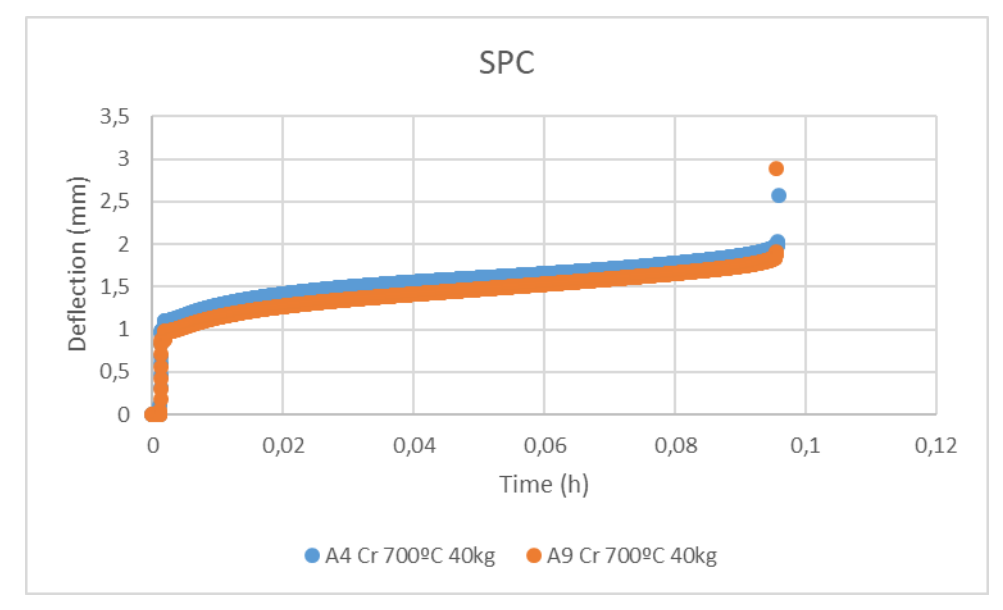


Figure 71. Deflection vs. Time curves obtained for Cr. Test conditions: 700°C and 40kg.

5.3.3 Discussion

The next Figures present the variation of central deflection (mm) as time to rupture (h) at 700°C for levels of load between 60 and 40 kg. The creep curves obtained from SPC test are similar to the conventional one with the initial deflection, primary, secondary and tertiary regions. The effects of applied load and temperature on the creep response in SPC are similar to conventional uniaxial creep tests that is higher load at the same temperature gives shorter

rupture times. In accordance to uniaxial creep tests and the literature, SPC tests show that IN740 has with the longest time to ruptures and Sanicro25 steel with the shortest creep life.

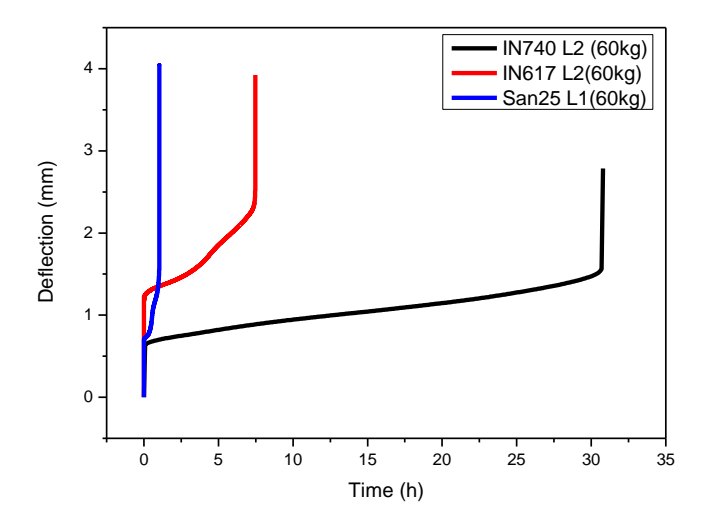


Figure 72. Small punch creep curves obtained at 700°C and 60 kg for IN740, IN617 and Sanicro25.

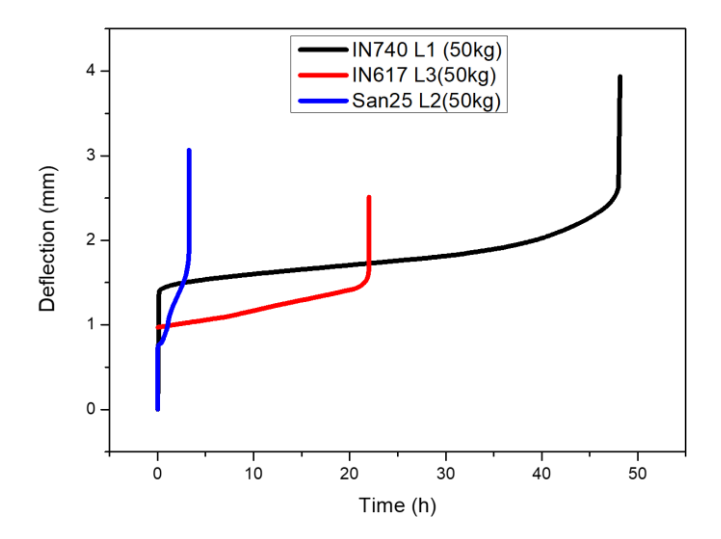


Figure 73. Small punch creep curves obtained at 700°C and 50 kg for IN740, IN617 and Sanicro25.

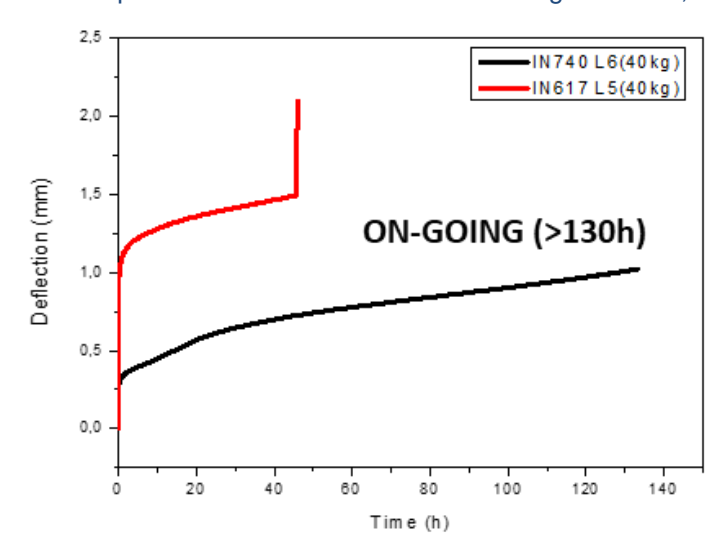


Figure 74. Small punch creep curves obtained at 700°C and 40 kg for IN740 and IN617.

5.4 EVALUATION OF CREEP PROPERTIES

5.4.1 Study of the effect of the environment: Air vs CO2

Figure 75 shows the comparison of the minimum creep rate in air and in CO₂. Values obtained in air tested by CIEMAT are indicated as hollow symbols. Please note the two different geometries were tested in air by CIEMAT. The hollow symbols in this case belong to M5 (miniature samples), whereas the semi-filled triangles correspond to larger samples (M8 samples). The borderline criterion, indicating the highest acceptable creep rate at 10-6s-1, is illustrated by the dashed red line.

As different geometries were used for the high creep resistant alloy Inconel 740 and Haynes 282 in air and in sCO2, it is difficult to analyse the effect of the environment on creep strain rate. Based on the results for the IN617 it can be inferred that the minimum creep rate is not adversely affected by the CO2, as the results from both institutes show a good agreement. For the γ '-strengthened alloys, the high extent of scattering makes a direct comparison difficult. The analytical characterization of the crept samples and the determination of the γ '-depleted or microstructurally altered zones will clarify the influence of the atmosphere.

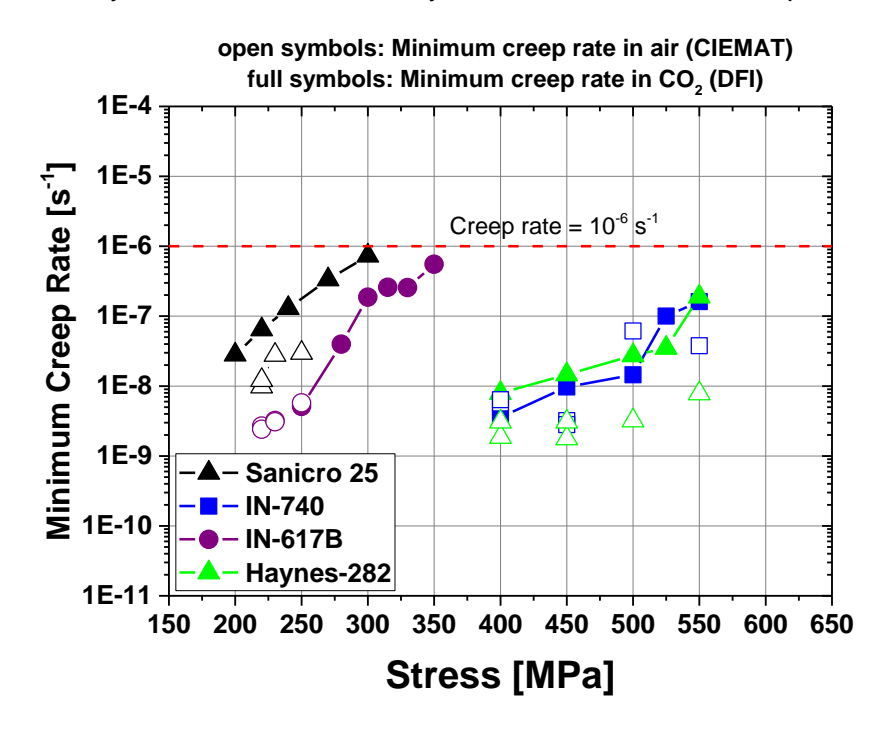


Figure 75. Comparison of the creep data in air and in CO₂. Values obtained in air tested by CIEMAT are indicated as hollow symbols. Please note that Sanicro 25 in air were tested with two sample geometries: M5 (miniature) with hollow symbols and M8 (standard) with semi-filled triangles. The borderline criterion (the highest acceptable creep rate at 10-6s-1) is illustrated by the dashed red line.

Figure 76 shows the Larson-Miller plots for the investigated alloys in both test atmospheres. Despite the deviations in minimum creep rate in varying atmospheres, which was observed especially for the γ '-strengthened alloys, the rupture duration data in air and in CO_2 display a good agreement, and thus no size effect is observed. For both atmospheres, a linear correlation between the applied stress and the rupture duration can be found and the slopes for the investigated alloys do not deviate strongly from each other in varying atmospheres.

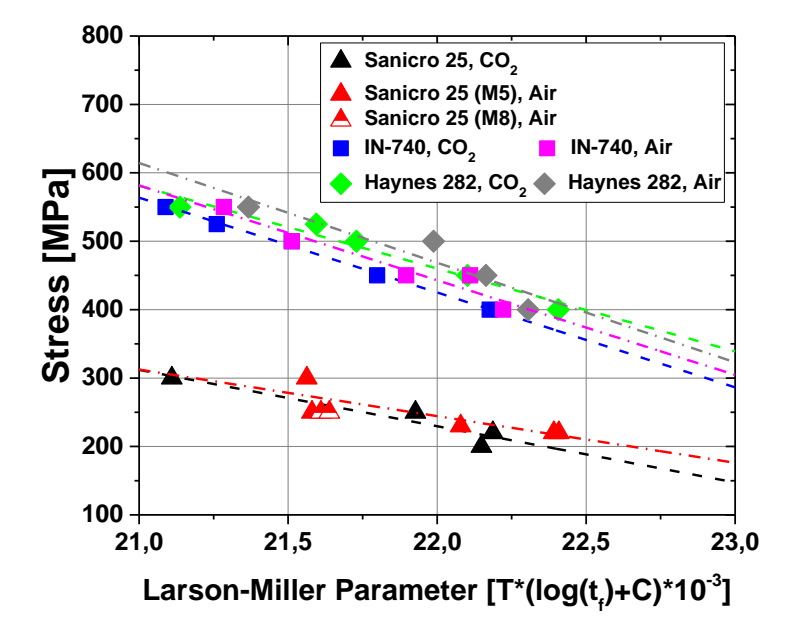


Figure 76. Larson-Miller plot of the investigated alloys in both test atmospheres. Please note that Sanicro 25 in air were tested with two sample geometries: M5 (miniature) and M8 (standard).

5.4.2 Study of the effect of the specimen size

Typically, creep experiments are performed on standardized samples according to DIN EN ISO 204 and/or ASTM E139. However, some situation where there is a small amount of material available, or in this case, a reduced geometry has been chosen to reduce the load required to achieve the same stress level, standard specimen cannot me mechanised and thus the use of miniature specimens is required

For comparative purposes, corresponding data for T92 (tube and pipe from NIMS) results are included in Figure 77. The times to rupture obtained for P92 (M5 specimens, similar to the small specimen used in this study) are shorter than the T92 (Tube and pipe). This can be attributed to an effect of the specimen size, according with the previous experience of CIEMAT with sub-size specimens in the study of the creep properties in ferritic-martensitic steels.

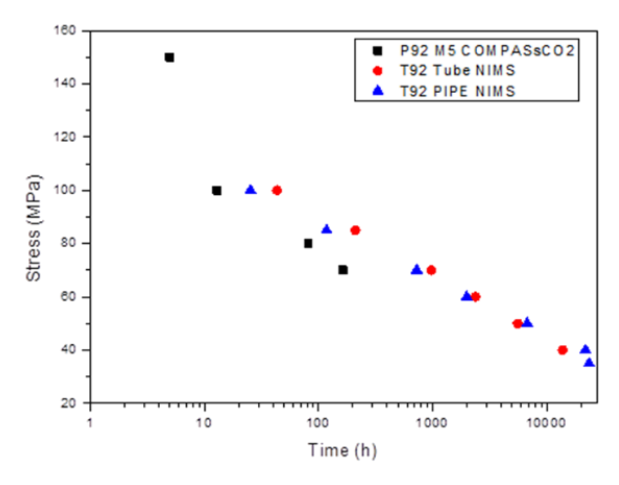


Figure 77. Stress (MPa) vs. Time (h) at 700 °C for P92 in air at 700 °C

In Figure 78 it can be seen that the smaller specimens obtain lower times to rupture in comparison with the standard samples under the same conditions. At high loads, the differences found between specimens M5, M8 and M12 could be considered within the expected scatter of the results, even though this same trend was found. On the other hand, as the load is decreased, this reduction in time-to-rupture is more evident. An effect of oxidation for long term creep tests cannot be excluded.

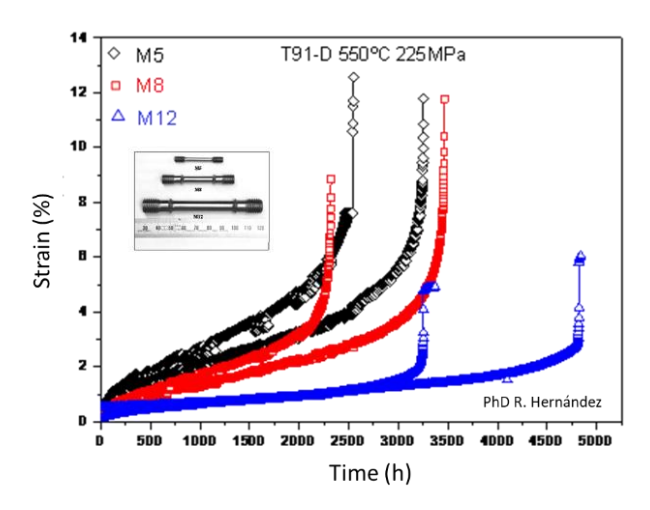


Figure 78. T91 steel tested on creep conditions (550°C, 225MPa) at CIEMAT.

The relationships established by Bertella-Oliver between the elongation and the uniaxial deformation can be found in the literature (11,12,13). These authors show that under uniform deformation regimen, the effect of the volume of material under stress do not affect the results, however as soon as non-uniform deformations (plastic) occurs, the final failure is accelerated for the smaller specimens giving a lower rupture time, leading to a wider scatter of the results.

Segle et al (14) carried out a very interesting analysis of the effect of specimen size on creep properties using finite element analysis of the stress distribution during a creep test. The differences observed in the minimum creep strain rate result in stress enhancements due to local stress redistribution and, depending on the creep ductility and creep rupture strength of the constituents, the time to failure would be more or less reduced when testing small specimens. Therefore, it is not evident a detrimental effect of sCO2 on the creep strain rate, and the lower values of the tests performed in air could be attributed to a size effect.

The following figure shows the results for Haynes 282 material. Despite the scatter due to the use of smaller specimens, the results obtained with smaller specimens (M5 geometry) are in agreement with the reference data and the sCO2 tests. It can therefore be concluded that there is no effect of specimen geometry or environment on for rupture time.

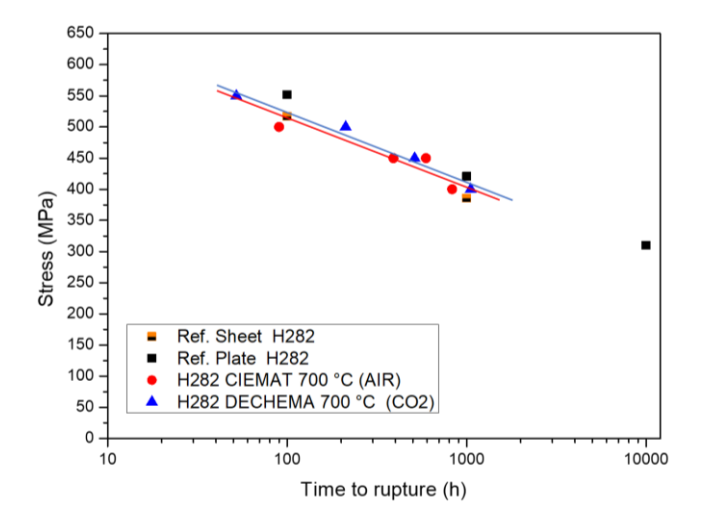


Figure 79. Stress (MPa) vs. Time (h) curve at 700°C for H282 alloys in air and CO₂

5.4.3 Use of the small specimen tests techniques: SSTT

SPC test technique was developed to study the creep properties of materials when the amount of material is small and a standard type specimen cannot be manufactured. The method can also be used as a screening method for novel materials manufactured in very small quantities

Figure 73 shows that SPC tests gives the lowest value fracture times for Sanicro 25 material, in accordance with the conventional uniaxial creep tests. Of the two Inconel alloys, higher times to rupture and lower minimum deflection rates are obtained for IN740, consistent with the results obtained in conventional uniaxial creep tests, as can be seen in the following figure:

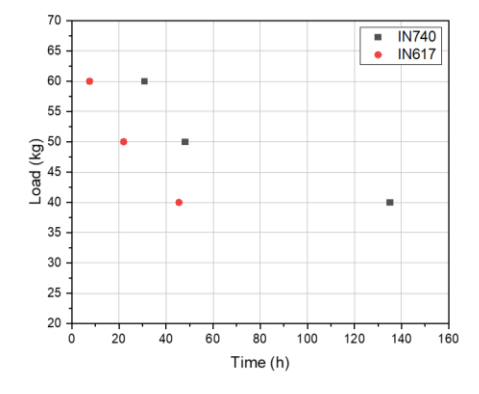


Figure 80. Load (kg) vs. creep time (h) for IN740 and IN617 alloys.

In the same way that the Norton equation relates the minimum creep velocity to the applied stress in a uniaxial creep test, for a small punch creep test, the minimum deflection rate can be related to the applied load by the following equation:

$$\dot{\delta} = A_{SPC} P^{n_{SPC}}$$

Following this equation, the exponent, n_{SPC} , could be used to estimate the Norton exponent using the small punch creep test. The justification is given by the relationship between the deformation and the deflection of the disc defined by Yang et al (15) based on the Chakrabarty model. In the next figure this relationship between displacement rate and load, P is plotted. The n_{SPC} values obtained in this study for Inconel 617 is 6.03 and for Inconel 740 is 3.90.

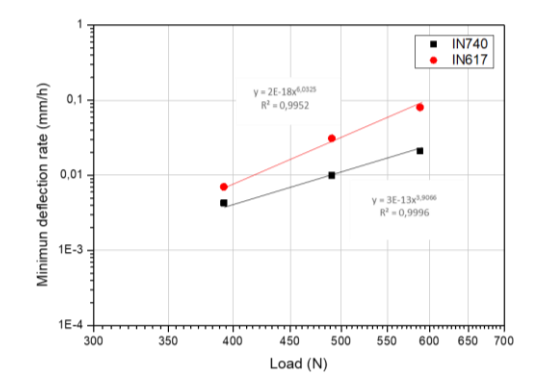


Figure 81. Deflection rate (mm/h) vs. load (N)

Kim et al (16) performed SPC tests on the IN 617 alloys and its weldments. They obtain a n_{SPC} value of 6.19 for the base metal, in accordance with the results at $700^{\circ}C$ and validated the reproducibility of this technique. The n_{SCP} value is higher for IN 617 than for Inconel 740 that means an enhancement of creep rate for IN 617, in accordance to the literature. The lower high temperature strength of IN 617 is due to the fact that it is a solid solution strengthened alloy whereas IN 740 is also strengthened by γ ' precipitates (17).

Figure 82 shows the specimens fractography in conventional uniaxial creep conditions. The failure mechanism was intergranular fracture. Intergranular creep fracture involves the nucleation, growth and subsequent bonding of voids at grain boundaries to form two different cavities: wedge cavities and isolated cavities, as can be seen in the figure and in literature (18). For IN740 alloy, SEM images reveal individual γ particles and areas of ductile fracture.

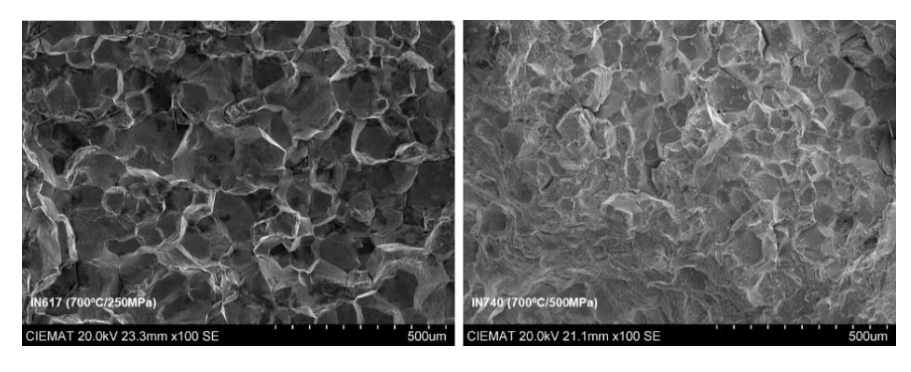


Figure 82. Fracture surface of conventional creep specimens for IN617 and IN740 alloys.

Figure 83 shows bottom fracture surface of the SPC specimens for IN617 and IN740 respectively. The creep brittle intergranular fracture mode was observed for both materials (16) and several circumferential brittle branch cracks. The fractography observed is consistent with that obtained in the conventional creep test and literature.

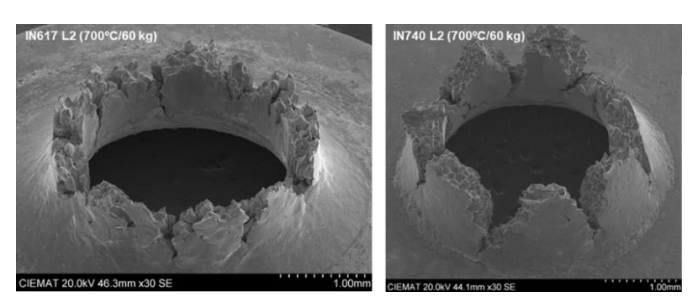


Figure 83. Bottom fracture of SPC rupture specimens for IN617 and IN740 alloys.

6 CONCLUSIONS

The following conclusions were reached:

WEAR/EROSION PROPERTIES:

- Wear/erosion tested has demonstrated the deposition of the particles over the metallic surfaces. The shape of the continuous deposits on more exposed faces shows the waveform typical morphology of wear/erosion degradation due to particles impact, which has not been observed in the free surfaces (backside) excluding the material removal in these zones.
- Results of weight measurements have shown a gain mass changes (Ciemat) due to the effect of the simultaneously exposition of all the tube faces for cylindrical specimens and loss mass changes (FZJ) for planar specimens by subtracting the contribution of the oxidation of previous tests. These results are complementary because the use of the tube cylindrical simulates the real exposition of the tubes and the effective erosion has been determined in the front face of planar specimens.
- The extent of particle deposition is mainly influenced by particle velocity and testing time but also on the material alloy. The highest depositions were obtained in the specimens tested with FerOx particles, at high velocity of 20mm/s velocity during 1000h, demonstrated by the presence of their chemical elements (Fe, O, Zr and Si).
- The erosion mechanisms seem be different between lower (700°C) and higher (900°C) temperatures due to the different oxidation kinetics. At lower temperatures the hardness of the base metal seems to play more important role in determining the wear resistance, whereas at higher temperatures the mechanical properties of the oxide scales can be of significance
- The oxidation-erosion testing shows that for majority of the alloys the least mass loss occurred when using IP 30/50, while the highest mass loss occurred with SB 30/50. The highest estimated hardness values of the SB30/50 granulate correlate well with the highest measured mass losses of the studied materials. However, the results with the other particles and materials indicate that other factors might play a role.
- Topographical backscattered SEM images of all samples post oxidation-erosion testing shown a black discoloration on the sample surface indicates granulate deposition (corundum). Hematite deposition from FerOx and Cr₂O₃ can be challenging to differentiate due to their similar average atomic weights. Zirconia was also detected on the surface, attributed to the m-ZrO₂ rich phase in FerOx 16/30.
- Regarding to the coating deposited over the metallic surfaces, a good resistance to erosion degradation has been demonstrated with only an isolated detached zone in the case of P92 with the lower time and particle velocity so it could be due to a non-detected previous defect. In addition, the particle deposits on the coatings are smaller and isolated, indicating better performance with the coating. The beneficial effect of the coating on Haynes 282 was demonstrated by the lowest weight gain, which is consistent with the lower particle deposition and no oxide formation observed in the specimen examination under all conditions.
- The hot long-term test results, performed at CVR, show that all tested samples exhibit erosion patterns on the sides of the microstructure, corresponding to areas with a particle velocity gradient, which leads to uneven wear.

Furthermore, the nickel-based alloys, along with some of the experimental chromium-based alloys, developed a compact and uniform oxidation layer. In contrast, most of the coated samples, as well as Sanicro 25, exhibited signs of spallation.

CREEP PROPERTIES:

- The Larson-Miller parameter describes the equivalence of time with temperature for alloys undergoing the thermally activated stress rupture creep process. Despite the variations in the minimum creep rate in different atmospheres, due to the scatter observed when using small specimens, the rupture duration data in air and in CO₂ show good agreement.
- For both atmospheres, a linear correlation between the applied stress and the rupture duration can be found and the slopes for the investigated alloys do not deviate strongly from each other in varying atmospheres. The main conclusions were:
 - Sanicro 25 exhibited the highest minimum creep rates among the alloys tested, followed by IN-617B.
 - γ'-strengthened alloys show increased creep life in both environments. H282 shows higher time to rupture and creep strains to fracture compared to IN-740.
- SP and SPC test techniques are suitable screening methods for the studying of the tensile and creep properties of materials in comparison with the conventional material using small amounts of material. This technique is sensitive to the study of the ductility of materials. For brittle materials, the estimation of SP parameters is complicated but allows to work on the design and development of the new materials before manufacturing large quantities.

7 FUTURE WORK

The focus of future work will be on a number of aspects:

- Most relevant result, in both laboratories, is that granulated particles are deposited or embedded in the metallic surfaces. Particle deposition must be evaluated taking into account the possible effect on the heat transfer coefficient of the tubes. Some aspects of the extent of particle deposition can be studied more deeply like particle flow rate, testing time, material and surface finished.
- Future studies could analyse the effect that the surface changes have on the mechanical and thermal properties of the materials, as these are critical parameters for the design of heat exchanger tubes. Particle deposition points out that further tests are necessary to determine the behavior of the actual composition of the particles to be used in the final heat exchanger design, with special attention on the resistance of the optical coatings deposited over particles and the influence of their composition.
- The creep properties of new development materials will be compared with state-of-theart materials characterised and tested on the same facility at CIEMAT using small specimen tests techniques in CO₂.

8 REFERENCES

- 1 Benameur N., Marlin S., Sutter F. Wiesinger F., Oskay C. Alkan, G., Menichetti E. (2022) Particle optimization by modifying chemical composition. Deliverable 2.2 COMPASSCO2.
- 2 Anthony J.W. Bideaux R.A., Bladh K.W., Nichols (2001): Handbook of Mineralogy, Mineralogical Society of America.
- 3 Collector's corner (2024) http://www.minsocam.org/msa/collectors_corner/article /mohs.htm. Mineralogical Society of America. Retrieved 12 April 2024.
- 4 Mohs' Hardness of Abrasives (2024). https://web.archive.org/web/20091017120910/http://www.reade.com/resources/reference-charts-particle-property-briefings/851-mohs-hardness-of-abrasives. Retrieved 12 April 2024.
- 5 Klein, C.; Hurlbut, C.S. (1993). Manual of mineralogy: (after James D. Dana) (21st ed). New York: Wiley. pp. 380–381.
- 6 Tamura, M., Abe, F., Shiba, K., Sakasegawa, H., & Tanigawa, H. (2013). Larson–Miller constant of heat-resistant steel. Metallurgical and materials transactions A, 44(6), 2645-2661.
- 7 Render, M., Santella, M. L., Chen, X., Tortorelli, P. F., & Cedro, V. (2021). Long-term creep-rupture behavior of alloy Inconel 740/740H. Metallurgical and Materials Transactions A, 52, 2601-2612.
- 8 Tortorelli, P. F., Wang, H., Unocic, K. A., Santella, M. L., Shingledecker, J. P., & Cedro III, V. (2014, March). Long-term creep-rupture behavior of Inconel® 740 and Haynes® 282. In Pressure Technology (Vol. 40740, pp. 29-36).
- 9 EN Standard EN-10371 (2021); Small Punch Test Method for Metallic Materials. European Committee for Standardization: Brussels, Belgium 2021.
- 10 Altstadt, E., Houska, M., Simonovski, I., Bruchhausen, M., Holmström, S., Lacalle, R. (2018). Journal of Mechanical Sciences, 136, 85-93
- 11 Davis, J. R. (2004) "Tensile testing" ASM International, 2nd edition
- 12 Annual Book of ASTM Standards (2003), ASTM "Standard Test Methods and Definitions for Mechanical Testing of Steel Products" Vol.1, 370, Annex 6.
- 13 John, M.; Holt, T. (1999) "Uniaxial tension testing" Alpha Consultants and Engineering, ASM International pp.124-142.
- 14 Segle, P., Tu, S. T., Storesund, J., & Samuelson, L. Å. (1996). Some issues in life assessment of longitudinal seam welds based on creep tests with cross-weld specimens. International journal of pressure vessels and piping, 66(1-3), 199-222.
- 15 Yang, Z., & Wang, Z. W. (2003). Relationship between strain and central deflection in small punch creep specimens. International Journal of Pressure Vessels and Piping, 80(6), 397-404.
- 16 Kim, B. J., Sim, Y. B., Lee, J. H., Kim, M. K., & Lim, B. S. (2011). Application of small punch creep test for Inconel 617 alloy weldment. Procedia Engineering, 10, 2579-2584.
- 17 Shingledecker, J. P., & Pharr, G. M. (2012). The role of eta phase formation on the creep strength and ductility of INCONEL alloy 740 at 1023 K (750 C). Metallurgical and Materials Transactions A, 43, 1902-1910.
- 18 Krishna R., Hainsworth, S.V., Atkinson, H.V., Strang, A (2010) Microstructural analysis of creep exposed IN617 alloy. Materials Science and Technology, 26(7), 797-802.